Nanowicking:

Multi-Scale Flow Interaction with Nanofabric Structures

Thesis by

Jijie Zhou

In Partial Fulfillment

of the Requirements

for the degree of Doctor of Philosophy

CALIFORNIA INSTITUTE OF TECHNOLOGY

Pasadena, California

2005

(Defended April, 2005)

Acknowledgements

I would like to thank Professor Morteza Gharib, my advisor, for providing an excellent learning environment, giving me the freedom and trust to pursue my interests, and keeping me on track. He is an inspirational leader and my academic role model. I sincerely appreciate his bringing together such a wonderful group of intelligent people who have contributed to my graduate career in various ways. And I am grateful for his guidance in preparing me for a career in science. Furthermore, I thank him for encouraging me to explore other projects and expanding my scientific imagination.

I would also like to thank Dr. Flavio Noca, my co-advisor, for impacting my scientific and personal development. As I struggled through my first few years of graduate school, his aid and encouragement made this work possible.

I want to thank my Ph.D. committee of professors: Guruswami Ravichandran, Scott Fraser and Joel Burdick. Professor Ravichandran advised me on a previous project about actuation with moisture in a natural porous material. The important questions he asked in that project enlightened me in a variety of ways on this project. He always encouraged and supported my scientific pursuits. Professor Fraser was the committee chair of my candidacy exam when I proposed this project. He asked me to focus on one problem and his insight greatly speeded up my progress. Professor Burdick made special travel plans in order to attend my defense exam.

I have been incredibly fortunate to be surrounded by amazing people throughout my time at Caltech. Special thanks to Professor Mel Simon for his unending enthusiasm and support of my work. He and his group generously provided lab supplies, equipment and valuable suggestions in their field of expertise. I also sincerely thank Dr. Brian Hunt from the Jet Propulsion Laboratory (JPL) for supporting this work and my career. He and his group synthesized carbon nanotube arrays and provided advice for this work. I wish to thank the following people for their encouragement, training and help on my laboratory work including imaging and lithography: Chi Ma in the Geological & Planetary Sciences Division; Randall E. Mielke and Michael J. Bronikowski at the Jet Propulsion Laboratory; Tau-Mu Yi and Valeria Mancino in Biological Sciences; Alireza Ghaffari and Will Green in Applied Physics; Zhongping Huang at NanoLab Inc.; and Qiang Liu at City of Hope Hospital. I also want to thank all the members of Mory's group who have come and gone, particularly Anna I. Hickerson, Ben Lin and Elijah Sansom, who frequently lent their support.

I would like to thank my husband, Kun Wei, for his encouragement and patience as I pursued my doctorate, and my parents who taught me from an early age the importance of hard work, discipline, and the pursuit of knowledge.

This thesis is dedicated to the apple of my eye, my daughter, Lingyi Wei.

This work was supported by the NASA Office of Biological and Physical Research (Award No. 04520-06); and the NSF NER Program (Award CTS-030473).

Abstract

Dense arrays of aligned carbon nanotubes are designed into strips — nanowicks — as a miniature wicking element for liquid delivery and potential microfluidic chemical analysis devices. The delivery function of nanowicks enables novel fluid transport devices to run without any power input, moving parts or external pump. The intrinsically nanofibrous structure of nanowicks provides a sieving matrix for molecular separations, and a high surface-to-volume ratio porous bed to carry catalysts or reactive agents.

This work also experimentally studies the spontaneous fluid transport along nanowicks. Liquid is conveyed through corner flow, surface flow, and interstitial flow through capillary force and the Marangoni effect. The main course for corner flow and surface flow follows Washburn behavior, and can deliver liquid centimeters away from the input blob with a speed on the order of millimeters per second depending on the nanowick configuration and the amount of input liquid. Corner flow can be minimized and even eliminated through proper nanowick and input design. Otherwise, corner flow interacts with surface flow in the first 2mm of the pathway closest to the input point. Interstitial flow dominates the late stage. It is driven by both capillary force and concentration-gradient-induced Marangoni force. The concentration gradient is determined by two competing rates: surfactant diffusion in solution and adsorption onto nanotube surfaces. The flow inside nanowicks may wick hundreds of microns in seconds or tens of seconds. A non-conventional advancing

front may develop in the flow around nanowicks. They are seen as (i) Rayleigh instability-induced fingering in surface flow on millimeter-wide nanowicks, (ii) viscous instability-induced branching near almost-stagnant surface film at low surfactant concentration, and (iii) disjointed wetting domains at very low concentration.

Additional keywords: microfluidic, microdevices, nanowicking, spontaneous transport, carbon nanotubes, nanoarrays, nanoporous, nanopillars, nanocarpets, nanoforests, capillarity.

Table of Contents

List of Figures

Chapter 1

INTRODUCTION

1.1 Motivation

Progress in miniaturization technology, such as a solid-state transistors, has been shaping the world. The microfluidic devices for chemical/biological sample diagnostics are going to define a new paradigm for chemical analytical devices. Such microfluidic analytical systems have a quick turnover time and great portability, and are suitable for domestic, military, and even space applications. They are going to greatly improve the global quality of medical care based on the tremendous growth of new knowledge on the molecular basis of life processes.

Most microfluidic devices currently rely on large auxiliary setups and external power input to drive liquid through microchannels[14, 16, 43, 53]. This work proposes and studies a miniature wicking element—the nanowick—for spontaneous delivery of small amounts of liquid with wetting and spreading forces. Delivering liquid by wetting and spreading forces avoids unreasonably large pressures required to push liquids through small channels and small interstices because the required pressure gradient increases inverse-proportionally to the fourth power of the characteristic size.

In addition, this delivery element can be integrated with other microfluidic analytical functions. The fibrous structure of nanowicks provides a large surface-to-volume ratio. Consequently, nanowicks can be designed to carry catalysts and

reactive agents, or utilized as sieving matrixes for molecular separations (as in chromatography), which also make nanowicks a good candidate for portable or disposable fluid sampling and analysis devices.

1.2 Nanowick definition

Since Feynman considered the possibility that we "can make a thing very small which does what we want" in 1959 [(22)], there are two typical approaches to build a nanoscale analytic device or system—top-down and bottom-up. Top-down techniques create micro/nanoscale mechanical structures out of bulky materials. But device dimensions by conventional techniques are limited by the resolution of electron-beam lithography, etch roughness, the synthesis of epitaxially grown substrates, and other factors. Bottom-up techniques chemically synthesize nanostructured materials such as carbon nanotubes. The achieved structure can be smaller and smoother than one created with conventional e-beam lithography. Large-scale integration of nanoscale functional structures with top-down fabrication techniques becomes a crucial challenge. On the other hand, bottom-up techniques only create materials, not devices. We combine these two approaches to make cheap, high throughput devices that rely on nanometer-scale dimensions to attain their functions.

We have fabricated surface patterns of dense arrays of aligned carbon nanotubes. They can guide liquid flow by capillary action and themselves can be treated by the chemicals in the solution in the mean time. We call a strip full of dense arrays of nanotubes for liquid delivery a *nanowick*.

A wick is a thread, strip, or bundle of fibers to draw up, by capillary action, the oil of a lamp or the melted wax in a candle to be burned. Wicks were invented 3000 years ago and are typically composed of microscopic fibers of material such as flax, cotton, mullein, asbestos, linen, oakum, or papyrus. About 50 years ago, the word "wick" began to be used as a verb meaning to convey by capillary action. Wicking depends on wetting properties. Wetting is the displacement of a solid-air interface with a solid-liquid interface. Textile, painting and printing industries have been studying capillary flow on micro-scale porous fibers or layers. However, liquid flow through nanoscale porous media or fibers has been less studied.

The nanowick configuration and dimensions are different from conventional fabrics or porous media. The nanowicks in this work are 30 to 1700 microns wide, 3 to 80 microns high, and up to 2 centimeters long. They are grown on flat wafers, consisting of nanotubes vertical to the wafer. The diameter of the nanotubes is about 20 nanometers and the center-to-center space is about 60 nanometers. Considering the nanowick as a strip of porous media, its pores are anisometric, and the transverse pore size is 3 orders of magnitude smaller than conventional porous media. Because of the overall large <free boundary surface>-to-<porous body volume> ratio, liquid transport formats, other than interstitial flow, become distinct on nanowicks. Most of the wicking experiments in this work are carried out with surfactant aqueous solution. The addition of surfactants is widely used to control evaporation and to accelerate the capillary penetration of aqueous solution in hydrophobic porous bodies. Furthermore, surfactants are present in most biological buffer solutions.

In addition, the opaque nanotubes on a clear wafer enable us to distinguish inside flow from surface flow. In contrast, traditional translucent porous material

confuses the liquid location. This work provides direct observation on the progressive front and a variety of stages in liquid transport on nanowicks.

1.3 Background

1.3.1 Carbon nanotubes

Carbon nanotubes (CNT) were discovered in 1991 by S. Iijima.[28] They can be viewed as a large macromolecule of carbon, analogous to a sheet of graphite rolled into a cylinder. They are light, flexible, thermally stable, and chemically inert with a very broad range of electronic, thermal, and structural properties that change depending on the different kinds of nanotubes (defined by its diameter, length, and chirality, or twist). Single-wall carbon nanotubes (SWNTs) have an average diameter of ~1.3nm, the carbon bond length of 1.42Å; multiwall carbon nanotube (MWNT) diameter varies from 7nm to 200nm. Carbon nanotube thermal conductivity is on the order of 2000 Watt/meter/Kelvin; electrical resistance $10^{-4}\Omega$ cm; Young's Modulus 10^{12} Pascal (1TPa); Maximum Tensile Strength 10^{11} Pascal (100GPa). [4, 57, 67, 68]

In this writing, nanotube by default means carbon nanotube.

Carbon nanotubes, as their graphite relative, are hydrophobic. The contact angle of a single tube has been theorized to increase with the decreasing radius of the tube[38]. Based on existing values for contact angles of water on graphite, theoretical considerations have suggested that the equilibrium contact angle for nanotubes 20 nm in diameter (the typical value of most nanotube carpet samples used in this research) should be about 83°. Experimental results have proven the predict value of 80.1±3.6˚ for approximately 20nm multiwall carbon nanotubes.[3] However, once the nanotubes

assemble into a carpet of aligned nanotube arrays, the carpet, as a whole, functions as a super-hydrophobic (contact angle higher than 150°) surface. The contact angle of a water droplet on top of the carpet is 158° ±1.5°, when nanotubes have "uniform external diameter of about 60nm[*]."[21]

1.3.2 Capillarity and wetting phenomena

Wetting refers to how a liquid spreads out on a solid substrate or another liquid. Capillarity studies the interfaces between two immiscible liquids or between a liquid and gas. The studies of wetting and capillarity play a major role in many scientific endeavors and industrial areas, such as oil recovery, textile production, surface physics (anti-stain, anti-frost, improving adhesion treatment), chemical industry (paints, ink, coloring ingredients, insecticides) and some fields in life sciences (inflation of lungs, sap transportation in trees, adhesion of parasites on a surface).[17]

Intermolecular forces are responsible for surface tension. Molecules in liquid attract each other and lower their potential energy. Surface tension therefore tries to minimize the surface area. Given a molecule with potential energy 0 when isolated faraway, and potential energy $-U$ when surrounded by other molecules inside the liquid, the potential energy for it to sit on the surface is roughly $-U/2$. The molecule finds more attraction toward the inside of the liquid where the potential energy is lower. The surface tension is a direct measure of this potential energy difference from the surface to inside per unit surface area. If the molecule size is a and its exposed

---

[*] However, the tube diameter looks to be ~20nm and tube spacing is ~30 or 40nm in the published SEM images. Therefore, 60nm could be the center-to-center spacing.

area is of order a^2, the surface tension is on the order of $U/(2a^2)$. Surface tension is often denoted as γ in a capillary system, or σ in free surface studies.

Although the surface tension originates from intermolecular forces, it is a macroscopic parameter and can be defined mechanically from the energy or force angle of view.

Surface tension can be viewed as a force per unit length, directed toward the liquid along the local radius of curvature on any interested curve. It provides remarkable forces that enable liquid to rise or drop in a narrow tube, insects to walk on water, and liquid surface to be sub-atomically smooth. On the other hand, surface tension can be viewed as energy per unit area, which is required to generate more surface or surface area. These two aspects — energy and force — are typical approaches to studying surface (interfacial) tension.

The field was pioneered by Pierre Simon de Laplace and Thomas Young in the early 19th century. The general Young-Laplace equation describes the hydrostatic pressure difference (ΔP) traversing the boundary between two fluids:

$$\Delta P = \gamma \cdot \left(\frac{1}{R_1} + \frac{1}{R_2} \right), \qquad (1.3.2A)$$

where R_1 and R_2 are the principle radii of curvature at the interface. The Laplace pressure can explain why small bubbles empty themselves into connected large ones, and how wet hairs adhere together through capillary bridges. Applying Laplace pressure to capillary rise in a small circular tube of radius R, the biggest radius of curvature of the interface is obtained at the bottom point, and the two principle radii of curvature are the same—$R/\cos(\theta)$ (see Fig 1.1). Consequently the capillary pressure

is

$$\Delta P = \frac{2\gamma\cos(\theta)}{R}, \qquad (1.3.2B)$$

where θ is the contact angle. The contact angle characterizes the angle formed at the edge of a liquid where it contacts a solid surface (see Fig 1.2). It is defined in Young's relation (1805):

$$\gamma_{LG}\cos\theta = \gamma_{SG} - \gamma_{SL} \qquad (1.3.2C)$$

Young's relation can be viewed as force balance of the interfacial tensions on the triple line between three phases (Solid/Liquid/Gas), or as zero work done by surface free energy at equilibrium.

The classical physical concepts for the spreading of liquids on a solid surface are influenced by a disparity in the surface or interfacial tensions at the three-phase contact line. If the solid/gas surface tension (γ_{SG}) is greater than the sum of the liquid/gas and solid/liquid interfacial tensions ($\gamma_{SL} + \gamma_{LG}$), the liquid will spread on the solid surface until the surface tension balance is restored. According to this concept, spreading is driven by wetting (i.e., solely by the unbalanced capillary force on the three-phase contact line) and the three-phase contact angle decreases with time as the liquid spreads. From the definition in Eq. 1.3.2C, it is expected that spreading, wetting and a low contact angle are associated with high solid surface energy and low liquid surface energy.

The contact angle phenomena are, in practice, very complicated. It is generally found that a large range of contact angles is accessible experimentally, causing wetting or contact angle hysteresis. To avoid hysteresis or pinning effects caused by surface roughness, chemical heterogeneity, or adsorption layers, it is strategic to

choose ideal surfaces that are homogeneous and smooth on an atomic scale such as highly-oriented pyrolytic graphite (HOPG), microelectronics silicon wafers, and elastomers cross-linked from liquid film. A substrate is considered hydrophobic when the contact angle that water forms on it is greater than 90°. Otherwise, the substrate is considered hydrophilic.

1.3.3 Capillary number and capillary length

Dimensionally, surface tension is force per length: [γ]=[force]/[length], and viscosity is the product of pressure and time: [η]=[pressure][time]=[force][time]/[length]^2; as a result, [γ] / [η] =[length] / [time] = [velocity]. The number

$$V^* = \gamma / \eta \qquad (1.3.3A)$$

is defined as a *characteristic velocity*. It tells how much the driving capillary force overcomes the retarding viscous force in a liquid. It ranges from 1μm/s (viscous polymer) to 70 m/s (water). Characteristic velocity is a liquid property alone and does not interfere with the structure that liquid flows in or on. But surface tension cannot function without the interface. The following dimensionless number counts in the effects from interfaces. If the velocity in a real flow is V, then V/V^* is defined as *capillary number* Ca:

$$\text{Ca}=V/V^*=V\,\eta / \gamma \qquad (1.3.3B)$$

The dimensionless capillary number controls the dynamics of wetting and time-dependent phenomena. It reflects some geometrical features in the system such as porosity as well as the properties of spreading liquid.

Climbing spontaneously against gravity is a phenomenal property that capillary force gives liquids. There exists a particular length (λ) to distinguish the relative

importance between surface tension and gravity, which is termed *capillary length*:

$$\lambda = \sqrt{\frac{\gamma}{\rho \cdot g}} \tag{1.3.3C}$$

The distance (λ) is on the order of a few millimeters. Inside the range of capillary length, capillary effects dominate and gravity is negligible; outside gravity dominates.

Chapter 2

NANOWICK DESIGN AND FABRICATION

We combine the bottom-up technique, self-assembly of carbon nanotube arrays, with top-down photolithography to fabricate large-scale fluid analytical devices with nanoscale functional structures. The overall dimension of such a device is on the order of centimeters; the delivery element is often designed to be 100μm wide; the building block—nanotubes—is approximately 20nm thick. This hierarchical structure is demonstrated in Fig 2.3. The actual appearance of the wafer is given in Fig 2.4. Figure 2.1 summarizes the lithography and self-assembly steps.

2.1 Growth of carbon nanotube arrays

Growth of nanotubes is a bottom-up self-assembly process, typically done at high temperature (>600°C) with a steady supply of carbon-containing gas (e.g. methane, ethylene, acetylene) over a substrate that is adequately layered with a thin coat of catalyst. The nanotubes can be produced in large, well-ordered arrays with individual nanotubes being vertically oriented with respect to the substrate. The concept is similar to a field of grass or wheat, but on a vastly smaller length scale. These well-aligned carbon nanotube arrays on inch-size wafers are named *highly ordered carbon nanotube arrays*, or "nanocarpets." Regularity of the arrays and straightness of nanotubes are controlled by steady conditions for growth, such as gas

flow rate, temperature, catalyst thickness, etc. When the nanotubes become too long to stay straight, the layer of nanotubes may look tangled from top view. We can *not* refer to such a layer of nanotubes as a highly ordered array of carbon nanotubes, yet the nanotubes are indeed much more regular than typical porous materials such as agarose gels. We refer to this carbon nanotube layer as a *carbon nanotube mat.* It is also termed nanocarpet or "nanoforest" in the literature, because of its appearance under SEM imaging (see Fig 2.2). The size of the growth wafer is limited by the size of the heating core in the furnace and diffusion control capability.

Configurations of the nanotube mats (spacing, diameter, and height) are adjustable by catalyst deposition and growth conditions (e.g. temperature, flow rate of carbon-containing gas, and growth time). The wafer needs to survive high temperature and be non-reactive with the catalyst at high temperature. For example, silicon bonds with iron at a high temperature and kills the catalyst; a 100nm oxide layer on silicon wafer is able to isolate the catalyst to preserve its function. We tried sapphire (Al_2O_3), quartz (SiO_2) and a thermal oxidized silicon wafer.

All nanowicks used in this work were grown in the JPL Microdevices Laboratory by Michael J. Bronikowski with a modified recipe emulated from Hongjie Dai group's 1999 work at Stanford University [20]. In the first step, a 6–8nm thin layer of iron is sputtered/coated onto a wafer as a catalyst for the growth. Second, the wafer is heated in a furnace to mobilize the top of the thin metal layer into particles, through sintering, from which the nanotubes can grow. Then, carbon-containing gas is fed into the furnace at high temperatures (e.g. 650°C) to allow self-assembly of carbon near the catalyst particles into cylindrical tube structures that are vertical to the substrate. The cylindrical tube is pinned on the support wafer, in this growth model, by the

catalyst. (In another model, the catalyst may sit on top of the nanotube like a cap.) The self-assembly process usually takes a few minutes. The growth rate, in the first phase, is linear for the first few seconds when the tube length is within a few microns. For the second phase, the rate seems to halt and then burst to tens of microns (20–40μm), probably because a new mechanism for growth needs to establish itself. In the third phase, the growth rate starts to be limited by the rate of diffusion. Grown normally, straight nanotubes are a state-of-the-art technology. There are other, arguably higher quality, nanotube growth methods such as electric arc discharge, hydrocarbon pyrolysis, laser vaporization, etc. The growth recipe is often empirical and equipment-sensitive. Contamination control is very important. A few other configurations of nanotube mats were purchased from NanoLab[26, 27, 44, 58] for comparison. There are many other state-of-the-art aligned nanoarray structures[19, 24, 29, 39, 69] in different configurations, or made with other materials that are not included in the work.

Nanotube/nanowick samples are stored in dry cabinets and desiccators. No shelf-life issue has been encountered so far.

2.2 Patterning carbon nanotube mats

This work patterns carbon arrays by patterning the catalyst, because nanotubes only grow from where a catalyst exists. Therefore, up-scaled functional devices with nanoscale structures can be obtained without post-growth manipulation or assembly. And, if desired, the patterned nanotube mats are ready for encapsulation and chemical treatment. The width of nanowicks is most often designed to be 100 microns for easy optical observation. For most features greater than 6μm, patterning the catalyst can be

done with inexpensive high-throughput photolithography. Smaller features may require e-beam lithography.

Growing carbon nanotubes from a micro-patterned catalyst enables low-cost, high-output device manufacture without painstaking post-growth manipulation of nanotubes. The catalyst layer can be patterned with photolithography, through utilizing the native inclusions in the wafer crystal, or even by scratching metal onto the wafer by hand.

2.2.1 Patterning with photolithography

Arbitrary design of the catalyst deposition layer by photolithography allows any desired surface pattern of nanotube mats to be grown, and their location on the wafer to be precisely controlled. Figures 2.5–2.8 show photo-lithographed nanowicks and their details. Photolithography is a very mature technology and has long supported the success of the semiconductor industry. The following steps are taken to pattern the catalyst with photolithography after designing the pattern on a computer and printing it on a film or glass to make a mask.

1) spin a thin layer of photoresist on the wafer of choice.

2) align the mask on top of the wafer and expose to UV light.

3) rinse the wafer in developer so that the exposed positive resist or unexposed negative resist is washed off.

4) sputter the catalyst over the whole wafer. (The catalyst directly contacts the wafer only on the area where resist has been developed away.)

5) liftoff (usually with acetone) all the remaining resist. Only the catalyst having direct contact with the wafer survives; others are washed away with the resist.

2.2.2 Patterning without lithography

Depending on the application, the patterns of carbon nanotube mats themselves may be preferred rather than their particular location on the wafer. Patterns can even be generated without lithography. For instance, the large-scale parallel nanowicks can be made by scratching a fresh-split catalyst metal onto the substrate wafer. The natural roughness on the metal surface deposits some micron-wide parallel lines of catalyst for nanotube growth. The two-scale rough surface in Fig 2.9 can be fabricated through growing nanotubes on sapphire wafers with iron and titanium inclusions that affect the nanotube growth rate. (Iron and titanium, present in the form of ilmenite, a mineral which is a titanium iron oxide-TiFeO3, are known to form microscopic slender fibers in the aluminum oxide lattice, which may be responsible for sapphire's optical effects: "asterism.") Deep micro-canyons as in Fig 2.10 can be induced by thermal fractures on the catalyst layer.

2.3 Enclosing nanotubes in a channel

Encapsulating nanowicks into channels can eliminate free-surface flow and provide control over experimental environment parameters such as evaporation. Perfect alignment of nanotubes inside channels requires growing nanotubes inside the channels directly. Because of the complexity of gas diffusion around channel sidewalls and the time limit of collaborators, a simple coarse approach is chosen — to align nanowicks into a channel as a control experiment. A gap of a few microns between the side walls of the nanowick and the channel wall cannot be avoided in this approach.

The cover channel is a size and pattern matched silicone elastomer channel. The elastomer is also known as silicone rubber, typically formed by cross-linking PDMS – poly(dimethyl-siloxane) – around platinum. It is a widely used material for soft-lithography devices, and has Young's modulus ~750kPa. In a typical soft-lithography device, two layers of PDMS channels can be made with a thin membrane (~30 μm) in between[43]. The top channel can expand and deform the thin membrane, when activated pneumatically, to close the bottom fluid channel. The top layer can control the bottom flow by its valve and pumping function and isolate parts of channels from others and their environment. Both layers of channels are made by pouring PDMS onto a mold, and then peeling the PDMS off after curing. The mold is typically made by photolithography. The peeled-off PDMS channels are open on one side, and are ready to seal when placed onto a flat surface. Compatible nanowicks are grown on the supporting substrate, such that they can be aligned and placed in the bottom channel. Figure 2.11 illustrates this process.

A through-hole can be punched before sealing for liquid input.

Chapter 3

FLOW INTERACTION WITH NANOWICKS

3.1 Introduction

Preliminary experiments have demonstrated that nanowicks are not only configurationally but also dimensionally different from conventional fabrics and porous media. An old myth about wicking is that wicking requires capillary structures to occur. Wicking was originally defined as the spontaneous flow of liquid in a porous substrate, driven by capillary forces[31]. However, recent experiments and numerical simulations prove that the spontaneous flow by capillary action may happen in open channels[18, 34, 46-48], or even just on strips that are chemically different from other areas but geometrically flat without any kind of channel confinement[15, 63]. (For less confusion, some investigators refer to open channel capillary flow as *spreading*.)

As the overall structure shrinks, free surface flows outside the porous body become distinct. This work first identifies flow by their locations relative to nanowicks. Flows have been observed in three feature topographies:

(i) in the corner between an edge of nanowick and the supporting wafer— *corner flow*;

(ii) over the top roughness of nanotube arrays— *top surface flow*;

(iii) through the interstices of dense nanotube mats— *interstitial flow*.

The three flow formats are sketched in Fig 3.1.

A corner is the same as a V-shaped groove surface with an opening angle of 90 degrees, especially for films thinner than the capillary length. And corner flow is observed to be induced by the corner's shape alone, the same as V-groove flow[34, 46, 47]. Corner flow can be minimized, even eliminated by the proper design of inlet or nanowick configuration. Surface flow on the asperities is topography-driven (roughness-assisted) spreading[6, 36, 65], as well as the corner flow. The spiky top surface, consisting of nanotube tips, provides nanoscale roughness. Surface roughness can exaggerate a material's natural wettability. That is, roughness improves wetting and spreading on hydrophilic surfaces, and magnifies hydrophobicity for hydrophobic ones[40, 65]. Interstitial flow, from this work's observation, is slower, but more persistent than the other two, because nanopores produce both the largest viscous drag and the largest wetting force in flow. The former presents as "slower", and the latter presents as "persistency."

In reality, liquid first spreads on a composite air-solid surface. Consequently, surface flow creates air pockets inside the nanowicks, and trapped air generates a resistance to liquid penetration along a nanotube's long axis. As the front of surface flow moves farther away from the supply droplet, the surface flow slows down because the capillary force has to work over a larger distance. Lateral interstitial flow then takes over and leads the surface flow. The lateral interstitial flow along the nanowick's long axis takes place in several formats, sensitive to boundary conditions and surfactant concentration. Generally, the overall progression of liquid flow around and inside a nanowick is sensitive to the inlet condition, liquid properties, nanowick

configuration and operating ambients. Figure 3.3 gives a schematic diagram of flow stages, neglecting the corner flow.

3.2 Experimental methods

3.2.1 Light microscopy for dynamics and scanning electron microscopy for nanoscale resolution

One difficulty in imaging is obtaining a large field of view and high resolution at the same time. An additional challenge is imaging the three-dimensional liquid that is constantly *deforming*. The theoretical resolution of ordinary light microscopy is about 200nm. We sacrifice the resolution for a greater field of view in order to observe the moving liquid front for a longer period. High contrast features or displacement of a couple of microns are easily visible.

Light microscopes, such as upright, long-working-distance microscopes, and inverted fluorescent microscopes, are used for time-dependent observations. Surface flow and corner flow changes the reflected and scattered light on nanowicks and wafers. Consequently, a wet region appears different from a dry region. Figures 3.8 and 3.9 exemplify the view under microscopes. *Liquid is supplied from the left and flows toward the right in all graphs depicted in this writing*. The next two sections explain methods for observing interstitial flow.Video signals from the microscope CCD (29.97 frames per second) are recorded by a computer (high resolution) and camcorder (long-term low-resolution storage). Visible displacement from frame to frame is then measured in software such as Adobe Photoshop.

Scanning electron microscopy (SEM) is employed for high-resolution dry morphology studies of nanotubes and nanowicks before and after liquid tests. Most SEM micrographs in this work are taken with the LEO 1550VP Field Emission Scanning Electron Microscope. Three other SEMs have also been used.

Scanning electron microscopy, in principle, is no different from light microscopy. It simply replaces visible light with a smaller wavelength counterpart — an electron beam. It analyzes the electrons and radiant rays that are emitted from the sample surface while being bombarded with the electron beam. SEM has a theoretical resolution of about 0.6 Angstrom. It shows a detailed three-dimensional view of a sample surface at much higher magnifications than is possible with a light microscope. While most SEMs only provide a qualitative view of relative sample heights with good depth-of-field, the latest LEO 1550, using a precise laser control over the stage, provides better than 1μm resolution in height measurement without tilting the sample.

3.2.2 Fluorescence microscopy for interstitial flow

All the interstitial flow is visualized from the bottom through a clear (quartz) wafer in an inverted fluorescent microscope with the addition of dye molecules in the solution. Because visible light cannot penetrate the dense arrays of carbon nanotubes, the fluorescence signal is stimulated and received from the clear wafer side (the bottom of the carbon nanotube array). Consequently, the signal is inside the nanotube arrays/nanowicks and not superficial. The corner flow is visible from the bottom view but none of the surface flow.

Fluorescein is added in aqueous SDS solution to visualize the flow but it is a mild surfactant itself and influences the cmc of SDS. (Appendix B provides some background about surfactants and SDS.) Additionally, SDS can increase the efficiency of chemiluminescence. Actual cmc of SDS upon addition of the amount of fluorescein in these experiments is not found in the literature. Nile red is dissolved in methanol and then added into PDMS mixture. The methanol is evaporated before wicking tests. The PDMS liquid used in this work has a viscosity of 50 centistokes, and average molecular weight of approximately 5000. The diffusion rate in very thin capillary structures could limit the dye molecule concentration in meniscus. Consequently the light intensity changes from dye additives can be coded as dye concentration, provided the thickness of background liquid in the view window is uniform, which can be proven with surface tension actions.

Another way to analyze the thin wedges of progressive fronts embedded in carbon nanotubes is to detect the action of surface tension. Configuration changes of the nanotube arrays by the surface tension can be detected optically. Please refer to the following section for details.

3.2.3 Detection of the interstitial progressive front

Visualization of the interstitial front is difficult, especially at the progressive front where the adsorption of fluorescein molecules onto carbon nanotubes overcomes the diffusion supplement. That is, there may not be enough fluorescein to detect all parts of the progressive front effectively (further discussed in Section 5.1 and 5.2). In this case, the action of surface tension can help visualize the front or part of the front. The surface tension effect can be confirmed in SEM in great detail after the

experiments. Detection of the front with surface tension under optical microscopes has a resolution better than a few microns. There are three types of actions by surface tension that are fundamentally the same:

(i) Shrinking of the nanowick sidewalls as the interstitial flow advances. This can be observed dynamically;

(ii) Forming of trenches/cracks on the edge of liquid as it dries. This happens after liquid stops moving;

(iii) Opening of circular, polygonal, or slender cells everywhere in the wetted nanotube arrays during dewetting.

The open cells are termed *nests*. Their formation is controlled by the dewetting process of liquid on the surface and bubble growth inside the nanotube arrays. The self-assembly nest formation mechanism is being studied by fellow graduate student Elijah Sansom. Nest formation and patterns are not discussed in this work, but nests can be used as markers showing the regions where liquid has reached.

Surface forces can act in the absence of evaporation, for example with non-volatile liquid PDMS. Light is seen to penetrate the nanotube layer as soon as surface flow reaches there. This might occur because (i) thin film PDMS liquid can deform the nanotube arrays while sinking into the nanotube bed from the top surface; (ii) the tethered chains of flexible nanotubes are organized by liquid/solid interaction inside liquid; (iii) capillary force dislocates a nanotube by unbalanced interface curvature on two sides[66] such that near nanotubes become closer and far nanotubes become farther apart. The action of surface forces depends on the configuration of nanotube arrays, liquid properties and even the wetting history.

Surface forces on minute structures are so distinct that any liquid will always leave a trace in the delicate nanostructures. The trace can be utilized to decipher flow without direct observation of the liquid. This is further exemplified in Section 5.3.

3.3 Inlet condition

As a prototype, we adopt an easy input interface by placing a small drop of solution (0.5~2.5μL) beside exposed nanowicks, on an inlet auxiliary pad, or into two-millimeter-wide through-holes for encapsulated nanowicks.

In order to convey water-based solutions through well-known hydrophobic carbon nanotubes, we take advantage of surfactants in bio-molecular buffers and use anionic surfactant SDS (well below cmc) or non-ionic surfactant Triton X-100 biological compatible (0.01– 0.1wt%) aqueous solutions. (Appendix B lists some fundamentals of surfactants.) The addition of surfactants not only accelerates the penetration of aqueous solution in hydrophobic porous structures, but also decreases the rate of evaporation on the free surfaces.

3.3.1 Supply droplet

A droplet of volume 0.5-2.5μL is deposited beside or on top of the nanowick to supply flow. The volume is measured with a Hamilton syringe, which is held in place with a micromanipulator. The droplet is suspended from the Teflon tip of the syringe before it is moved down and contacts the nanowick. The droplet is assumed stationary with no injecting speed. The droplet spreads upon the wafer and tries to reach the equilibrium advancing contact angle. The spreading depends on liquid properties and surfactant concentration (if applicable). While spreading, liquid leads the droplet

through the nanowick while the outward flux decreases the droplet volume and decreases the contact angle. When the contact angle at the triple line of sessile is reduced to the receding contact angle, liquid in the droplet starts to retreat as shown in Fig 3.4.

The retreat of the triple line may be continuous throughout the drying process, or the rapid depletion of low-surface-tension liquid close to the nanowick, aided by film instability, may create a dry curve inside the droplet and end up draining only the liquid close to the nanowick as shown in Fig 3.5A. The depletion of only the part of the liquid close to the nanowick has also been observed with PDMS, which is a non-volatile liquid.

The pressure inside the small droplet depends on the droplet volume and the surfactant concentration. A typical test may have 0.8μL of solution spread to a spherical cap of radius 0.8mm and height ~0.4mm. Then the two principle radii at the spherical cap surface are the same, 1mm (sketched in Fig 3.5B). The pressure inside the sessile drop is approximately 70~100N/m^2 higher than the ambient pressure. It is on the same order of the capillary pressure of water in a circular hydrophilic tube of radius 1mm and contact angle 45°.

3.3.2 Elimination of corner flow

The corner flow can be minimized, and even prevented, in a variety of ways, such as by proper design of the inlet or nanowick configuration.

It is obvious that corner flow will vanish when the height of nanowicks tends to zero. Corner flow is limited by the side wall height and of course the capillary length.

For our in-air and on-earth experiments, the capillary length is on the order of a few millimeters, which is much greater than the tallest nanotubes (85μm) in our experiments. As a consequence, gravity is negligible in corner flow[*]. On a low aspect ratio nanowick (where the height of a nanowick is much smaller than its width), surface flow dominates corner flow, if the latter exist, and the corner flow becomes less important than the surface flow in terms of the volume flow rate. Figure 3.7 gives some examples of flow on two low aspect ratio nanowicks. The corner flow beside a 40μm-high 1.8mm-wide nanowick is approximately 15μm-thick. That beside a 3μm-high 100μm-wide nanowick is less than 4μm thick. The nanowick is illuminated from the side in Fig 3.7B. In contrast with built-in lighting, the wetted region is darker than the intact dry region there.

Corner flow is induced by the corner's shape and, consequently, the capillary pressure induced by the angle. These corners include both the in-plane nanotube-to-wafer contact corner and the out-of-plane concave corner of nanotube mat walls. Corner flow can be avoided by separating corners and flow, or by providing a negative Laplace pressure that contradicts the corner capillary pressure. That is, (i) preventing supply liquid from contacting corners at the inlet by inputting flow far away from nanowick edges or from the through holes of the encapsulation, or (ii) induce concave curvature in the supply droplet as in Fig 3.8.

In order to prevent supply liquid from contacting the corners, liquid in some tests is placed on an inlet auxiliary pad. The auxiliary pad is made of the same

---

[*] The state-of-the-art upper height limit of a nanotube forest is 2.5mm (Hata et al 2004), which is almost twice the PDMS capillary length — the smallest capillary length used in this work.

nanotube arrays and is in contact with a strip-shaped nanowick. A schematic diagram is given in Fig 3.6A. This initial design failed to eliminate liquid accumulation at the concave corner as in Fig 3.6B. The liquid seen at the corner, indicated by the arrow in Fig 3.6B, is only stored there and is not spreading outward along corners because of limited supplement. (This was learned after the experiment.) The liquid accumulation at the junction corner can be easily eliminated by smoothing the curve as in Fig 3.6C. Therefore, in order to eliminate liquid loss into concave corners, circuits of nanowicks require rounding of the concave corners on the liquid transport pathway, in contrast to the counterpart chip design in the semiconductor industry.

3.4 Flow progression

3.4.1 Surface flow and vertical seeping

When corner flow is eliminated, liquid placed on top of the nanowick will first flow through the asperities of the tip surface, and then seep into the nanowick along the nanotube long axis from the top tip surface to the bottom wafer surface (as sketched in Fig 3.3A&B). The speed of initial surface spreading is on the order of millimeters per second. The speed of vertical seeping is on the order of 10μm/sec when air is trapped within the nanotubes.

The trapped air under surface liquid films prevents liquid from moving all the way to the bottom in some regions. It forms large bubbles in nanotube forests and these bubbles appear isolated circular black holes in Fig 3.6B, 3.12A, and 3.13B. Further evidence of these bubbles is that they will grow and deform the nanotubes at their border, when heated with laser light, because of the liquid-gas surface tension

present there. It takes much longer, tens of seconds, to fill in the black holes, because liquid will have to absorb the air or work against the pressure in the bubbles. The black holes (trapped bubbles) last longer under a stagnant bulky liquid drop (Fig 3.6B) than under a thin moving film (Fig 3.12A). In Fig 3.12A, upstream wafer is already smoothly covered by liquid in contrast to the black holes downstream.

The average speed of vertical seeping is measured by creating small windows on nanowicks to track the arrival time of surface flow. Time for vertical imbibition is counted from this reference time until an earliest nearby solid signal appears on the bottom. “Solid” here means half of upstream intensity. The growth defects in nanotube arrays can also be employed as such windows.

3.4.2 Transition to lateral interstitial wicking

Transition from surface dominant flow to interstitial dominant flow takes place in two flavors, depending on how surface flow slows down.

When surface flow slows down gradually to a speed on the same order as that of vertical penetration, air inside the nanowick has enough time to be displaced. Consequently, there are no trapped bubbles at this stage and the liquid moves smoothly inside the nanotube forest. In this transition, solution still moves from top surface to bottom wafer along the nanotube’s long axis. The liquid interface in the nanotube matrix is still inclined. Consequently, there is a cloud, out of the focal plane, ahead of the focal fluorescence border as shown in Fig 3.13A, due to the opaqueness of nanotubes. (The concentration gradient of fluorescein can also contribute part of the intensity gradient.) This becomes clearer when compared with the color gradient

in Fig 3.12B, where the border is within the focal plane and the liquid edge appears sharp.

The other transition format occurs on the front of a halting surface flow, which is often braked to a stop. The transition is described as *diving-in*, because liquid appears suddenly at the front in the bottom view as sketched in Fig 3.3C. Diving, combining vertical wicking with lateral expansion, is a transient but distinct transitional stage. It has been seen on both radial and on-strip spreading when supply liquid meets another outlet. One could argue that liquid can displace air more easily at the pressure-free front to cause diving. But pressure-free liquid edges are also present along nanowick side walls where vertical imbibition is actually slower than inside. The detail and mechanism for diving-in is not clear to the author, who assumes that the dynamics of a triple-phase contact line contributes to this effect. Two horns by nanowick sidewalls appear in this stage at the front as shown in Fig 3.13B. In radial spreading, dive-in liquid first appears on discrete dots of an arc and then submerges the whole arc.

The actual time required to dive is not currently measurable because of the difficulty in establishing a reference time. Based on liquid rising in angular capillary tubes[5], it takes an aqueous surfactant solution* approximately 0.1 second to travel from the top surface down to the bottom wafer on a 60μm high nanowick according to Washburn's law. Other data related to the diving mechanism shows that the speed of pure water climbing a single nanotube is on the order of 30m/s at start[55] from

---

* Surface tension is approximately 40mN/m, viscosity is 10^{-3}Pa·s, contact angle is around 80°, and the radius for degree of confinement is approximately 40nm.

molecular dynamics simulation, and the slip length for flow along the nanotube long axis is more than two orders of magnitude larger than the transverse flow[61].

3.4.3 Typical observations of lateral interstitial flow

In lateral interstitial flow, liquid is in contact with the bottom wafer when passing nanotube arrays. As a result there is no trapped air or bubbles. An example is given in Fig 3.12B, where the front displaces like a piston. The light intensity gradient seen on the front here results from the fluorescein concentration gradient. The concentration gradient results from the faster adsorption of fluorescein molecules onto the high surface-to-volume ratio nanotube bed and the slow diffusion rate in nanopores. Further discussion about concentration gradient is in Section 5.2.

Due to the high viscosity and tapering of surfactant concentration at the front, piston-like displacement of interstitial front as in Fig 3.12B is transient. The typical observation for the next stage is that liquid invades part of the nanowick area and leaves the other part untouched. Partial invasion after piston-like interstitial flow has been seen as finger-like invasion, or edge flow.

In finger-like invasion, fingers first form on the surface of nanotube tips and then seep into the interstices. The front of the surfactant solution on the surface may break into fingers due to the instability at the leading edge. The value of this instability wavelength is not studied in this work. Fingering may also be induced by topological heterogeneity of the surface. These fingers enhance the flow underneath by the curvature-induced Laplace pressure as shown in Fig 3.16.

Edge flow, seen as interstitial flow, preferentially runs along the edges of a nanowick, exemplified in Fig 3.15. The edge flow might employ nanowick sidewalls as a pathway to supply liquid and to lower the viscous drag. This is inferred from the co-existence of bulky liquid in contact with the sidewalls upstream, such as corner flow. But this work is not able to distinguish a thin film on the sidewalls. Even if it does exist, detection with the current setup is still a challenge.

3.5 Control experiments for corner flow and surface flow

3.5.1 Corner flow

Corner flow beside the solid step can develop without surface flow or interstitial flow. As a control experiment, corner flow is tested on solid steps made of photoresist. The solid steps have the external configuration of nanowicks but have no porous conformation inside. An example is given in Fig 3.9A. The gold-colored strip is a 10μm-high and 100μm-wide step. There is no surface flow on the smooth photoresist top surface. In comparison, corner flow beside nanowicks is illustrated in Fig 3.9B, where the black strip is the top view of a 40μm-high and 100μm-wide nanowick. The corner flow beside nanowicks looks similar to the flow along the solid step initially, except that surface flow progresses simultaneously on top. In the long run, different boundary conditions from the surface flow take effect.

The corner flow along a nanowick receives part of its liquid supply from the top surface on the first 2mm closest to the supply droplet. This cross-sectional flow is induced by imbalanced Laplace pressure. The cross-sectional profile for surface flow in the absence of corner flow and interstitial flow should be parabolic[15]. And the

cross-sectional profile for corner flow without the other two should be concave[46]. If surface flow is in direct contact with corner flow, these two opposite curvature are not in concert with each other. Therefore corner flow gives in and adapts a convex shape to live in harmony with the positive pressure in the supply droplet and the surface flow on approximately the first 2mm along the rivulet. Figure 3.11A sketches the initial velocity profile for cross-sectional flow. This is only observed indirectly through the maximal reach of corner flow on a wafer surface. Corner flow on the first 2mm appears narrower than the following.

3.5.2 Surface flow

At later stages, surface flow on nanowicks become faster than corner flow because of the pulling force from interstitial flow. An example of surface flow independent of corner flow is given in Fig 3.8. Triton solution (0.1wt%) is deposited on the digit "3" and migrated from left to right on the black nanowick. The time interval between the two frames there is 27 seconds; the indent downstream in B is entailed on by interstitial flow.

Surface flow can progress, provided similar surface roughness exists, when both interstitial flow and corner flow are minimized. A control experiment is done with rough surfaces made of sparse short nanotubes. The height of the nanotubes is no more than a few microns. Micrographs of such a surface are given in Fig 2.9. An example of flow on it is given in Fig 3.10C, where the bulky liquid is smooth, the surface film covers the tips of asperities, and the progressive front, darker than the surface film, leads the flow.

The same solution on smooth surfaces is not able to spread along the strip surface. ("Smooth" here refers to greatly reduced roughness.) Such control surfaces are made with photolithography. An example is given in Fig 3.10A.

The catalyst surface under the nanowicks has a roughness of a few nanometers. It is the only continuous lateral surface for an ideally grown nanowick. It is made of hydrophilic iron sinters; the oxide surface underneath is also hydrophilic. Appendix C explains why liquid can be seen through the catalyst layer. The control experiment proves that there is no tangible rivulet on such a catalyst strip, as shown in Fig 3.10B.

3.6 Fractal wicking at low concentration

Fractal interstitial wicking is observed at stagnant liquid edges, when an aqueous droplet with very low surfactant concentration is pinned and unable to spread itself on a nanowick top surface. Fractal wicking refers to the flow that branches randomly at front while moving forward inside the nanotube forest, as shown in Fig 3.14. Top view of fractal branching in Fig 3.14B, by courtesy of Elijah Sansom, is the first record of wicking phenomena in a nanotube forest.

Fractal wicking can carry liquid hundreds of microns away. The fractal front has been observed with water, 1/2 cmc SDS on 30μm high nanotube mats, and 2/3 cmc Triton on 3μm mats. (SDS cmc is ~8.3mM and Triton cmc is ~0.23mM.) The two concentrations were tested without the addition of fluorescein, while water always has unknown contaminants. Due to the limited number of available nanowicks, the author could not study the concentration effects parametrically. It is not clear whether the

height of a nanowick influences the branching behavior or other interstitial flow formats.

Spreading force for low surfactant solution is small, but being close to the supply liquid offers low viscous drag for liquid to extend. Low viscous drag introduces viscous instability and leads to the fractal phenomena. Section 5.4.3 will further discuss the competitive forces in nanowicking.

Chapter 4

TRANSPORT RATE ON NANOWICKS

Flow on nanowicks can first be categorized by spatial location: corner flow, surface flow, and interstitial flow, as illustrated in Chapter 3. Previous investigators have studied each of these isolated formats in their expertise, and their work enlightens this work in a variety of ways. This chapter describes the temporal scaling for each flow format at certain stages, benefiting from these established works.

4.1 Background

4.1.1 Washburn's law for an interface rising in capillary tubes

The temporal scaling of an interface rising in a capillary tube was first studied by Washburn (1921) [(64)] based on the fundamental equations of capillarity and wetting by Young (1805) and Laplace (1806). If we consider a horizontal capillary tube, neglect inertia because viscosity dominates, and replace the pressure difference in Poiseuille law with the wetting pressure drop at the liquid front, then the average velocity

$$\frac{dL}{dt} = V = \frac{r^2}{8\eta} \cdot \left(-\frac{dP}{dx} \right) = \frac{r^2}{8\eta} \cdot \frac{2\gamma \cos\theta}{r} \cdot \frac{1}{L} \qquad (1.3.2A)$$

where L is the liquid penetration length into the capillary. Solve L from the

differential equation 1.3.2A,

$$L^2 = \frac{\gamma \cos\theta}{2\eta} \cdot rt \qquad (1.3.2B)$$

The linear relationship of L^2 to t given in Eq. 1.3.2B (or the linearity of L to $\sqrt{t}$) is often referred to as Washburn's law. In the expression of L=K$\sqrt{t}$, K is named the *penetration rate coefficient* for the Washburn relationship. The gravity and inertia are neglected during its derivation. Albeit some controversial observations exist[8, 25, 54], Washburn's law and its extension have been obeyed and accepted in a variety of systems[23, 32, 37, 48, 51]. Two key conditions for the system to obey Washburn behavior are (i) a constant pressure drop acting from the reservoir to the advancing front; (ii) unidirectional flow according to the Poiseuille law.

Unidirectional flow in open channels, such as a V-shaped groove surface, or a strip on a flat surface that is easier to wet than other areas chemically, has been seen to follow the Washburn relationship[34, 46, 47]. The flow in both cases can be solved with similarity transformation[46] for appropriate boundary conditions. These boundary conditions include (i) a constant liquid height at entry (which would correspond to spreading from a reservoir), (ii) the liquid free surface within the groove sidewalls, (iii) an arbitrary contact angle at the strip edges. The similarity transformation shows that the position of the wetting front is proportional to $\sqrt{Dt}$, where D is a diffusion coefficient, proportional to the ratio of the liquid-vapour surface tension to viscosity.

4.1.2 Early and late stages

The Washburn solution, $L \propto \sqrt{t}$, has a singular point at t=0, i.e. $v \rightarrow \infty$ as $t \rightarrow 0$. This is because the velocity field used in solving for the viscous force is not valid initially. At the beginning of liquid impregnation when time scales are small, gravity and viscous effects are much smaller than momentum and capillary forces. Consequently, the early stage for capillary flow is a momentum regime. A linear relationship that states the penetration length is linear with time can be derived from Newton's second law for the early stage[17],

$$h = \sqrt{\frac{2\gamma \cos\theta}{\rho R}} \cdot t \ .$$

Therefore impregnation velocity is constant at the entrance, as the molecular dynamic simulation result shows for small time scale nanotube imbibition[54].

The transition time from inertia regime to viscous regime is dimensionally $\rho R^2/\eta$. The transition time is on the order of a second for water in a millimeter tube and can be on the order of minutes in the absence of gravity, where the capillary length, a limiting factor of R, can be bigger. The flow around a 3μm-high 100μm-wide wick is no more than 108μm wide. Consequently the transition time is on the order of 0.01 second or less. But the flow around 60μm high wicks can easily spread to 0.5mm wide. Therefore the first measured point may be recorded in the momentum regime. Despite the short transition time, the large entrance impregnation velocity can significantly shift the reference point in Washburn's relationship. [17, 32]

In the absence of a reservoir, the rate of spreading at late stages can be much slower[63]. There is no one single power law applicable to all late stages. On flat

surfaces, surface tension driven one-dimensional spreading scales as $L \sim t^{1/7}$.[56] In V-grooves, $L \sim t^{2/5}$.[63] And similarly, inside nanowick interstices, $L \sim t^{1/4}$.

As a result, the prediction for non-volatile flow is that the spreading rate should progress in a series of power laws:

(i) $L \sim t$ (a very short momentum regime)

(ii) $L \sim t^{1/2}$ (a Washburn-like law)

(iii) $L \sim t^{2/5}$ (as liquid becomes confined to top asperities)

(iv) $L \sim t^{1/4}$ (as liquid becomes confined to nanotube interstices)

4.2 Surface flow and corner flow

4.2.1 Washburn regime and penetration rate on nanowicks

Experiments on nanowicks confirm that the Washburn relation fits the major corner flow and surface flow except at the early and late stages. Washburn behavior fitting curves ($t \sim L^2$, t is time and L is liquid front position) for two different nanowicks is shown in Fig 4.1. Because the last few points and occasionally the first point in measured data are under different mechanisms, they are omitted from the fit. The binomial fit for the 100μm nanowick is t=4.90 L^2 +1.93 L+ 0.01, and for the 66μm nanowick is t=4.30 L^2 +2.14 L+ 0.16. The penetration rate coefficient (K in L=K$\sqrt{t}$) can be derived from the binomial fit. The curves can be translated horizontally and vertically by the reference start point of observation. It is the slope and curvature that reflect flow nature.

In the presence of corner flow on 60μm high nanowicks, the penetration rate of 0.1% Triton solution achieves its minimum (0.45 cm $sec^{-1/2}$) on 100μm wide nanowicks, in comparison with other width 35μm, 66μm, 200 μm and 1500 μm, as plotted in Fig 4.5. But the data may be suspect since the inlet condition is not well controlled— the 1.5mm strip (the last point in logarithm scale inset graph) has far more input liquid than the other thin strips.

The penetration rate for the same solution on a 100μm -wide but 3μm-high nanowick is smaller (0.19 cm $sec^{-1/2}$). The penetration rate for PDMS on a 200μm -wide and 40μm-high nanowick is even smaller, 0.049 cm $sec^{-1/2}$, for the first 40 seconds when data can fit into the Washburn behavior. (Refer to the next section for PDMS flow.)

Correlation coefficients (R) for binomial regression curves and experimental data are high ($R^2 > 0.9995$) in all experiments under microscope.

4.2.2 PDMS flow

PDMS — poly(dimethyl-siloxane) — is briefly tested to eliminate the complexity introduced by bi-mixture and evaporation. PDMS is considered an ideal liquid for wetting experiments because it is non-volatile with low contamination. (PDMS is immune to self contamination due to its low surface tension.)

Pure PDMS spreads faster than 0.1% Triton-X solution on the *wafer* surface, exempted by comparing Fig 4.8A with the sharp transition regime of Fig 3.4. Because of fast spreading on the wafer, PDMS does not hold high curvature nor high inside

Laplace pressure. Consequently, the spreading of PDMS along nanowicks is actually *slower* than that of aqueous solution.

Furthermore, PDMS never stops spreading, because there is no evaporation, while the aqueous solution dries up eventually.

Another main difference is that no trapped air bubbles are observed for the vertical interstitial flow (Fig 4.8D) because of the slow surface flow on nanowicks and because the low surface tension of PDMS itself improves the flow along the nanotubes.

The spreading of PDMS follows the power prediction for all stages. Flow slows from $t^{1/2}$, to $t^{2/5}$, and then to $t^{1/4}$ gradually. The raw data is shown in Fig 4.9.

4.2.3 Reflow test

The speed drops from 6.7mm/sec for flow on the intact nanowick to 1.9mm/sec for the once treated nanowick. This big drop results from the roughness change.

After a nanowick is tested with flow, its configuration is permanently changed by the surface tension of the liquid. We refer to the nanotubes that have already been exposed to liquid flow as liquid-treated nanotubes. Treated nanowicks have different configurations in height, interspaces, and top surface roughness (see Fig 4.6 for a comparison). Nest cluster sizes and patterns depend on liquid film instability, and surface tension action around the local nanotubes. The interstices are reduced and the pre-liquid treatment micron-scale roughness is enlarged greatly.

This reconfiguration after the first cycle of wetting and drying has only subtle changes during subsequent reflow tests. Therefore, the roughness — the cluster configuration of nanotube arrays — stays almost invariant for following wet-and-dry treatment cycles with the same liquid. The more flow cycles the nanowicks are tested for, the more surfactant molecules are adsorbed onto the nanotube surface. Surfactant molecules may even form thin films and block the interstices. Consequently, the speed changes a little for reflow tests.

Changes in flow behavior with the number of liquid treatments on a nanowick are shown in Fig 4.7. The curves there are tested with the same solution (0.1wt% Triton). Pure water is able to spread on treated nanowicks at a slower speed. The corner flow effect can be neglected in this nanowick, whose width is one order of magnitude larger than its height.

4.3 Average spreading rate

Early-stage speed on 1.5mm-wide 60μm-high nanowicks for the first two seconds is 6.7mm/sec as in Fig 4.2. Early-stage speed on a 100μm-wide 3μm-high nanowick is on the order of 1.5mm/s as shown in Fig 4.3.

Late-stage speed for interstitial wicking of surfactant aqueous solution can vary from a few microns per second to hundreds of microns per second (1–100μm/sec), depending heavily on solution concentration and boundary conditions from surface flow and corner flow. The spontaneous flow becomes faster when a new outward stress is created by a concentration gradient. This outward force is further discussed in Section 5.2. Evaporation greatly affects the late-stage speed. This is further discussed

in Section 4.5.1. Two examples of speed measurement of fingering wicking are given in Fig 4.4. The speed of fractal wicking and edge wicking is similar.

4.4 No-slip condition

It is known that the macroscopic no-slip boundary condition may break at the small scale.[13, 70] But our spontaneous flow has a relatively low shear rate compared to the established apparent slip flow[9]: the slip length at a shear rate of 10^5 s^{-1} is approximately 25nm for pressure-gradient-driven pure water flow through hydrophobic micro channels, while that at 10^4 s^{-1} may be no more than 1nm. The speed of surface flow on nanowicks is on the order of 1cm/sec or less, and the height of the liquid film is on the order of 10μm. Accordingly, the shear rate is on the order of 10^3 s^{-1} or less. This shear rate should not induce apparent slip flow.

Besides the high shear rate induced slip velocity, there exists another mechanism for concentrated surfactant solutions, where the adsorbed surfactant on the pore surface forms a mobile admicelle[2]. This work doesn't use concentrated surfactant solution. Consequently, mobile admicelles are neglected.

Additionally, molecular dynamic simulations of flow passing carbon nanotube arrays[61] give a slip length of 0.49nm for 2.50nm tubes in a 16.4nm lattice at a flow speed of 50 m/s. The spontaneous flow speed on nanowicks is two orders of magnitude smaller. Therefore, all slip phenomena along solid surfaces in surface flow or interstitial flow are neglected. (Trapped air under surface flow allows slip on the air portion.)

4.5 Other unaddressed parameters and limitations of this work

4.5.1 Evaporation

When a nanowick is not encapsulated, flow is in an open system, and evaporation significantly changes the surfactant concentration. This greatly affects the late-stage wicking, especially for low surfactant input, because surface tension changes faster with surfactant concentration when below cmc. As explained before, edge flow or finger invasion is observed at late stages of flow progression. However, corner flow and surface flow have been observed to resume themselves from edge flow and dash millimeters in the last 20 seconds right before all liquid dries up. The author just imagined the cause and did not systematically study this behavior. As evaporation goes on, liquid spreading properties change, as well as the inlet conditions such as liquid height and pressure head at entry. These changes lead to the aforementioned resuming of flow.

The resuming flow could be particular useful to portable chemical analysis systems because it rapidly pumps liquid into the nanowick, and its span (~1mm) is detectable with naked eyes.

4.5.2 Temperature

Evaporation may lower the temperature by 3°C in a layer of thickness about 500μm immediately below the interface.[62] And fluorescein excitation light may increase local temperature by 4°C (measured with a thermocouple). This work does

not address the issues associated with temperature change nor accompanying changes in physical parameters.

4.5.3 Continuous fluid media

The fluid medium is assumed to be continuous in this work. Molecular dynamic simulations of water flow through an array of single-walled carbon nanotubes find drag coefficients in reasonable agreement with the macroscopic Stokes-Oseen solution.[61]

4.5.4 Other parameters for wetting

The wetting properties of nanowicks are assumed to be invariant in terms of the hydration state of solid surfaces, temperature, ionic strength and pH value effect. These may affect wetting properties.[10, 12] For example, because OH groups introduce negative charges on the solid, the contact angle is 0° for water on fully hydroxylated quartz and 45° on completely dehydroxylated quartz. This work assumes that all solid surfaces are dehydroxylated because of the sub-atmospheric pressure growth process at high temperature and sample storage in desiccators; nevertheless, all experiments are performed in ambient room conditions. The dynamic wetting, how velocity and viscosity affect the rate of wetting[7], is neglected.

Despite all experimental complexity, there is no theoretical work that can predict everything without experimental support.

Chapter 5

FORCES INVOLVED IN INTERSTITIAL WICKING

The author discovered that the Marangoni force (Section 5.1 and 5.2) drives the spontaneous lateral interstitial flow, which enables nanowicks to carry reactive agents or sieve molecules by size. And the author has not crossed any reference on the Marangoni effect in wicking. Surface tension, which significantly alters the nanowick configuration, can be employed to detect liquid properties and flow history without direct observation of the liquid. Section 5.3 exemplifies the trace of liquid on nanowicks by surface tension. Section 5.4 characterizes the front observations into four domains in term of force competition, emulating Lenormand's phase diagram (1990) for flow in porous media.

5.1 Background for Marangoni force

5.1.1 Surfactant diffusion in small pores

Acceleration of capillary impregnation of a hydrophobic porous system by the addition of a surfactant incorporates the diffusion mechanism of the surfactant into the wetting problem.[11] The diffusion mechanisms in hydrophobic and hydrophilic capillaries are different.

In hydrophobic capillaries, the advancing speed of the liquid front is limited by the diffusion rate of the surfactant. Surfactant molecules have to diffuse in advance of the wetting front to enable liquid to impregnate with capillary force.[11]

In hydrophilic tubes, pure water is capable of advancing without the aid of a surfactant. If the mean pore size is smaller than a critical value, surfactant molecules cannot diffuse to the liquid advancing front. Consequently, liquid imbibition in such small pores is not influenced by the presence of surfactants. This critical value of pore size is determined by the adsorption of the surfactant molecules onto the inner surface of the pores. The critical value is between 0.45μm and 3μm for sodium dodecyl sulphate (SDS) solution in nitrocellulose membranes.[52]

5.1.2 Surfactant adsorption

Surfactants adsorb strongly to graphite. Adsorption increases with increasing concentration up to the critical micellar concentration (cmc), after which it remains fairly constant. Above the critical micellar concentration, sodium dodecyl sulphate (SDS) self-assembles into supramolecular structures made of rolled-up half-cylinders on the nanotube surface. Depending on the symmetry and the diameter of the carbon nanotube, rings, helices, and double helices are observed. [45] Industrial grade poly(oxyethylene) surfactants contain mixtures of alkyl chain lengths and ionic impurity. Poly-dispersed surfactants usually form an adsorption multilayer on graphite, while the pure monodispersed non-ionic surfactant can construct a single layer with surfactant molecules forming highly aligned hemi-cylinder stripes on flat graphite surface, spacing 5.6±0.3nm apart.[41, 42]

Adsorption of surfactants onto carbon nanotubes enhances the concentration gradient in the advancing front by limited diffusion.

5.1.3 Marangoni effects

Other than restoring balanced surface tension at the three-phase contact line, another mechanism of droplet spreading is due to the Marangoni effect (1821)[35]. It has long been known that the spatial variation in surface tension at a liquid/gas surface results in added tangential stresses at the surface; this results in a surface traction that acts on the adjoining fluid, giving rise to the fluid motion in the underlying bulk liquid. The tangential force per unit area is given by the surface tension gradient on the free surface, and liquid tends to move in a direction from a low to a high surface tension. If the liquid/air surface tension is greater at the front surface of the spreading drop than in the center of the drop, then the difference in surface tension establishes a gradient and will create Marangoni flow.

The Marangoni tangent outward stress on the free surface can result from (i) surfactant concentration gradient, (ii) a bi-mixture solution with one component evaporating faster than the other, and (iii) temperature difference.

The Marangoni stress induced by concentration gradient, in a one-dimensional case, can be expressed as

$$\tau = \frac{d\sigma}{dx} = \frac{d\sigma}{dC} \cdot \frac{dC}{dx} .$$

Where shear stress (τ) is on the free surface, along the flow axis (x), and points towards higher surface tension. Surface tension (σ) is a function of surfactant concentration (C).

5.2 Marangoni force in nanowicking

5.2.1 Observations

Fluorescein concentration varies dramatically near the front. There are very few fluorescein molecules at the front. Surfactant concentration can not be observed directly, but one can infer that a surfactant behaves similarly to fluorescein. Therefore very low surfactant water sees a hydrophobic surface at front. Three-phase contact line disparity is not enough to drive the interstitial flow. A compensatory wetting force is created by the steep concentration gradient near the front. This steep gradient results from

(i) fast adsorption on to graphene,

(ii) large surface-to-volume ratio in nanowicks,

(iii) slow diffusion in nanopores (surfactant molecules cannot get to the front fast enough).

The front position of interstitial flow can be detected with surface tension action. Shrinking occurs as liquid arrives at the sidewall of a nanowick, and the deformation remains after liquid evaporation. An example of interstitial front indicated by the shrinkage at sidewalls is given in Fig 5.1, pointed by blue arrows. This position can be confirmed with the brightness profile scanned on the line as illustrated. The light intensity change in Fig 5.1 corresponds to concentration changes, not thinning of the liquid layer, because the liquid thickness there should be on the order of microns and more, in order to mechanically deform the nanotubes and open valleys as in Fig 5.5. Cracks in nanotube arrays form along the edges of wetted

regions. The contrast of the dark grey front beyond fluorescence and black intact region in Fig 5.5 is improved in Photoshop.

The concentration-gradient-induced surface shear stress is on the order of $0.3\sim0.4 nN/m^2$. This Marangoni outward stress is the main driving force for lateral interstitial flow where almost pure water sees the front interface.

In addition, Marangoni-stress-induced convection cells are observed in the surface flow for reflow tests on a 1.5mm wide nanowick with 4μL 0.1% Trition solution, as shown in Fig 5.2A, in comparison with structure left by non-convectional flow in Fig 5.2B. Because there exist convection cells, the surface flow film is likely bigger than 100μm in this case. By focus adjustment under optical microscopes, the film is likely thinner than 500μm.

5.2.2 Control experiments

We can remove free top surface effects by encapsulating the nanowick into a channel. As a result, the top surface flow and the free-surface effects, such as Marangoni effects, and mass and energy loss due to evaporation, can be minimized. Encapsulation also provides a simple way to adjust the ambient pressure around the nanowicks.

Perfect alignment of nanotubes inside the channel requires growing the nanotubes inside the channel directly, which could also eliminate corner flow. Because of the time constraints with collaborators, we chose a simple coarse approach—post-aligning nanowicks into a channel. The gap between the side walls of the channel and the nanowick cannot be avoided.

Due to wall shear and the absence of free-surface Marangoni forces along the flow axis, the speed of encapsulated flow (including all types of flow) is slower than free-surface flow. The speed of interstitial flow is on the order of a few microns per *minute* and less. In addition, the flow is very sensitive to the high-energy fluorescein excitation light. The increase (3–5°C) in temperature improves the liquid mobility between walls when the channel is open, and pushes the liquid to withdraw in a sealed channel by the incremental pressure resulting from evaporation. "Open" refers to having a through hole downstream; "sealed" here means that there is only one through hole upstream for the channel where liquid is input. A snap shot of flow in an open channel is given in Fig 5.4. The nanowick is 100μm wide and 50μm high. The channel, 180μm wide and 50μm high, is made of RTV with typical soft-lithography techniques. The RTV layer is 2mm thick. The 1:10 RTV channel is soft-baked for 20 minutes before being pressed onto the nanowick under a mask aligner. The nanowick is then peeled off the silicon wafer with the RTV channel. The RTV channel with the nanowick inside is placed on a glass slide and hard-baked to cure.[*]

In order to prove that pure water may advance ahead of other components in narrow pores, a control experiment is conducted in wicking of fluorescein solution through a thin film of polyacrylamide, whose average pore size is 20nm. This pore size is on the same order as the void space (40nm) between nanotube arrays for most experiments in this work. Water *does* advance far ahead of the visible fluorescein gradient and moistens the mildew growth as indicated with the arrow in Fig 5.3A. The curling is induced by surface tension and structure (there is a plastic backbone on one

---

[*] The peel-off procedure is not necessary and actually generates a small gap between nanowick and glass. It was done only because there were many nanowicks on that wafer for other tests

side of the polyacrylamide). The same action can happen on dense nanotube arrays as in Fig 5.3B. The action of surface forces enables analysis of liquid properties without direct observations of the flow, as in the following section.

5.3 Decipher flow by the front imprint

Flow leaves an imprint by deforming the flexible nanotubes. The imprint of liquid on nanotube arrays reflects the wetting history, therefore enabling diagnosis of liquid properties without direct observation of the liquid. How liquid leaves the imprint by surface tension is explained in Section 3.2.3. The imprint can be viewed optically or in SEM at greater resolution. The trace of liquid not only enables high-resolution morphological analysis of liquid front, but also allows liquid diagnosis anytime after sampling because the robust imprint remains. The match of flow with its imprint is illustrated in Fig 5.5.

The imprints on low-aspect-ratio nanowicks more easily recover flow history than those on narrow and tall nanowicks. Two imprints on 3μm high nanowicks are given for high and low surfactant flow in Fig 5.6. The high surfactant flow has a smooth parabolic front, indicating well-developed surface flow. The low surfactant flow is full of cracks near the front, which is a sign of fractal wicking. The distance from input to front is good proof too—the high surfactant flow being centimeters away from the input droplet location. The front of the low surfactant flow is very close (1mm) to input.

Imprints on high-aspect-ratio nanowick are greatly affected by corner flow. If corner flow resumes after edge flow, the nanowick tends to curl up in the region

where liquid is pumped in twice, as shown in Fig 5.3B. The high-aspect-ratio nanowick is pulled towards center to form a ridge, in contrast to multiple openings in a low-aspect-ratio nanowick. The ridge structure in front is demonstrated in Fig 5.7.

Flow is observed sensing conformation changes in nanotube arrays. This is very distinct through investigation of flow imprint in SEM. And it is hard to tell by optical observations because of the resolution limitation of optical microscopes. Fast spreading is induced by the alteration of the nanotube array configuration. Two examples are given in Fig 5.8: A: a zigzag front with leading points close to the configuration difference zone and the edges; B: fast spreading along the center border for different nanotube arrays on two sides.

5.4 Front dynamics in comparison with liquid inside porous media

Experimental observations of flow in this work are on a scale that is much larger than the pore size. The recorded fractal fronts are a direct proof of the discrete behavior of imbibition in pores. Lenormand summarized competition of wetting forces and viscous drag, in the field of flow in porous media, into phase diagrams. The nanotube arrays grown by Microdevices Laboratory for this work have a small pore aspect ratio (~1.6). Consequently the lateral interstitial flow in nanotubes is compared with the phase diagram for imbibition in small aspect-ratio porous media.

5.4.1 Background of liquid flow in porous media

A common description of flow in porous media is Darcy's law:

$$\langle \boldsymbol{q} \rangle = -\frac{\kappa}{\eta}(\nabla \boldsymbol{P} - \rho \boldsymbol{g}) \qquad (1.6.1)$$

Where $\langle \boldsymbol{q} \rangle$ is the volume flow rate, κ and η are the permeability and viscosity respectively. Darcy's law is a foundation stone for several fields of study including groundwater hydrology, soil physics, and petroleum engineering. All parameters are observed over representative volume elements, i.e. the parameters are averaged over such a certain volume that their values do not change from one element to another. The equation ignores all fluctuation and pore topology effects. Consequently, it fails to predict discrete behaviors in porous flow.

Previous investigators classify flow sensitive to pore geometry details into drainage and imbibition. *Drainage* refers to the flow in which a non-wetting invading fluid displaces a wetting fluid, and the opposite case, *imbibition,* refers to the flow where a wetting fluid displaces a non-wetting fluid. The pore geometry details involved in determining liquid displacement in the porous system include the inside surface roughness of pores and <pore body>-to-<pore throat> aspect ratio. Figure 5.9 illustrate the high and low aspect ratio for pores.

Typically, slow drainage is characterized by piston-like motion inside the pores where the invading non-wetting fluid only enters a pore if the capillary pressure is equal to or greater than the threshold pressure of that pore. The threshold pressure corresponds to the capillary pressure in the narrowest part of the pore. Consequently the invading fluid in drainage chooses the largest throat. However, in imbibition, at low injection rate, the invading fluid will enter the most narrow pores before any other is considered. For large <pore body>-to-<pore throat> ratio, the main mechanism is the collapse of invading fluid in the smallest channel without entering

the pore; for small <pore body>-to-<pore throat> ratio, the wetting fluid invades the pore first and then the adjacent channels. In addition, the possibility of flow by film along the roughness of the walls leads to disconnected structures.[33]

For circular cylinders of radius r in square arrays of repeat unit distance d, the <pore body>-to-<pore throat> aspect ratio is:

$$\text{Pore Aspect Ratio} = \frac{\sqrt{2}d - 2r}{d - 2r} = \sqrt{2} + \frac{2\sqrt{2} - 2}{\left(\frac{d}{r} - 2\right)} .$$

The rule of thumb from the above formula is that the pore aspect ratio is larger for denser arrays.

Carbon nanotubes are almost smooth at the atomic scale, but there are many particulates on the catalyst layer of the bottom wafer. These particulates provide a nanoscale roughness and may enhance spreading with the roughness.

5.4.2 Background of Phase diagrams for liquid imbibition

Studies on the stability and existence of a liquid interface in porous media display the different transport behaviors as qualitative domains in three phase diagrams: one for drainage and two for imbibition.[1, 33] One phase diagram of imbibition is for large aspect-ratio pores, in which the main mechanism is wetting fluid flowing along the roughness of the walls, surrounding the solid grains, and collapsing in the narrow throat. This mechanism is also described as "pinch-off."[60] The other phase diagram of imbibition is for small aspect-ratio pores, where the main mechanism is pore invasion. During invasion of the wetting fluid, the pore throats are filled rapidly, as long as the meniscus from the pore body entirely touches the walls

around that throat. This displacement is analogous to a contact line moving on a rough surface.

The phase diagrams employ the capillary number (Ca=$V\eta/\gamma$) and the viscosity ratio (η/η_0) of the two fluids involved to illustrate the competition of viscous and capillary forces. (Note: η_0 is the viscosity of the defending fluid — air — in this work.)

At a high capillary number, there exist unstable and stable viscous domains for all three phase diagrams. The unstable viscous domain is observed as "capillary fingering" — formation of non-compact branched structures due to weak surface tension. The stable viscous domain is observed as "stable displacement" of the interface, which is insensitive to the structure details in the porous network.

At a very low capillary number, discontinuous formation of wetted domains are observed for both large and small aspect ratios because of the film flow in the roughness on pore surfaces. At a small aspect ratio, the discontinuity is observed as disjointed clusters of the imbibing liquid. At a large aspect ratio, the discontinuity is observed as discrete wetting of pore throats.

There is an intermediate zone, observed as a "continuous capillary domain," for both imbibition phase diagrams. Due to the aforementioned mechanism, the continuous capillary domain in large aspect-ratio pore networks leaves isolated unfilled pores, while that in small aspect-ratio pore networks appears as a compact domain with well-defined interfaces reflecting the geometry of specially designed

porous networks, e.g., a compact wetted domain appears triangular in triangular arrays and square in square arrays.

5.4.3 Competitive domains of viscous and wetting forces

In the analog analysis, the viscous ratio in the phase diagram is mapped to viscous effective distance. The viscous ratio for this work is almost invariant:

$$M = \eta/\eta_0 \approx 10^{-3}\ \text{Pa·s} / 1.82\text{x}10^{-5}\ \text{Pa·s} = 55.$$

The viscous effect is reflected by the distance from the imbibing front interface to the bulky supply source. All observed fractal fronts are close to the surface flow, such that the viscous effective distance is small.

The capillary number in the phase diagram is replaced by effects from both wetting forces — capillary force and Marangoni force, say, $(\frac{V\eta}{\gamma}+\frac{\tau \cdot l}{\gamma})$. The augend is a capillary number and the addend is so-defined to correspond to the Marangoni effect, where τ is the Marangoni outward stress and l is the effective distance that τ acts on.

The new phase diagram for the interstitial flow in nanowicks is illustrated in Fig 5.10.

Four typical observations for imbibition in small aspect-ratio porous media are: (i) “capillary fingering,” (ii) “stable displacement” of the interface, (iii) disjointed clusters of the imbibing liquid, and (iv) a compact domain with well-defined interfaces that reflect the pore lattice particulars.

The first three behaviors have been observed as analog in nanowicking as exemplified in Fig 5.11. The third case—disjointed wetted regions—are observed in low surfactant solution or pure water wetting experiments. Liquid may flow in film along the hydrophilic supporting wafer, and aggregate at random locations to form small isolated wetting regions that are discontinuous from each other. In the case of small pore aspect ratio, high surface tension keeps liquid in the cluster.*

The fourth case—that flow sees pore lattice details—is not observed, because (a) nanotube arrays may not be regular enough to present the phenomena, and (b) the boundary conditions are more likely the cause leading to the straight lines at the front (in Fig 5.8), rather than the competition of capillary force with viscous force, which is the reason for the "intermediate zone" behavior (iv).

* This may not be true for large pore aspect ratio.

Chapter 6

SUMMARY

This work experimentally presents studies of the spontaneous fluid transport along nanowicks. Our studies depict that liquid is conveyed through corner flow, surface flow, and interstitial flow through capillary force and the Marangoni effect. Delivery through wetting and spreading forces avoids the unreasonably large pressures required to push liquids through small channels and small interstices. The required pressure gradient increases as the inverse of the fourth power of the characteristic size: $\frac{dP}{dx} \sim \frac{\eta \cdot Q}{r^4}$.

The main course for corner flow and surface flow follows Washburn behavior, and can deliver liquid centimeters away from the input blob, with a speed on the order of millimeters per second, depending on the nanowick configuration and the amount of input liquid. The corner flow can be minimized, even eliminated, through proper nanowick and input design. Otherwise, corner flow interacts with surface flow in the first 2mm of the pathway closest to the input.

Interstitial flow dominates the late stage. It is driven by both capillary force and concentration-gradient-induced Marangoni force. The primary lateral spreading force for low-surfactant interstitial flow is the Marangoni force near the front. The concentration gradient is determined by two competing rates: surfactant diffusion in

solution and adsorption onto nanotube surfaces. The flow may wick hundreds of microns in seconds or tens of seconds.

A non-conventional advancing front may develop in the flow around nanowicks. They are seen as (i) Rayleigh instability induced fingering in surface flow on millimeter-wide nanowicks, (ii) viscous instability induced branching near almost-stagnant surface film at low surfactant concentration, and (iii) disjointed wetting domains at very low concentration.

Through this work, we have introduced a novel microfluidic device for liquid transport and possible chemical analysis.

The delivery function of nanowicks enables novel fluid transport devices running without any power input, moving parts, or external pump, in contrast with other fluid transport methods[14, 16, 43, 53] in the field of micro/nano-fluidics engineering. In addition, the interstitial flow exposes liquid to a large surface-to-volume ratio porous structure, which can be designed to carry catalyst and reactive agents or utilized as a sieving matrix for molecular separations (as in chromatography). Therefore the delivery and nanofibrous nature make nanowicks a good candidate for portable or disposable fluid sampling and analysis devices.

6.1 Summary of the work

- Designed nanowicks for liquid delivery on microfluidic devices

- Studied flow interaction with nanowicks

- Preliminarily characterized flow observations

- Discovered Marangoni driven flow through hydrophobic nanopores

6.2 Unaddressed questions

We have not addressed the following specific issues:

- Wicking behavior spectrum with surfactant concentration

- Physical parameter variations with evaporation, temperature, speed…

- Structure changes in nanotube arrays by surface tension (studied by Sansom)

- Wicking in other nanopillar arrays with different surface property and configuration

6.3 Potential applications

- Chemical analysis with fluid circuits (biomolecular filtration)

- Body-worn and disposable lab on a bandage

- Rate control of micro-combustion

- Tissue engineering on nanofiber matrices

- Microchip cooling circuits (capillary pumping loops)

Appendix A

Surface tension of some common liquids

Liquid	Surface tension γ (mN/m)
Helium (4K)	0.1
Silicone oils (PDMS)	~20
Acetone (20˚C)	24
Glycerol (20˚C)	63
Water (20˚C)	73
Water (100˚C)	58
Mercury (20˚C)	485
0.01wt% Triton-X100 Solution	52
0.1wt% Triton-X100 Solution	36

Appendix B

Surfactant fundamentals

Surfactants (surface active substances) have two parts with different affinities: a hydrophilic head, formed with soluble short chain of neutral units, or ions; and a hydrophobic tail, in most cases formed with one or more long aliphatic chain(s). As surfactant concentration increases above a certain *critical micellar concentration* (cmc), surfactant molecules will aggregate in volume to form micelles with their hydrophilic head on the micelle surface and hydrophobic tails inside to minimize the energy. They will also align themselves on the interfaces in order to minimize the energy. At the liquid/air interface, surfactant molecules form a monolayer with the hydrophilic head toward an aqueous environment and the hydrophobic tail toward the air. This surfactant monolayer lowers surface tension by interacting with water molecules at the surface, equalizing the forces to which those water molecules are subjected. On a hydrophobic flat solid surface, a similar monolayer can be formed for diluted solution; on a hydrophilic surface, a bilayer may be formed, similar to cell membrane structure but with hydrophilic tails pointing outside and hydrophobic heads inwards. Higher concentration solutions often form adsorption multilayer on a solid surface.

Surfactants are often added to reduce the surface tension of water and improve spreading. In general, the lower the surface tension of a liquid, the faster it spreads.

Addition of a surfactant to accelerate the imbibition makes sense, only if the resulting decrease in liquid/air interface tension prevails over the counteraction on a solid surface. A surfactant can always accelerate the imbibition of aqueous solutions in hydrophobic capillaries. But the addition of a surfactant into hydrophilic capillaries may result in more complex and even controversial results.

This work used industrial Triton X-100 (Sigma product-octylphenol ethylene oxide condensate), which is produced from octylphenol polymerized with ethylene oxide which has an average of 9.5 ethylene oxide units per molecule. The average molecular weight is 625; specific gravity is 1.065 at 25°C; and critical micellar concentration (cmc) is 0.22–0.24 mM; the general concentration used for biological sample is 0.01–0.1wt%, and biocompatibility can be as high as 0.5%. Surface tension for 0.01% Triton X-100 solution is 52mN/m and that for 0.1% is 36 mN/m, in comparison to water (0%) surface tension ~70mN/m.[49] Industrial Triton is only of 97% purity. The impurity is more likely to be ionic, which effects ion strength, produces a broad electric double layer, and generates a polydisperse system.

Sodium dodecyl sulphate (SDS) is a typical anionic surfactant. Its chemical formula is C12H25OSO3Na; molecular weight is 288.38; and cmc is around 8.3mM at 25˚C in the absence of any other additive. The Krafft point of SDS is around 16˚C [59]. The Krafft point of ionic surfactant is defined to be the temperature at which the solubility of the monomer becomes equal to cmc. Above the Krafft point, micelles begin to form provoking a rapid increase in the solubility of the surfactant as was first clearly described by Murray and Hartley in 1935. Below the Krafft point, solute will form crystals instead of micelles. All liquid properties, such as conductivity, viscosity, density, and scattering, have a transition region where micelles form. The critical

micellar concentration decreases from 8.47mM to 8.20mM as the temperature increases from 20˚C to 30˚C, and increases with temperatures over 30˚C.[30]

Appendix C

Thin films

A film on a solid has the interfacial energy on both the solid/liquid interface and the liquid/air surface ($\gamma_{SL}+\gamma_{LG}$). When the film becomes thinner than 100nm, the surface tension of bare solid to air (γ_{SG}) starts to emerge, and as the film thickness (e) tends to zero, solo solid surface energy (γ_{SG}) is expected. In bridging the above two extreme cases, overall interfacial energy has to be a function of the film thickness:

$$\text{Energy per surface area} = \gamma_{SL}+\gamma_{LG}+ P(e)$$

where $P(e) = 0$ when $e\rightarrow\infty$; $P(e) = S = \gamma_{SG} - \gamma_{SL} - \gamma_{LG}$ when $e=0$. Following Derjaguin's notation, *disjoining pressure* can be defined as:

$$\Pi(e) = -\frac{dP(e)}{de}$$

Or more generally, *disjoining pressure* can be defined as the first derivative of the Gibbs free energy (G) of the thin layer with respect to its thickness (e):

$$\Pi(e) = -\left.\frac{\partial G(e, P^0, T, \mu^i)}{\partial e}\right|_{P^0, T, \mu^i}$$

where P^0, T, μ^i are ambient pressure, temperature, and chemical potential of the i^{th} dissolved component. Disjoining pressure is a basic thermodynamic characteristic of

thin interlayers, where long-range forces come into play. The most important long-range force for oil is van der Waal's force. Water turns out to be much more complicated than oil: spontaneously charged layers at interfaces introduce electrostatic interactions.

Appendix D

Characteristics of porous structures

The interest in pore size distribution and surface area of porous media is linked to industrial adsorbents and catalyst supports. According to the International Union of Pure and Applied Chemistry (IUPAC), pores can be classified by their size into (i) macropores (> 50nm), (ii) mesopores (2–50nm), (iii) micropores (< 2nm), according mostly to nitrogen adsorption studies. In the case of gas adsorption, the micropore properties are based on the internal surface area; the macropore properties are based on the internal volume; the mesopore properties are determined by both internal surface area and internal volume. There are still other critical values for pore size. Below 10nm, the effective values of molar volume and surface tension require progressive adjustment with decrease in pore width. Below 0.7 nm (a rough number up to date), the physisorption of nitrogen and other small molecules is energetically driven through the overlap of intermolecular forces and therefore takes place at very low relative pressures. Consequently pores smaller than 0.7nm are termed ultramicropores, and pores in size of 0.7 – 2nm are termed supermicropores.[50]

Pore size classification for liquid is less established. A critical value, somewhere between 0.45 and 3μm, for sodium dodecyl sulphate (SDS) solution in nitrocellulose membranes, is suggested where the rate of solution imbibition becomes independent of the surfactant concentration in the feeding solution.[52]

From a topological point of view, a pore can be open, semi-open or closed depending on the connection to the surface of the porous body. Open pores can be a percolation path for fluid to penetrate from one side to another. In open ultramicropores, some small molecules can be energetically driven through the overlap of intermolecular forces, which enables selective separation. The connectivity or interconnection of the porous body refers to the continuous porous structure from one side to the opposite. A pore can be open only to one surface and not connected to any other surfaces. In that case, it is termed "semi-open." And a pore can be isolated from surfaces to be a "closed" pore. The closed pore cannot participate in the mass transfer process, but it can increase the thermal, electrical, and acoustic insulation properties of the solid and reduce its density. All pores reduce mechanical strength. Our nanotube array structure is completely open. A porous structure is considered "regular" if it can be divided into a number of systematically repeating fragments. When no systematically repeating fragments can be found locally anywhere, the porous structure is considered "random." If the average properties do not significantly differ from fragment to fragment, a porous body is called "homogeneous." Otherwise, it is "inhomogeneous" or "heterogeneous." Heterogeneous nanotube arrays are possible, usually prepared with e-beam lithography. Homogeneity and heterogeneity are a global view, while the regularity and randomness are a local view. Most practical and experimental realizations of liquid transport through a porous structure

consider the structure disorder media. Disorder first means the randomness from a local view, and may include heterogeneity. Since development of a range of uniform porous materials is still a challenging work, *regular* is used in a very broad sense.

References

1. Alava M, Dube M, Rost M. 2004. Imbibition in disordered media. *Advances in Physics* 53: 83-175
2. Bakx A, Timmerman A, Frens G. 2000. The flow of concentrated surfactant solutions through narrow capillaries. *Colloid and Polymer Science* 278: 418-24
3. Barber AH, Cohen SR, Wagner HD. 2004. Static and dynamic wetting measurements of single carbon nanotubes. *Physical Review Letters* 92
4. Berber S, Kwon YK, Tomanek D. 2000. Unusually high thermal conductivity of carbon nanotubes. *Physical Review Letters* 84: 4613-6
5. Bico J, Quere D. 2002. Rise of liquids and bubbles in angular capillary tubes. *Journal of Colloid and Interface Science* 247: 162-6
6. Bico J, Tordeux C, Quere D. 2001. Rough wetting. *Europhysics Letters* 55: 214-20
7. Blake TD, De Coninck J. 2002. The influence of solid-liquid interactions on dynamic wetting. *Advances in Colloid and Interface Science* 96: 21-36
8. Chibowski E, Perea-Carpio R. 2002. Problems of contact angle and solid surface free energy determination. *Advances in Colloid and Interface Science* 98: 245-64
9. Choi CH, Westin KJA, Breuer KS. 2003. Apparent slip flows in hydrophilic and hydrophobic microchannels. *Physics of Fluids* 15: 2897-902
10. Churaev NV. 1995. Contact Angles and Surface Forces. *Advances in Colloid and Interface Science* 58: 87-118
11. Churaev NV. 2000. *Liquid and vapor flows in porous bodies: surface phenomena*. Moscow: Gordon and breach science publishers
12. Churaev NV. 2003. Surface forces in wetting films. *Colloid Journal* 65: 263-74
13. Craig VSJ, Neto C, Williams DRM. 2001. Shear-dependent boundary slip in an aqueous Newtonian liquid. *Physical Review Letters* 8705
14. Darhuber AA, Troian SM. 2005. Principles of Microfluidic Actuation by Modulation of Surface Stresses. *Annual Review of Fluid Mechanics* 37
15. Darhuber AA, Troian SM, Reisner WW. 2001. Dynamics of capillary spreading along hydrophilic microstripes. *Physical Review E* 6403: art. no.-031603
16. Darhuber AA, Valentino JP, Troian SM, Wagner S. 2003. Thermocapillary actuation of droplets on chemically patterned surfaces by programmable microheater arrays. *Journal of Microelectromechanical Systems* 12: 873-9
17. de Gennes PG, Brochard-Wyart F, Quere D. 2004. *Capillarity and wetting phenomena: drops, bubbles, pearls, waves*. Paris: Springer

18. Dussaud AD, Adler PM, Lips A. 2003. Liquid transport in the networked microchannels of the skin surface. *Langmuir* 19: 7341-5
19. Fan JG, Tang XJ, Zhao YP. 2004. Water contact angles of vertically aligned Si nanorod arrays. *Nanotechnology* 15: 501-4
20. Fan SS, Chapline MG, Franklin NR, Tombler TW, Cassell AM, Dai HJ. 1999. Self-oriented regular arrays of carbon nanotubes and their field emission properties. *Science* 283: 512-4
21. Feng L, Li SH, Li YS, Li HJ, Zhang LJ, et al. 2002. Super-hydrophobic surfaces: From natural to artificial. *Advanced Materials* 14: 1857-60
22. Feynman RP. 1959. There's plenty of room at the bottom. *annual meeting of the American Physical Society at California Institute of Technology,*
23. Geromichalos D, Mugele F, Herminghaus S. 2002. Nonlocal dynamics of spontaneous imbibition fronts. *Physical Review Letters* 89
24. Hata K, Futaba DN, Mizuno K, Namai T, Yumura M, Iijima S. 2004. Water-assisted highly efficient synthesis of impurity-free single-waited carbon nanotubes. *Science* 306: 1362-4
25. Horvath VK, Stanley HE. 1995. Temporal Scaling of Interfaces Propagating in Porous-Media. *Physical Review E* 52: 5166-9
26. Huang ZP, Carnahan DL, Rybczynski J, Giersig M, Sennett M, et al. 2003. Growth of large periodic arrays of carbon nanotubes. *Applied Physics Letters* 82: 460-2
27. Huang ZP, Wang DZ, Wen JG, Sennett M, Gibson H, Ren ZF. 2002. Effect of nickel, iron and cobalt on growth of aligned carbon nanotubes. *Applied Physics a-Materials Science & Processing* 74: 387-91
28. Iijima S. 1991. Helical Microtubules of Graphitic Carbon. *Nature* 354: 56-8
29. Islam MS, Sharma S, Kamins TI, Williams RS. 2004. Ultrahigh-density silicon nanobridges formed between two vertical silicon surfaces. *Nanotechnology* 15: L5-L8
30. Junquera E, Pena L, Aicart E. 1994. Influence of Temperature on the Micellization of Sodium Dodecyl-Sulfate in Water from Speed of Sound Measurements. *Journal of Solution Chemistry* 23: 421-30
31. Kissa E. 1996. Wetting and wicking. *Textile Research Journal* 66: 660-8
32. Labajos-Broncano L, Gonzalez-Martin ML, Janczuk B, Bruque JM, Gonzalez-Garcia CM. 1999. Distance-time measurements in capillary penetration: Choice of the coordinate system. *Journal of Colloid and Interface Science* 211: 175-7
33. Lenormand R. 1990. Liquids in Porous-Media. *Journal of Physics-Condensed Matter* 2: SA79-SA88
34. Mann JA, Romero L, Rye RR, Yost FG. 1995. Flow of Simple Liquids Down Narrow-V Grooves. *Physical Review E* 52: 3967-72
35. Marangoni C. 1871. Ueber die AUSBREITUNG DER TROPFEN EINER fLUSSIGKEIT AUF DER OBERFLACHE EINER ANDEREN. *Annalen der Physik und Chemie* 143: 337
36. McHale G, Shirtcliffe NJ, Aqil S, Perry CC, Newton MI. 2004. Topography driven spreading. *Physical Review Letters* 93

37. Medina A, Perez-Rosales C, Pineda A, Higuera FJ. 2001. Imbibition in pieces of paper with different shapes. *Revista Mexicana De Fisica* 47: 537-41

38. Neimark AV. 1999. Thermodynamic equilibrium and stability of liquid films and droplets on fibers. *Journal of Adhesion Science and Technology* 13: 1137-54

39. Nikoobakht B, Michaels CA, Stranick SJ, Vaudin MD. 2004. Horizontal growth and in situ assembly of oriented zinc oxide nanowires. *Applied Physics Letters* 85: 3244-6

40. Onda T, Shibuichi S, Satoh N, Tsujii K. 1996. Super-water-repellent fractal surfaces. *Langmuir* 12: 2125-7

41. Patrick HN, Warr GG. 2000. Self-assembly structures of nonionic surfactants at graphite-solution inter-faces. 2. Effect of polydispersity and alkyl chain branching. *Colloids and Surfaces a-Physicochemical and Engineering Aspects* 162: 149-57

42. Patrick HN, Warr GG, Manne S, Aksay IA. 1997. Self-assembly structures of nonionic surfactants at graphite/solution interfaces. *Langmuir* 13: 4349-56

43. Quake SR, Scherer A. 2000. From micro- to nanofabrication with soft materials. *Science* 290: 1536-40

44. Ren ZF, Huang ZP, Xu JW, Wang JH, Bush P, et al. 1998. Synthesis of large arrays of well-aligned carbon nanotubes on glass. *Science* 282: 1105-7

45. Richard C, Balavoine F, Schultz P, Ebbesen TW, Mioskowski C. 2003. Supramolecular self-assembly of lipid derivatives on carbon nanotubes. *Science* 300: 775-8

46. Romero LA, Yost FG. 1996. Flow in an open channel capillary. *Journal of Fluid Mechanics* 322: 109-29

47. Rye RR, Mann JA, Yost FG. 1996. The flow of liquids in surface grooves. *Langmuir* 12: 555-65

48. Rye RR, Yost FG, Mann JA. 1996. Wetting kinetics in surface capillary grooves. *Langmuir* 12: 4625-7

49. Siddiqui FA, Franses EI. 1996. Equilibrium adsorption and tension of binary surfactant mixtures at the air/water interface. *Langmuir* 12: 354-62

50. Sing KSW. 2004. Characterization of porous materials: past, present and future. *Colloids and Surfaces a-Physicochemical and Engineering Aspects* 241: 3-7

51. Staples TL, Shaffer DG. 2002. Wicking flow in irregular capillaries. *Colloids and Surfaces a-Physicochemical and Engineering Aspects* 204: 239-50

52. Starov VM, Zhdanov SA, Velarde MG. 2004. Capillary imbibition of surfactant solutions in porous media and thin capillaries: partial wetting case. *Journal of Colloid and Interface Science* 273: 589-95

53. Stone HA, Stroock AD, Ajdari A. 2004. Engineering flows in small devices: Microfluidics toward a lab-on-a-chip. *Annual Review of Fluid Mechanics* 36: 381-411

54. Supple S, Quirke N. 2003. Rapid imbibition of fluids in carbon nanotubes. *Physical Review Letters* 90

55. Supple S, Quirke N. 2004. Molecular dynamics of transient oil flows in nanopores I: Imbibition speeds for single wall carbon nanotubes. In *The Journal of chemical physics*, pp. 8571-9

56. Tanner LH. 1979. Spreading of Silicone Oil Drops on Horizontal Surfaces. *Journal of Physics D-Applied Physics* 12: 1473-&

57. Thess A, Lee R, Nikolaev P, Dai HJ, Petit P, et al. 1996. Crystalline ropes of metallic carbon nanotubes. *Science* 273: 483-7

58. Tu Y, Huang ZP, Wang DZ, Wen JG, Ren ZF. 2002. Growth of aligned carbon nanotubes with controlled site density. *Applied Physics Letters* 80: 4018-20

59. Vautier-Giongo C, Bales BL. 2003. Estimate of the ionization degree of ionic micelles based on Krafft temperature measurements. *Journal of Physical Chemistry B* 107: 5398-403

60. Vizika O, Payatakes AC. 1989. Parametric Experimental-Study of Forced Imbibition in Porous-Media. *Physicochemical Hydrodynamics* 11: 187-204

61. Walther JH, Werder T, Jaffe RL, Koumoutsakos P. 2004. Hydrodynamic properties of carbon nanotubes. *Physical Review E* 69

62. Ward CA, Stanga D. 2001. Interfacial conditions during evaporation or condensation of water. *Physical Review E* 6405

63. Warren PB. 2004. Late stage kinetics for various wicking and spreading problems. *Physical Review E* 69

64. Washburn EW. 1921. The Dynamics of Capillary Flow. *The Physical Review* XVII: 273-83

65. Wenzel RN. 1949. Surface Roughness and Contact Angle. *Journal of Physical and Colloid Chemistry* 53: 1466-7

66. Yang W, Wang W, Suo Z. 1994. Cavity and Dislocation Instability Due to Electric-Current. *Journal of the Mechanics and Physics of Solids* 42: 897-911

67. Yu MF. 2004. Fundamental mechanical properties of carbon nanotubes: Current understanding and the related experimental studies. *Journal of Engineering Materials and Technology-Transactions of the Asme* 126: 271-8

68. Yu MF, Kowalewski T, Ruoff RS. 2001. Structural analysis of collapsed, and twisted and collapsed, multiwalled carbon nanotubes by atomic force microscopy. *Physical Review Letters* 86: 87-90

69. Zhang WD, Wen Y, Li J, Xu GQ, Gan LM. 2002. Synthesis of vertically aligned carbon nanotubes films on silicon wafers by pyrolysis of ethylenediamine. *Thin Solid Films* 422: 120-5

70. Zhu YX, Granick S. 2001. Rate-dependent slip of Newtonian liquid at smooth surfaces. *Physical Review Letters* 8709: art. no.-096105

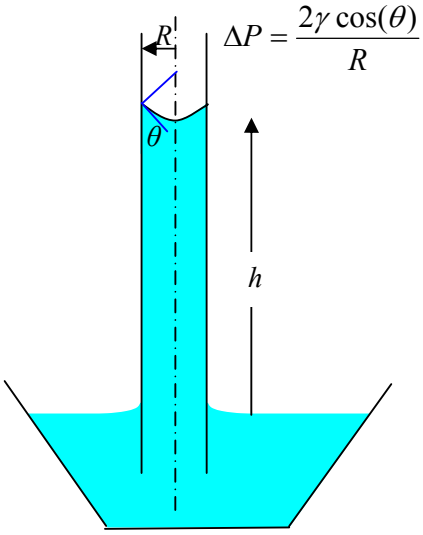

Figure 1.1 Capillary rise

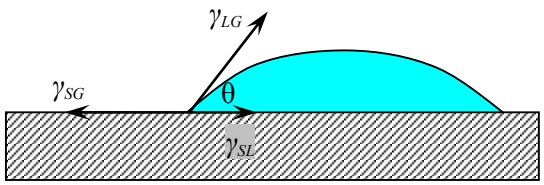

Figure 1.2 Contact angle

1. Spin coat photoresist on wafer	
2. Pattern the photoresist with desired mask	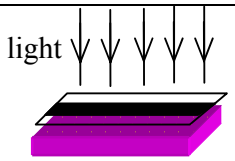
3. Develop the resist and expose part of the wafer	
4. Sputter iron catalyst on top	
5. Remove the catalyst on remaining photoresist by lift-off	
6. Heat catalyst into sinters	
7. Grow carbon nanotube arrays from the catalyst layer	

Figure 2.1 A diagram of nanowick fabrication

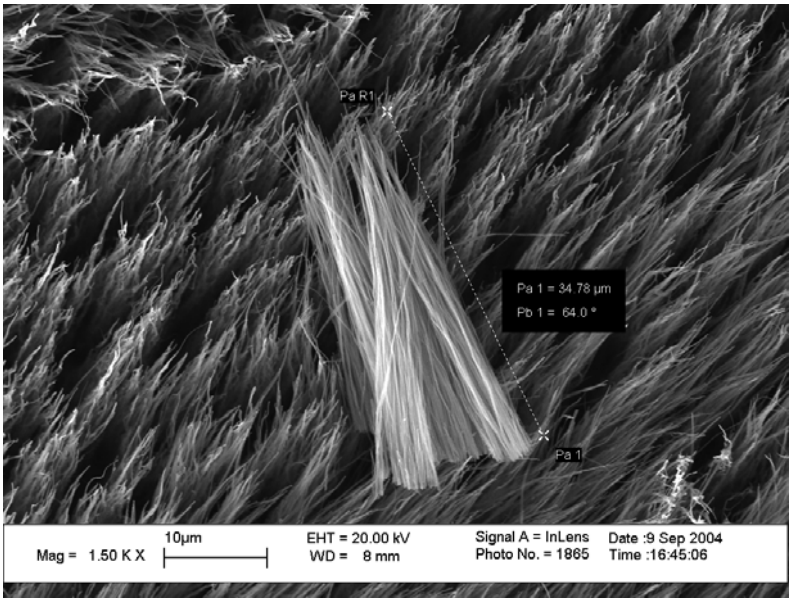

A: a bundle of nanotubes on top of a 33µm high mat

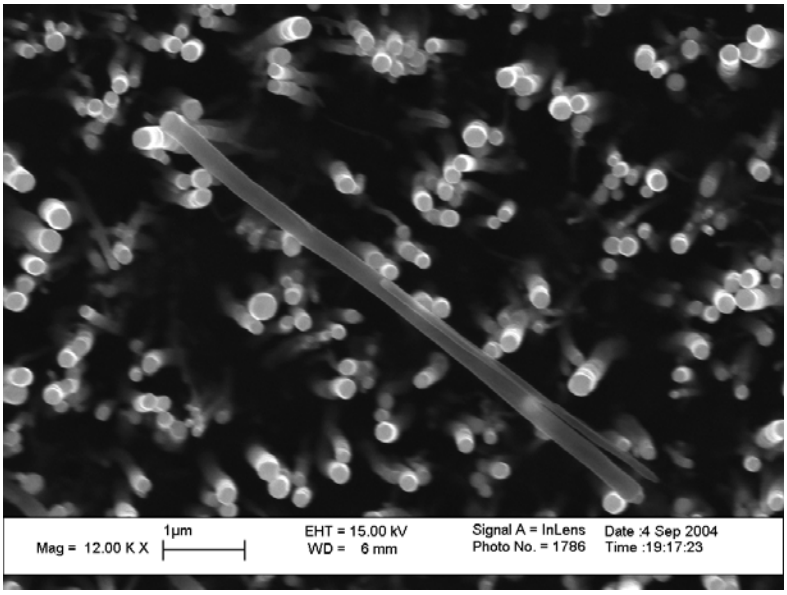

B: two nanotubes on top of a 7µm high mat

Figure 2.2 Top view of carbon nanotube mats purchased from NanoLab, Inc.

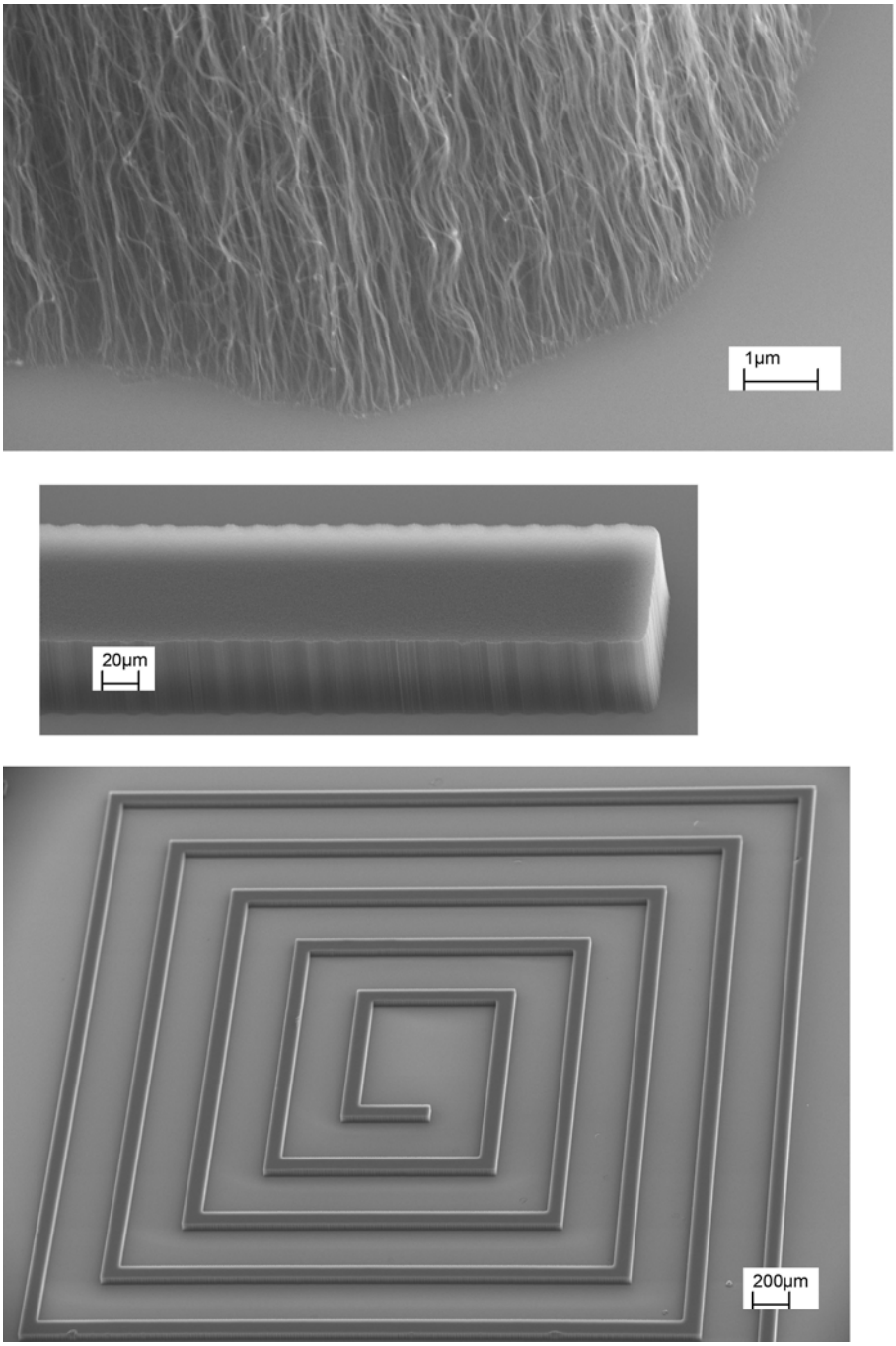

Figure 2.3 Hierarchical structure of nanowicks

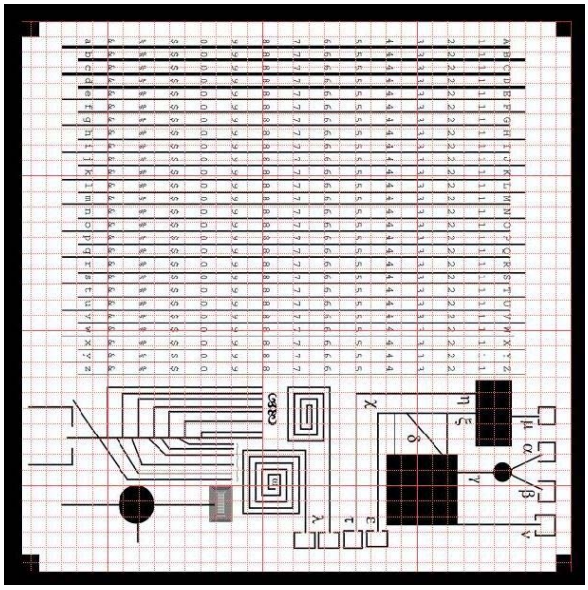

A: design patterns for nanowicks

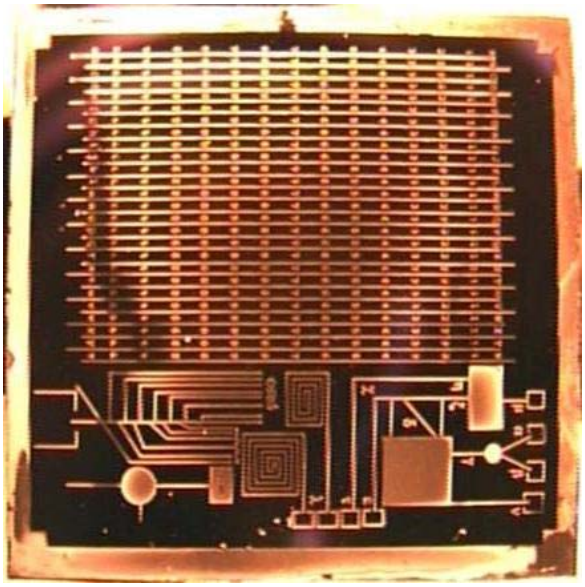

B: actual look of the wafer

Figure 2.4 Nanowick circuits on centimetre-sized wafer

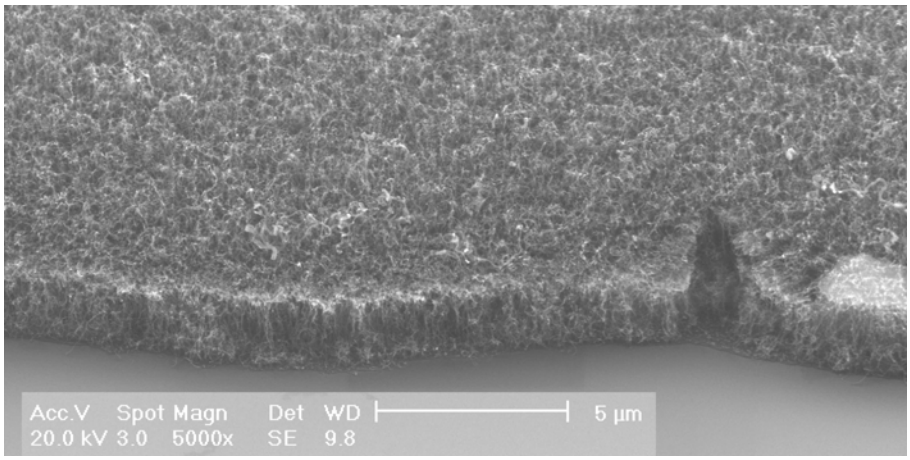

A: a 3µm-high dense carbon nanotube mat

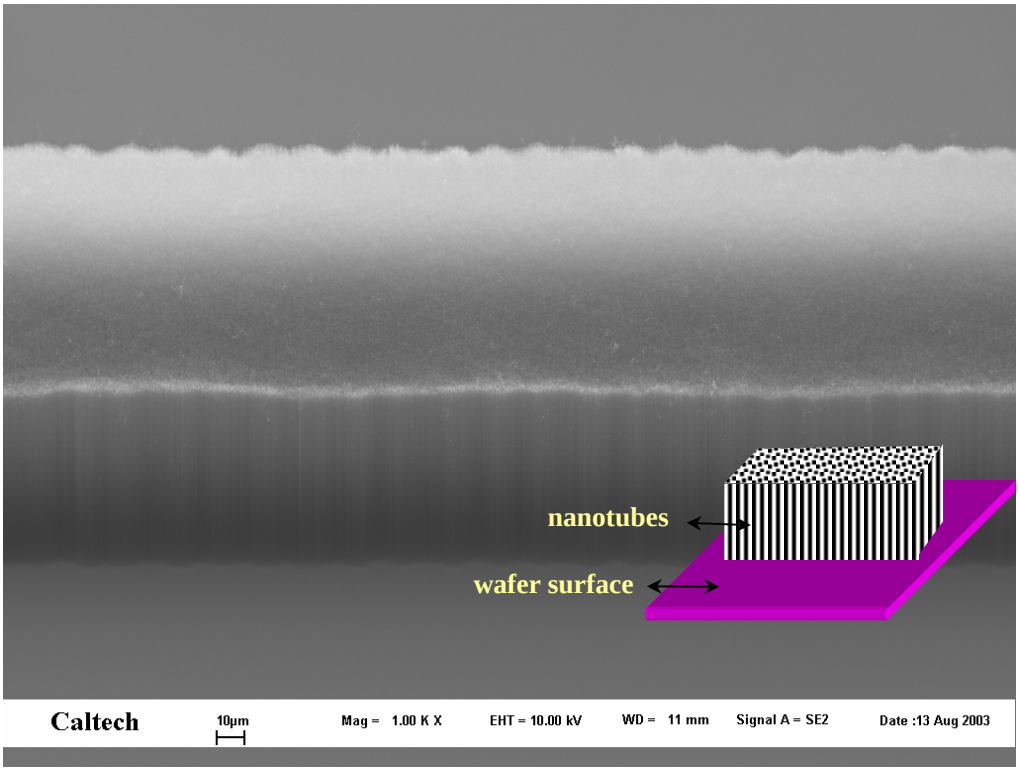

B: a 60µm-high 100µm-wide nanowick; inset: diagram of the structure

Figure 2.5 Local 45º tilted view of nanowicks

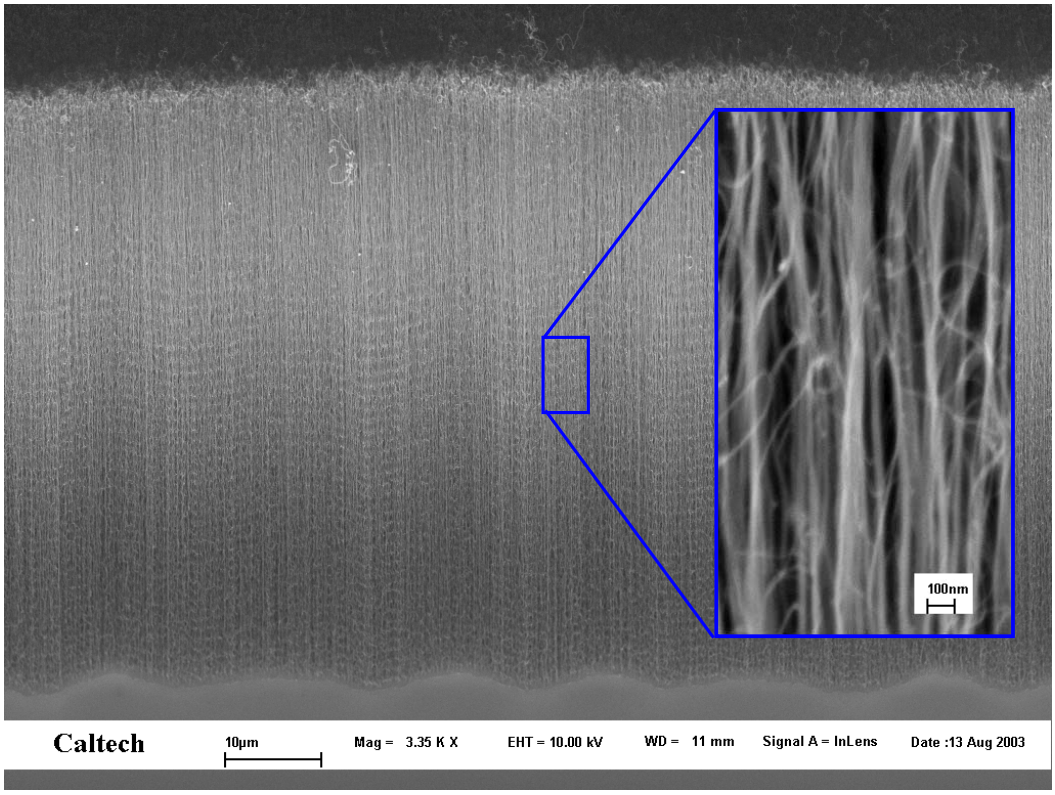

A: the nanowick sidewall; inset: close-up view

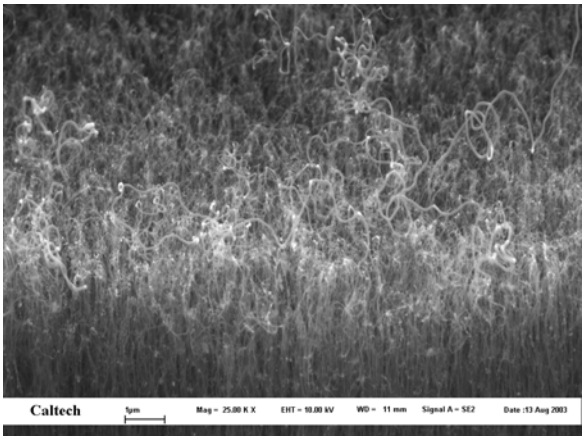

B: the nanowick top

Figure 2.6 Sidewall and top surface of the nanowick in Fig.2.4B

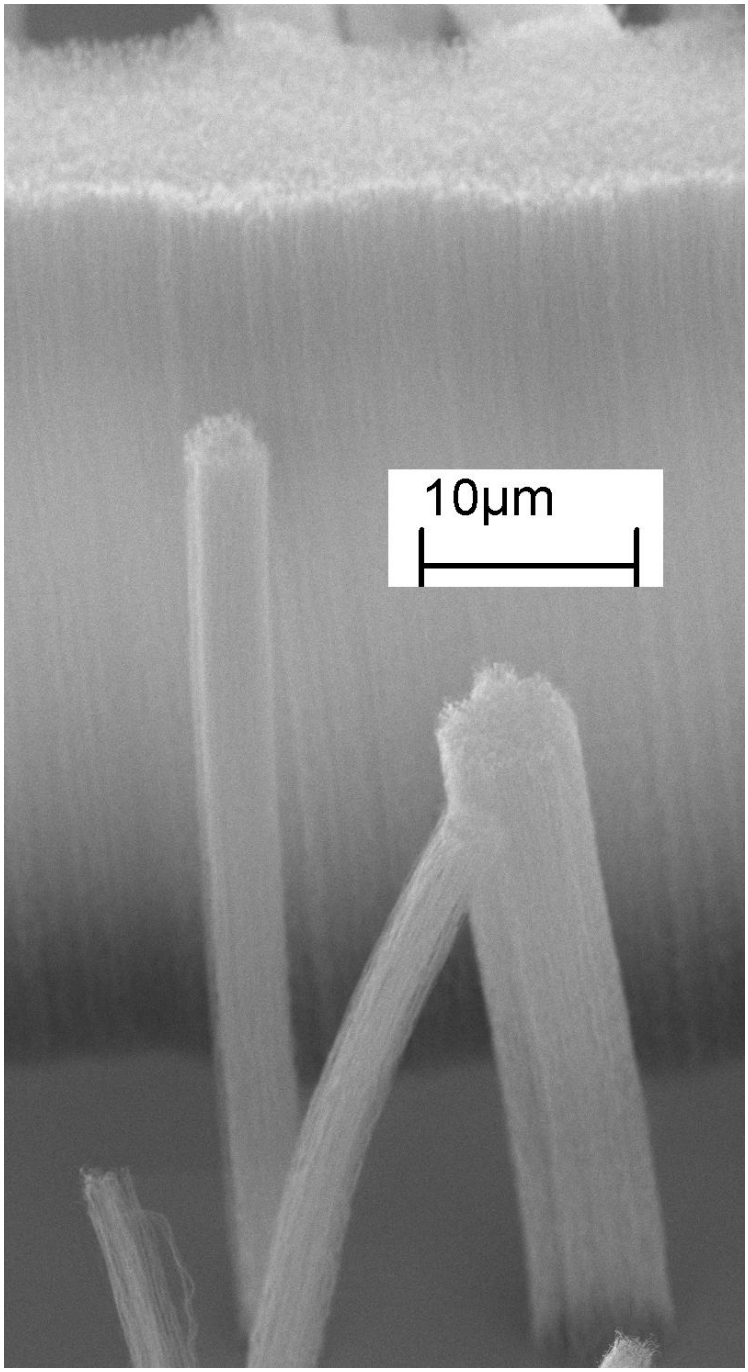

Figure 2.7 Minute nanowicks

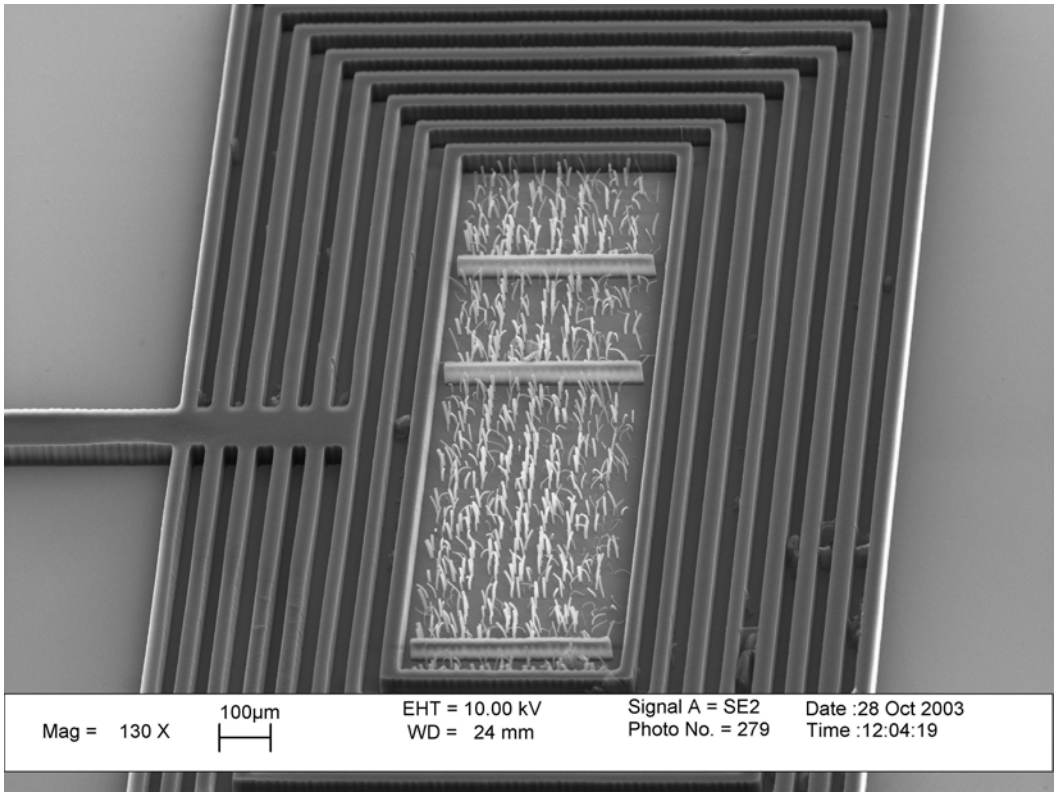

Figure 2.8 Built-in liquid holder at nanowick inlet

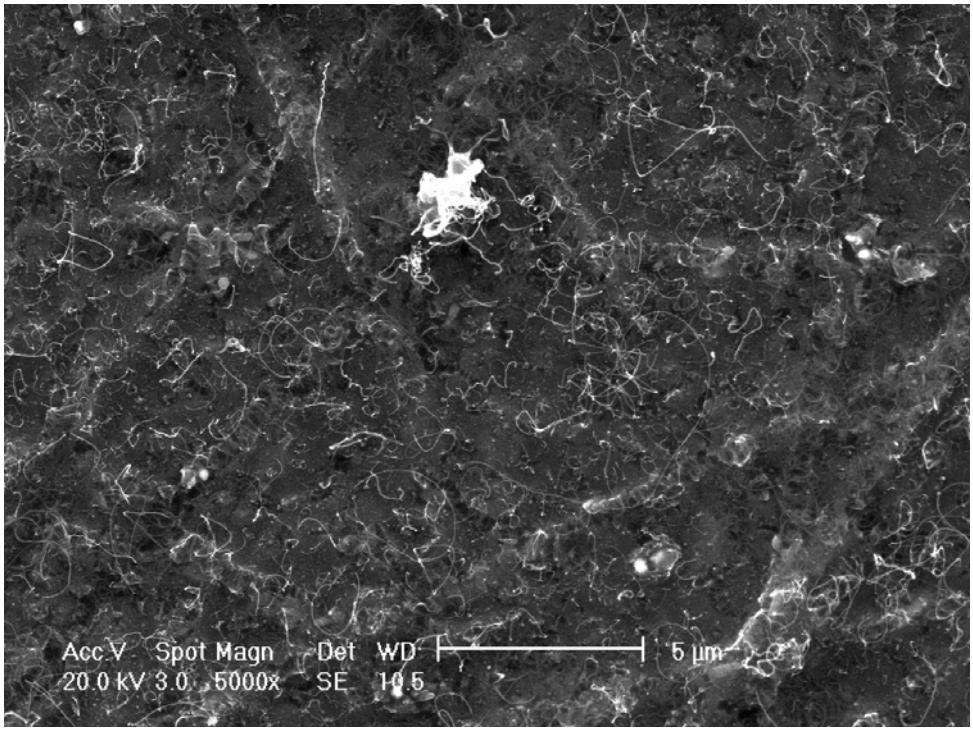

A: local view

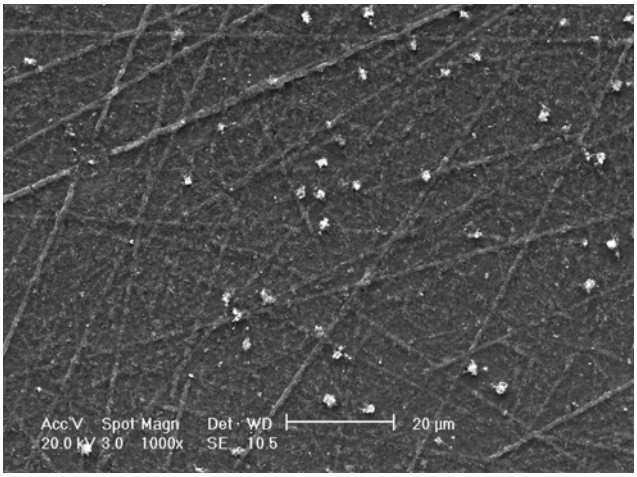

B: overall view

Figure 2.9 Hierarchical rough surface fabricated with nanotube mat

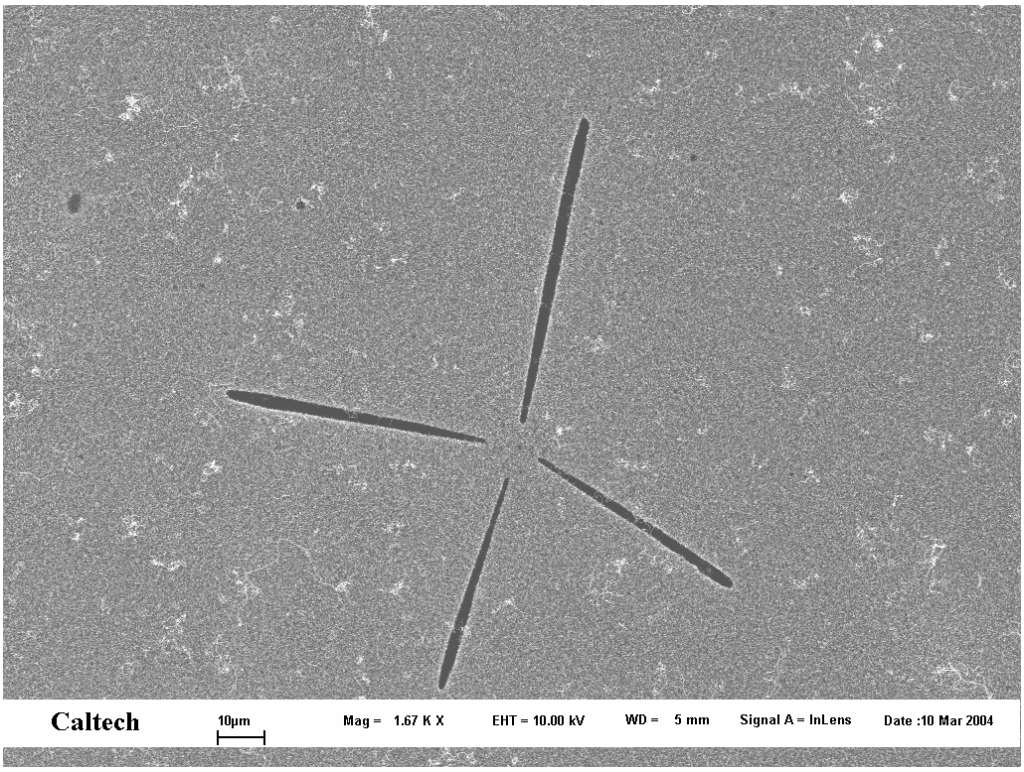

Figure 2.10 Micro-canyons induced by thermal fractures within the catalyst layer

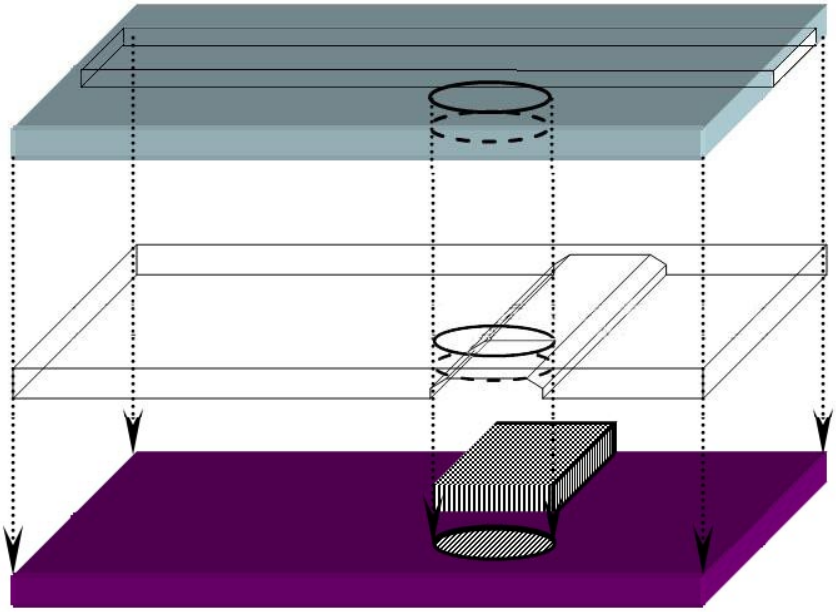

A: alignment of two layers of PDMS channels with a compatible nanowick

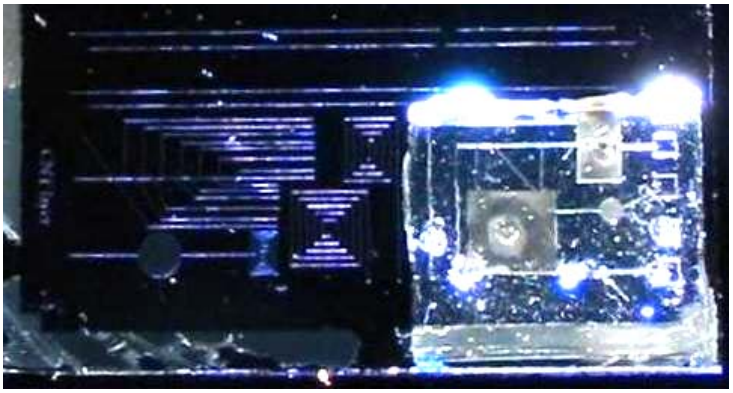

B: an example of encapsulation

Figure 2.11 Encapsulating nanowicks into channels

(i) Corner flow (ii) Top surface flow (iii) Interstitial flow

Figure 3.1 Formats of liquid transport with nanowicks

A: nanotube long axis B: nanowick long axis

Figure 3.2 Reference frame: nanotube long axis and nanowick long axis

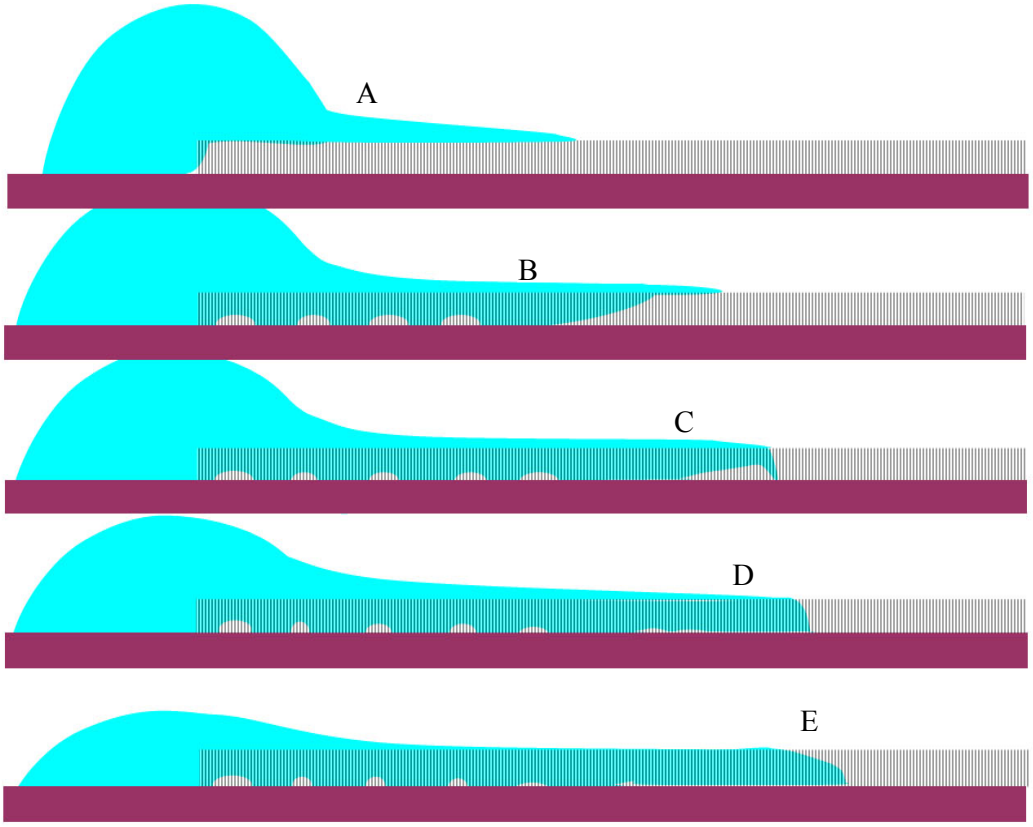

Figure 3.3 Typical progression of flow in nanowicks

A: superficial spreading on the surface asperities;

B: vertical seeping from top surface into the nanofiber interstices;

C: diving-in of the surface flow at the advancing front as the surface flow slows down;

D: co-advancing of surface flow and interstitial flow;

E: advancing interstitial flow supplied by surface flow

SL: supply liquid; WS: wafer surface; NW: nanowick; PL: position reference label.

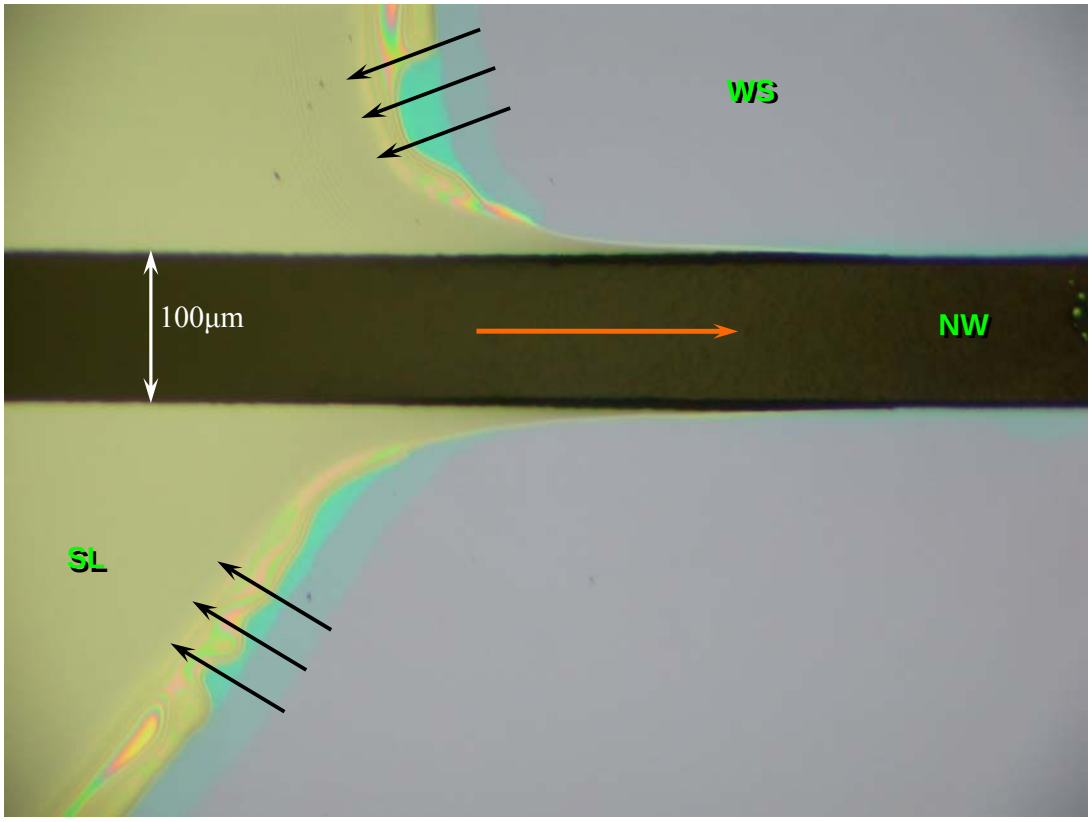

Figure 3.4 Wicking inlet in situ

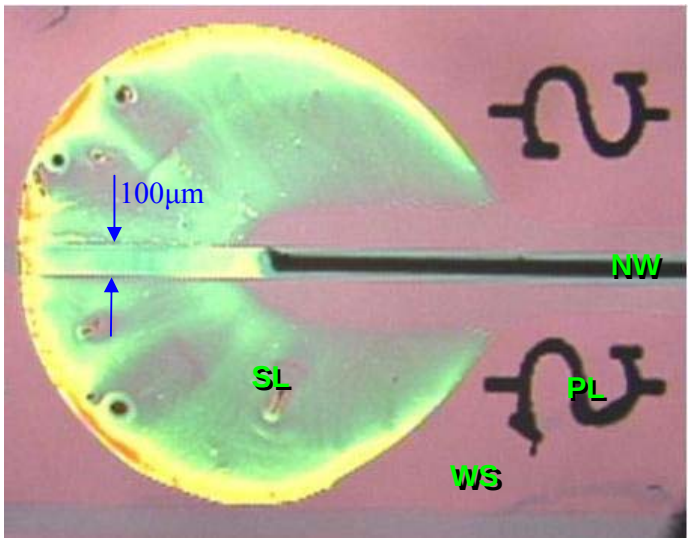

A: droplet residue

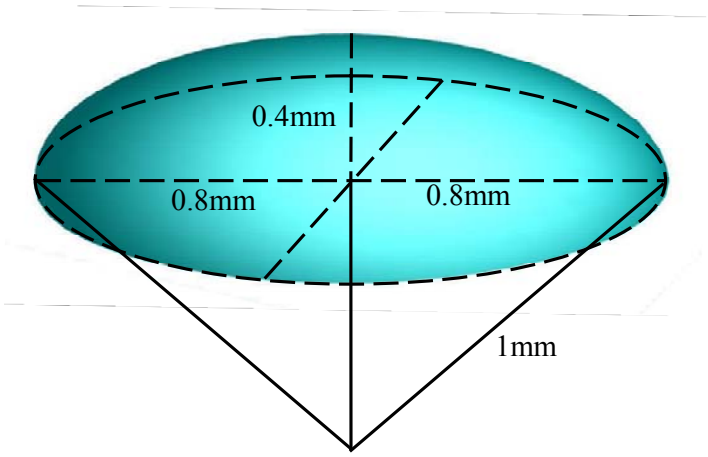

B: typical geometry

Figure 3.5 Input droplet

SL: supply liquid; AP: auxiliary pad; NW: nanowick; CA: corner accumulation.

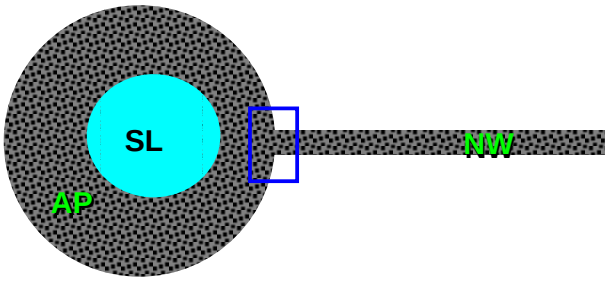

A: diagram

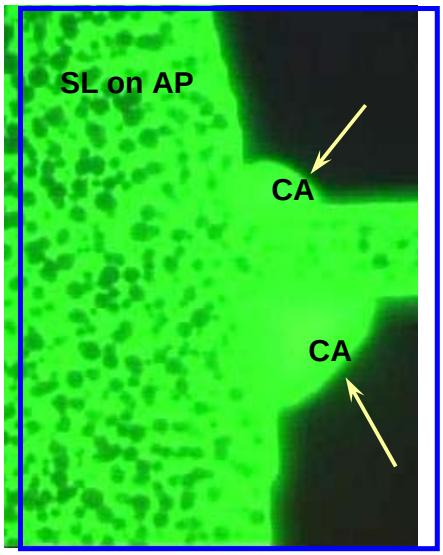

B: bottom view at the inlet junction

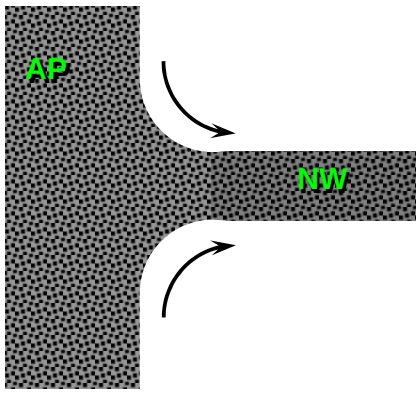

C: rounding of the concave corner

Figure 3.6 Supplying liquid from an inlet auxiliary pad

WS: wafer surface; NW: nanowick; SF: surface flow; CF: corner flow.

A: a 3μm-high 100μm-wide nanowick

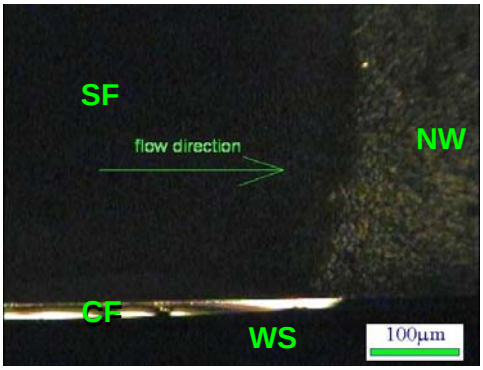

B: a 40μm-high 1.8mm-wide nanowick

Figure 3.7 Top view of surface flow and corner flow on low aspect ratio nanowicks

SL: supply liquid; NW: nanowick; PL: position reference label;
BSF: bulky surface flow; TSF: thin film surface flow.

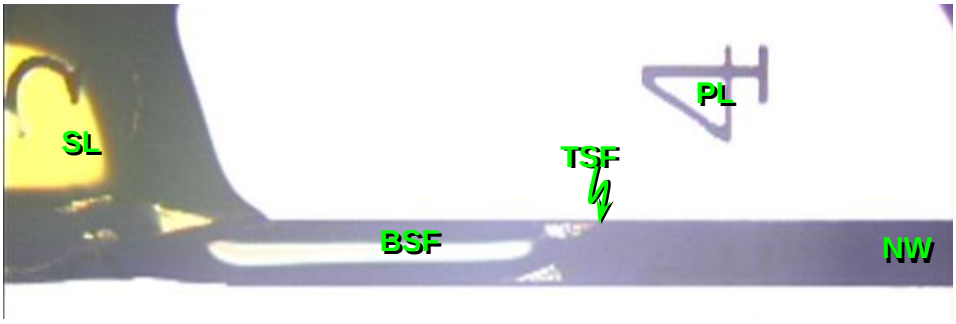

A: surface flow

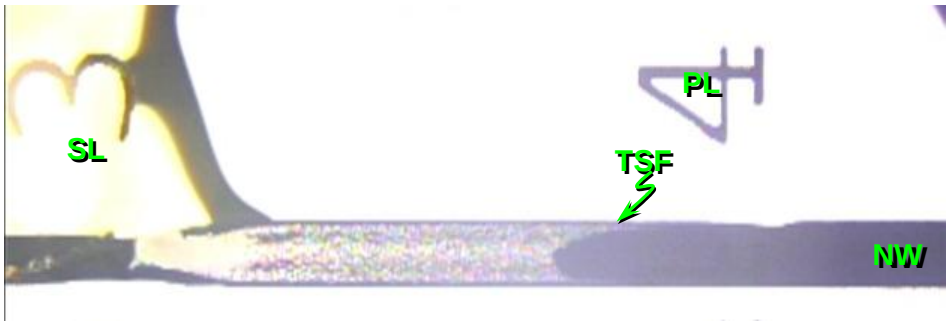

B: late-stage surface flow

Figure 3.8 Top view of surface flow from a concave droplet on a 200μm nanowick

SL: supply liquid; NW: nanowick; SF: surface flow; PL: position reference label.

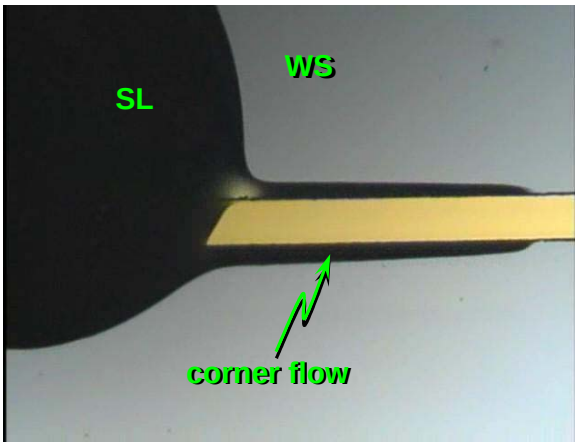

A: corner flow beside a solid step

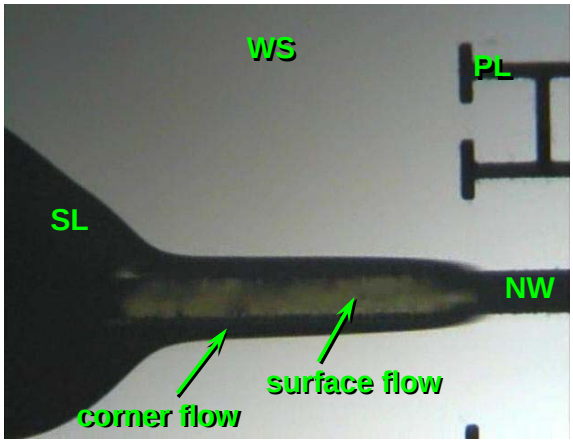

B: corner flow and surface flow beside a 40µm-high 100µm-wide nanowick

Figure 3.9 Control experiment for corner flow (top view)

SL: supply liquid; CS: control strip; WS: wafer surface;
SF: surface flow; PF: progressive front.

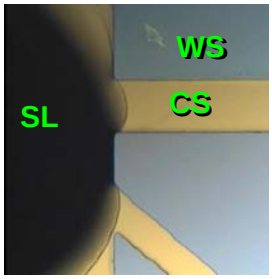

A: spreading on smooth strip

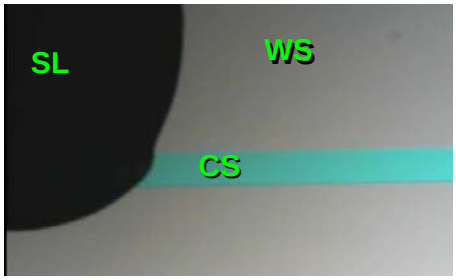

B: spreading on nanotube catalyst

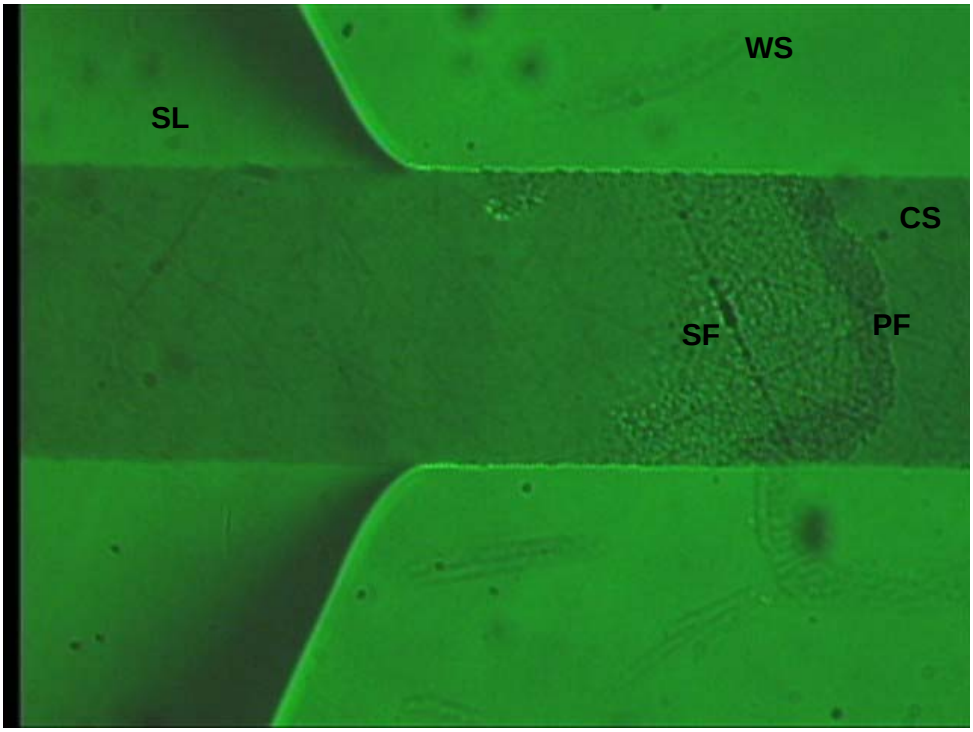

C: spreading on nanotube rough surface

Figure 3.10 Control experiments for surface flow

CF: corner flow; SF: surface flow; WS: wafer surface;
NW: nanowick; TB: trapped bubble.

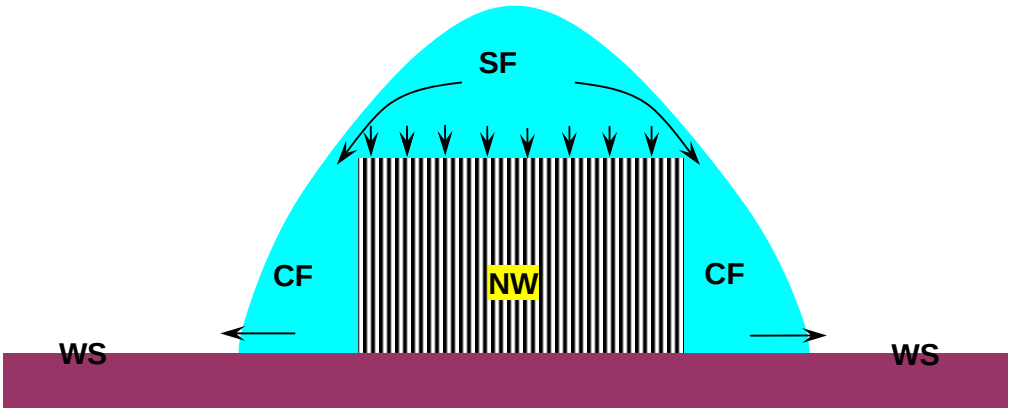

A: initial flow in the presence of corner flow

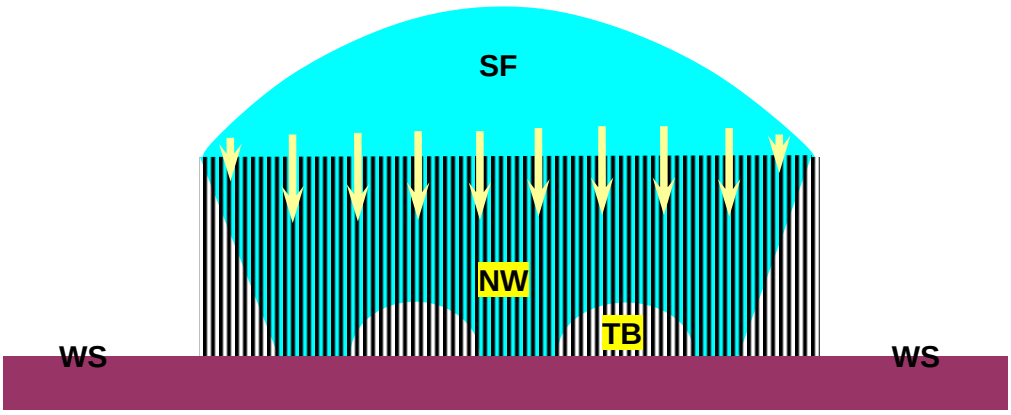

B: vertical seeping

Figure 3.11 Schematic diagrams of cross-sectional flow for high nanowicks

TB: trapped bubble; WS: wafer surface; NW: nanowick.

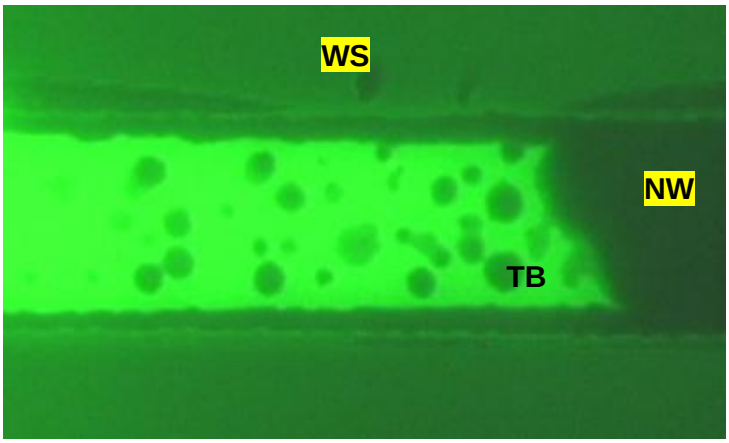

A: trapped bubble in vertical seeping

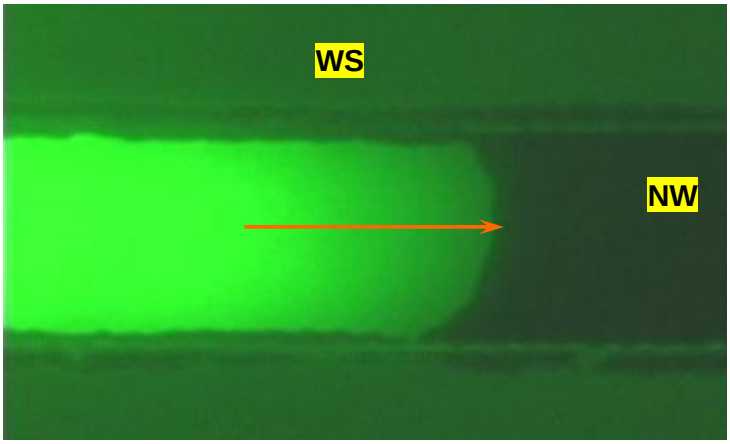

B: smooth lateral interstitial wicking

Figure 3.12 Vertical and lateral interstitial flow

WS: wafer surface; NW: nanowick.

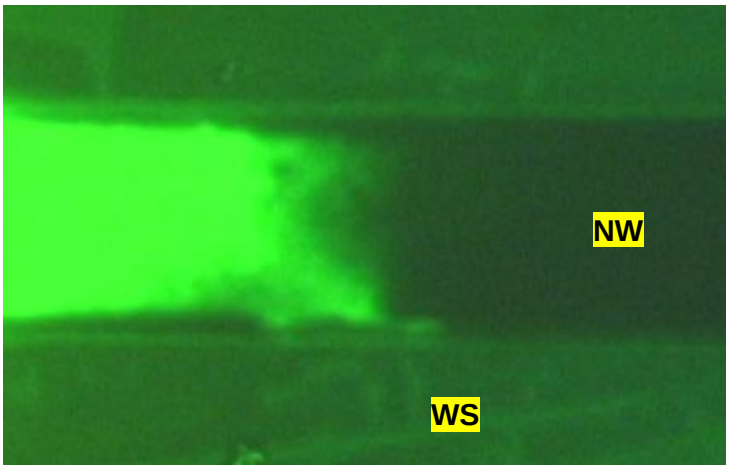

A: transition as surface flow gradually slows down

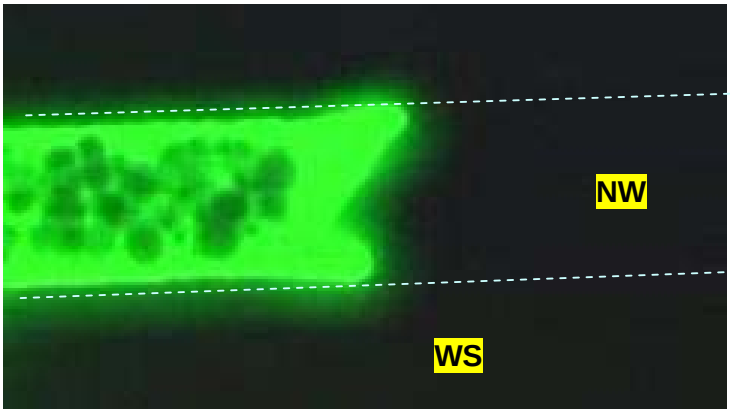

B: diving-in at the front as surface flow brakes to a stop.
(This image is not in good focus, consequently edges are fuzzy.)

Figure 3.13 Two types of transition from vertical seeping to lateral wicking

A: bottom view

B: top view of another branching by courtesy of Sansom

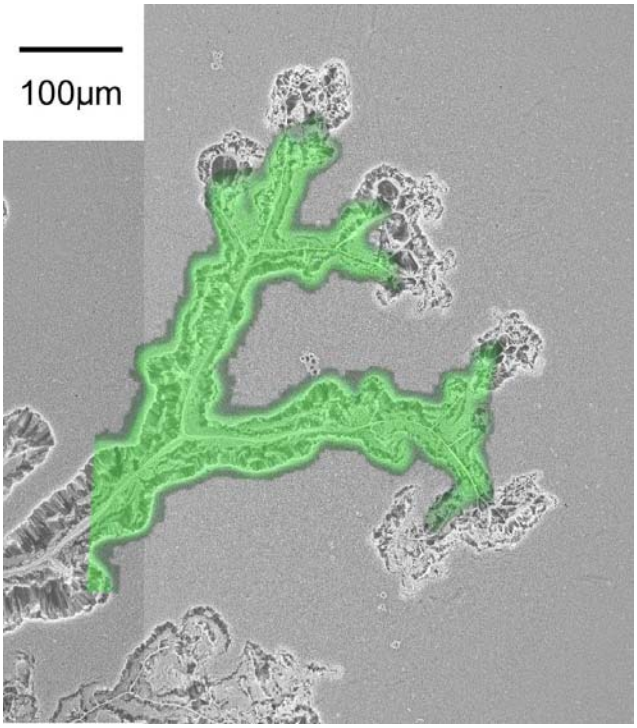

C: SEM view with superposition of the bottom view

Figure 3.14 Fractal fronts wicking through nanotube interstices

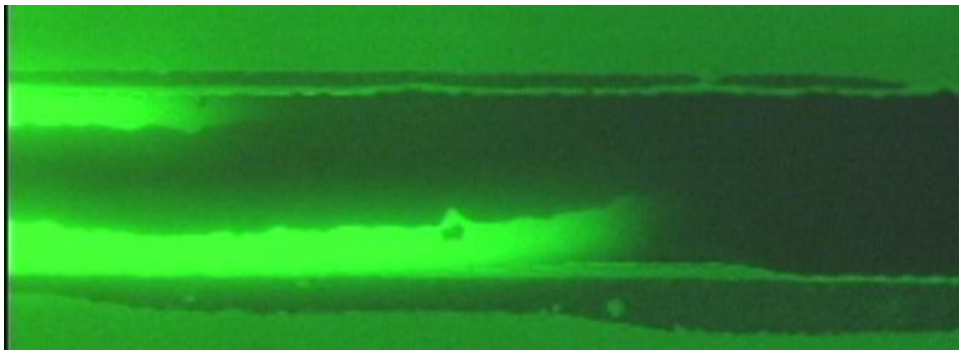

A: bottom view

B: top view

Figure 3.15 Interstitial edge flow

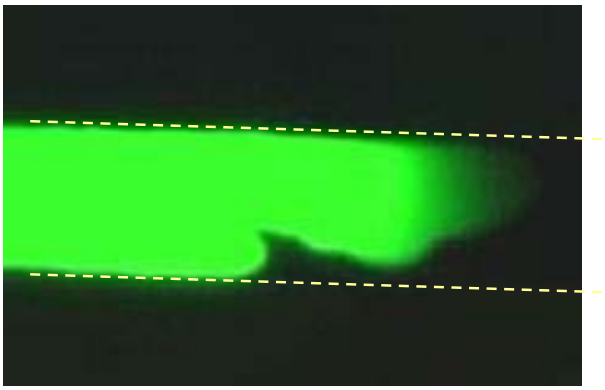

A: in 100µm wide nanowick (bottom view)

B: top view on uniform nanocarpet

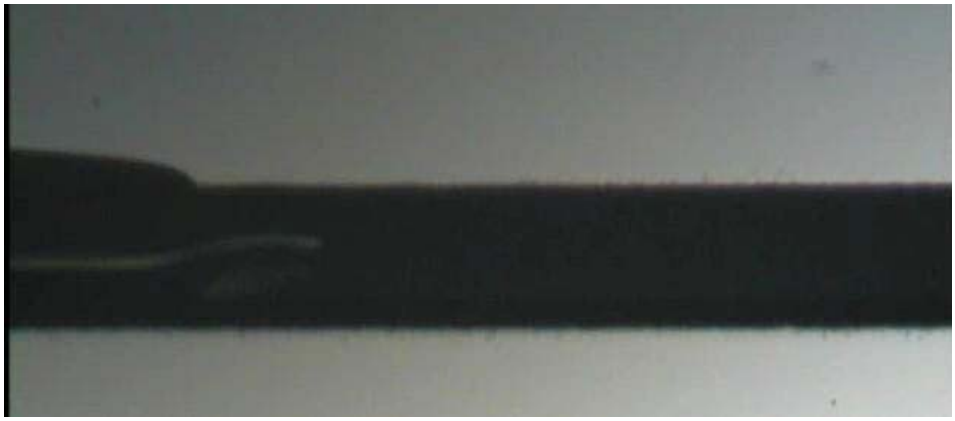

C: top view on 200µm wide nanowick

Figure 3.16 Fingers invading nanowicks

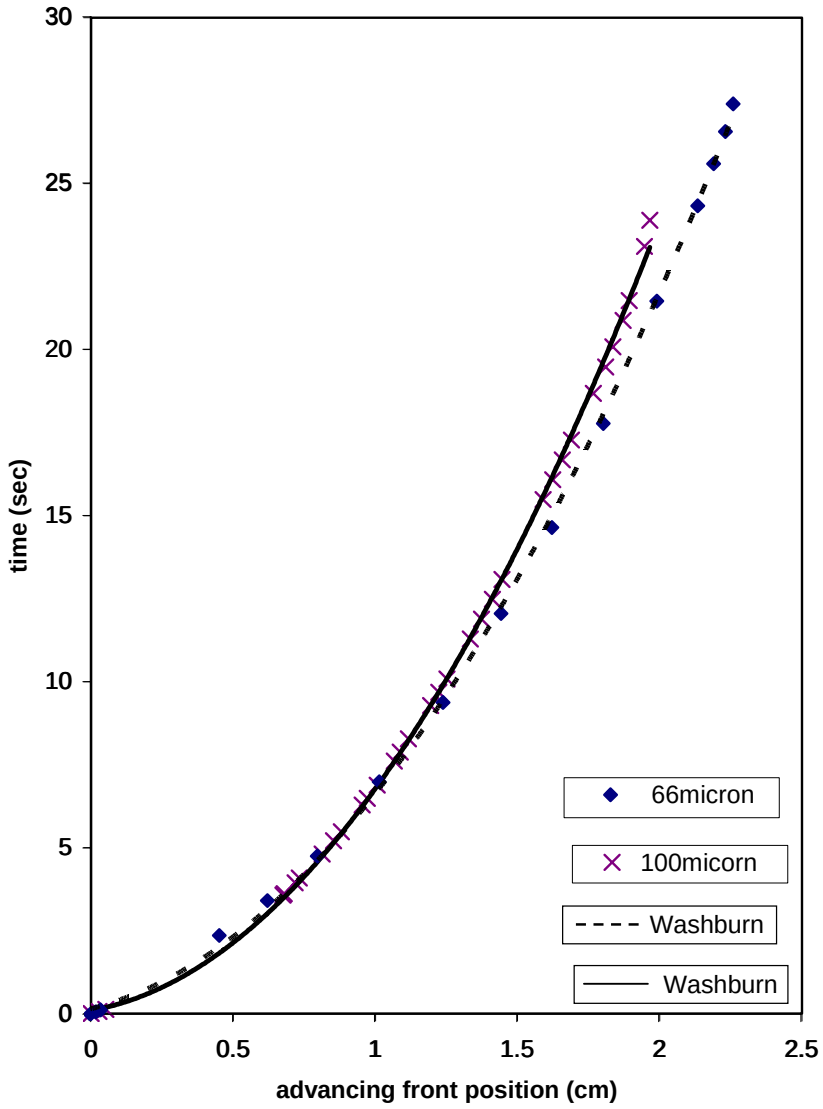

Figure 4.1 Washburn spreading in the presence of corner flow on nanowicks

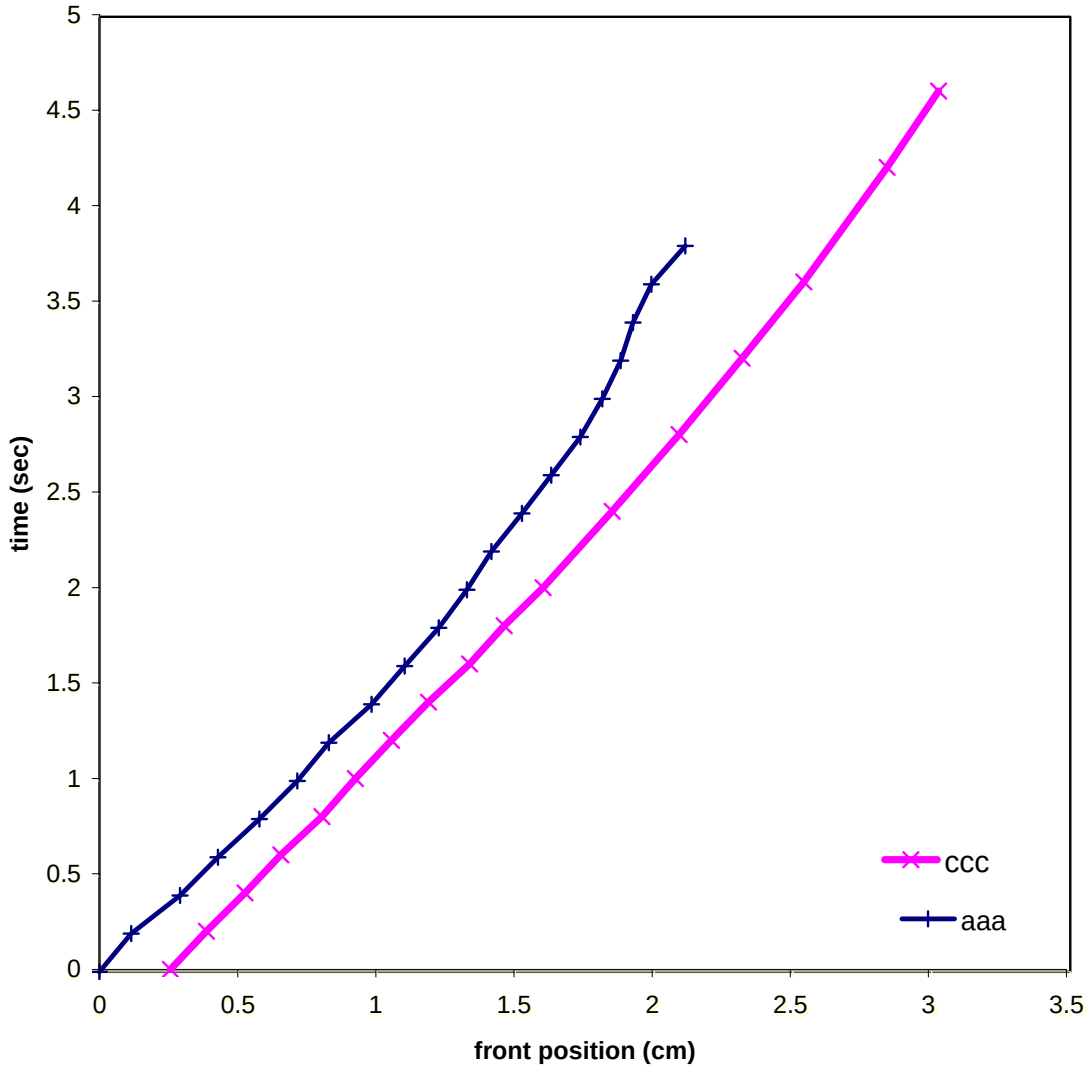

Figure 4.2 Liquid moving front position as a function of time for surface flow through the top asperities on 1.5mm wide nanowicks

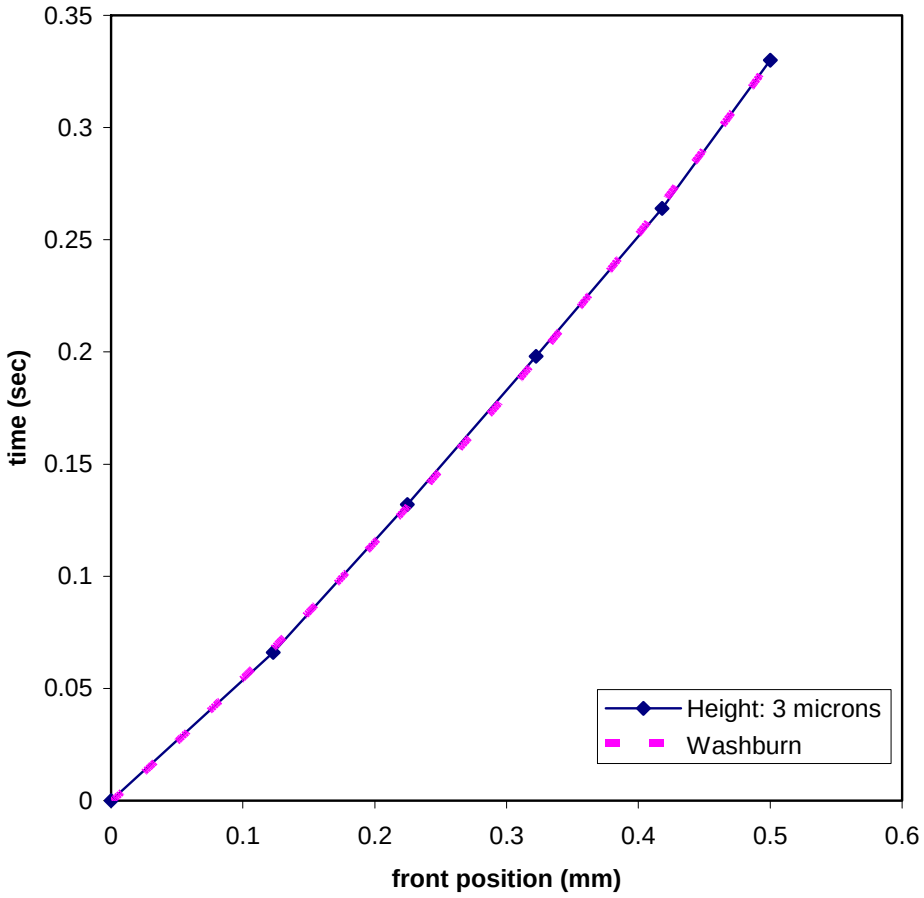

Figure 4.3 Surface flow on a 3µm-high and 100µm-wide nanowick

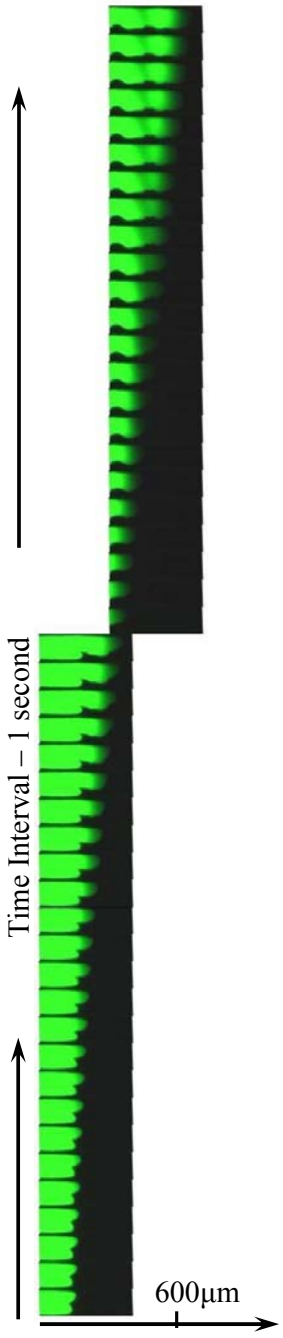

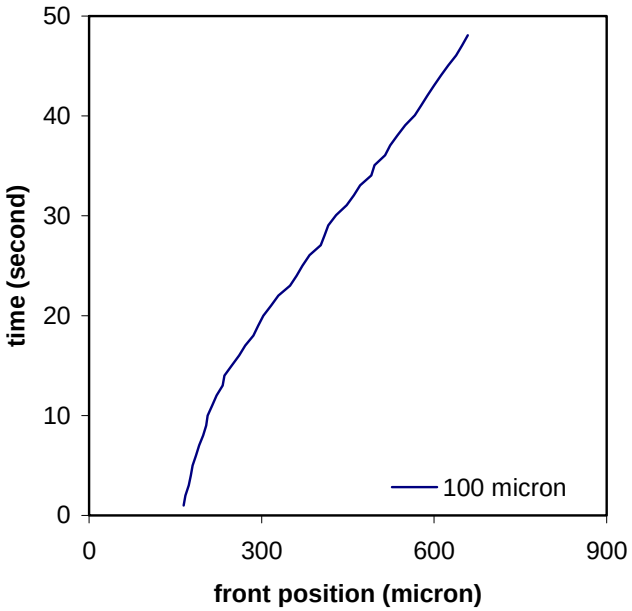

A: front displacement on a 100µm nanowick (extracted from left frames)

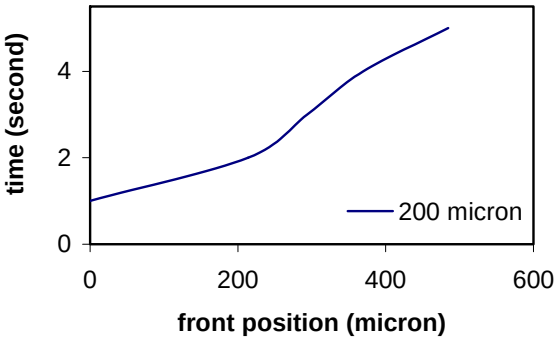

B: front displacement on a 200µm nanowick

Figure 4.4 Speed of fingering for smooth lateral interstitial wicking

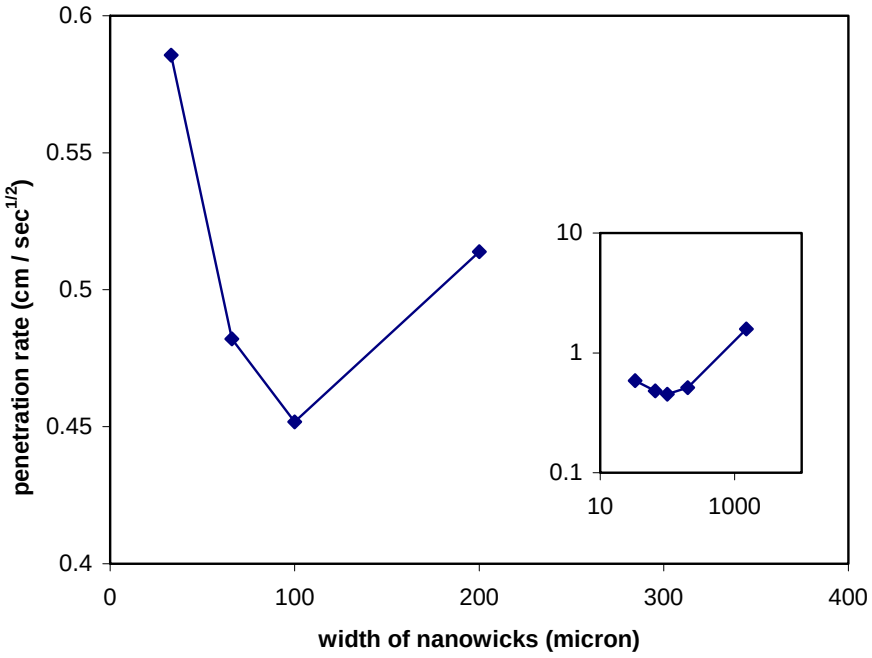

Figure 4.5 Penetration rate of 60μm high nanowicks as a function of nanowick width

Inset: data in logarithmic coordinates with one more point at 1500μm.

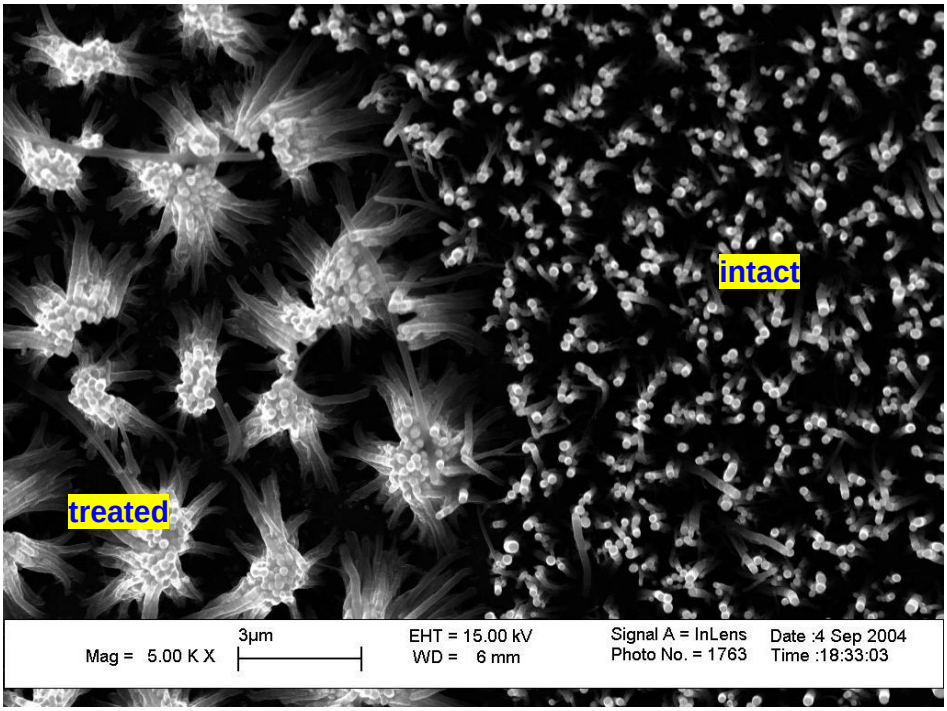

A: SEM view of front imprint in 7µm-high 100nm-thick nanotube arrays

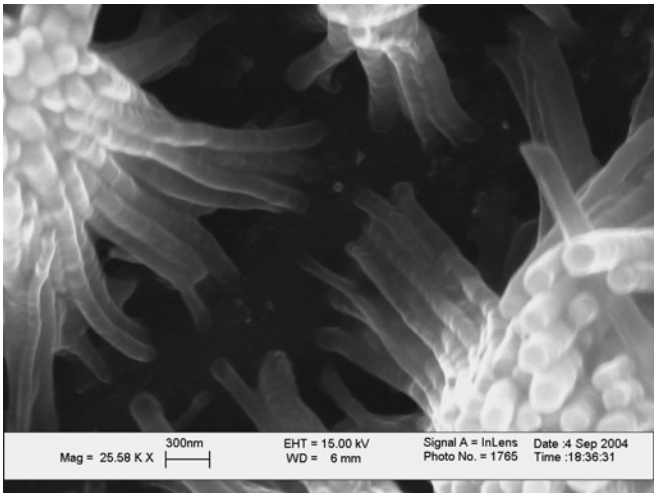

B: close-up at the open space

Figure 4.6 Configuration comparison of intact nanotube arrays and liquid-treated arrays

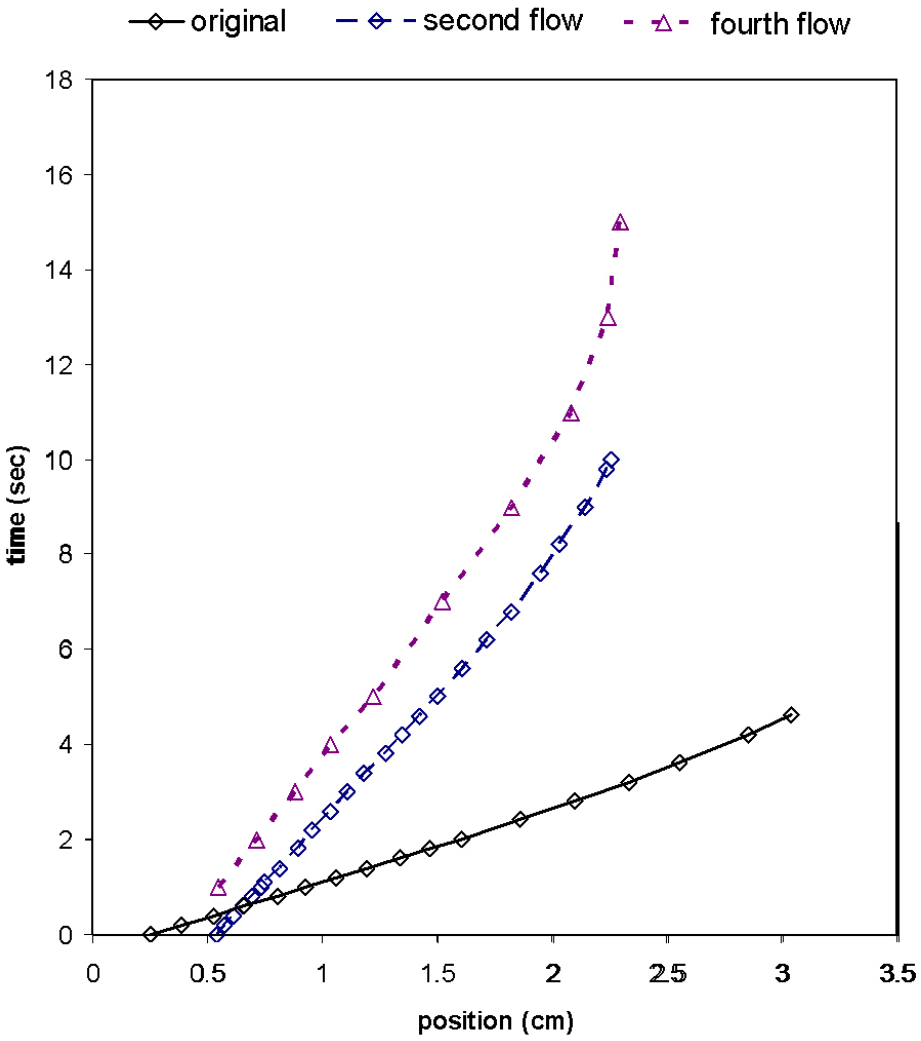

Figure 4.7 Reflow tests on a 1.5mm wide nanowick

Speed: original flow: 0.674cm/s; second flow: 0.191cm/s; fourth flow: 0.163cm/s

(Speed are derived through linear fitting of the first half points)

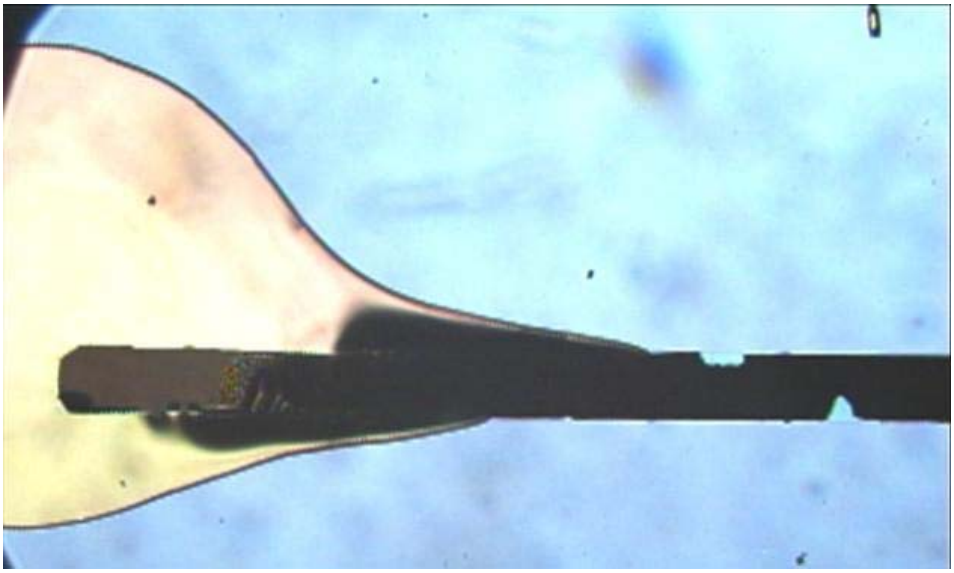

A: initial flow at in let

B: late-stage front of A

C: Another late-stage front in the absence of corner flow;

D: bottom view of a front
(dyed with Nile Red)

Figure 4.8 Observations of PDMS flow on nanowicks

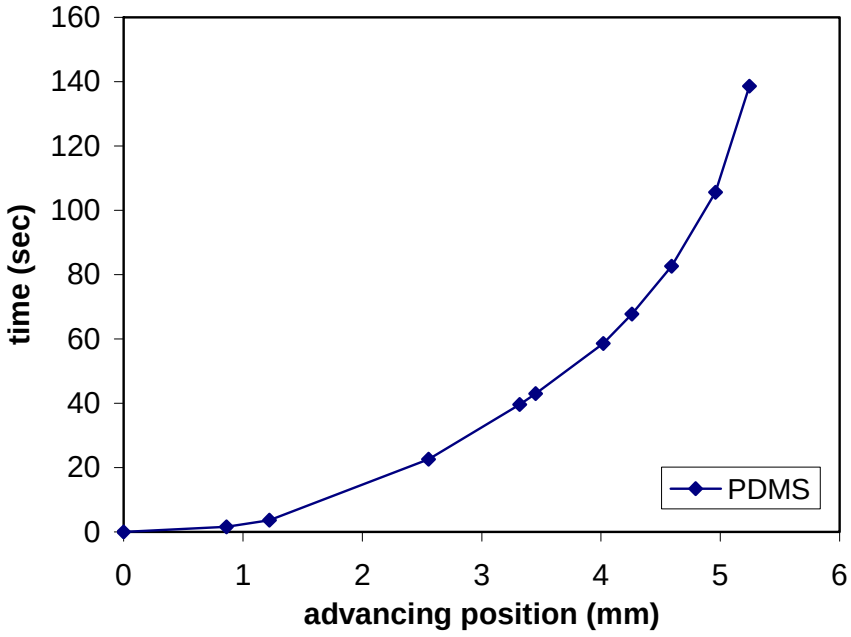

Figure 4.9 PDMS spreading on a 200µm wide and 40µm high nanowick

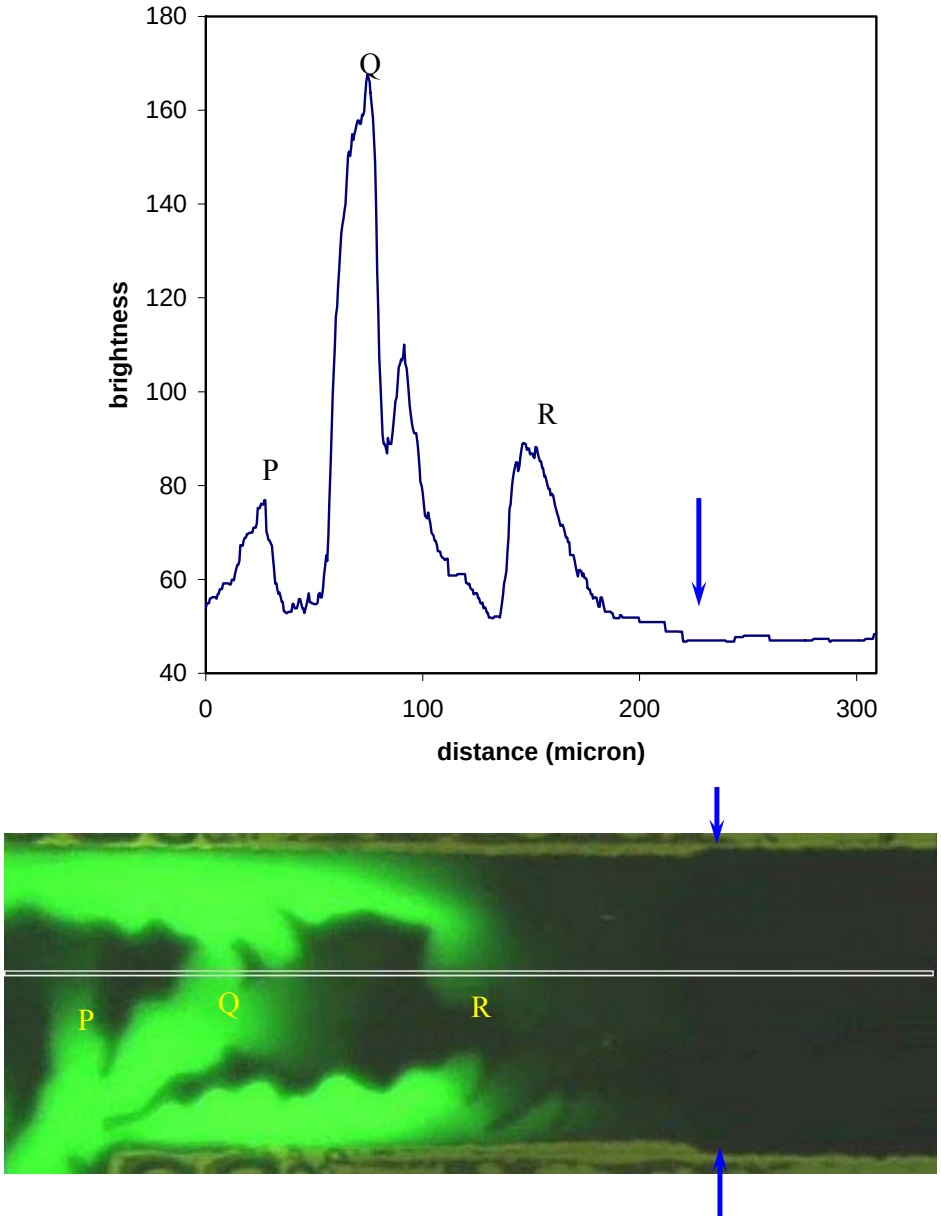

Figure 5.1 Light intensity changes at front edges

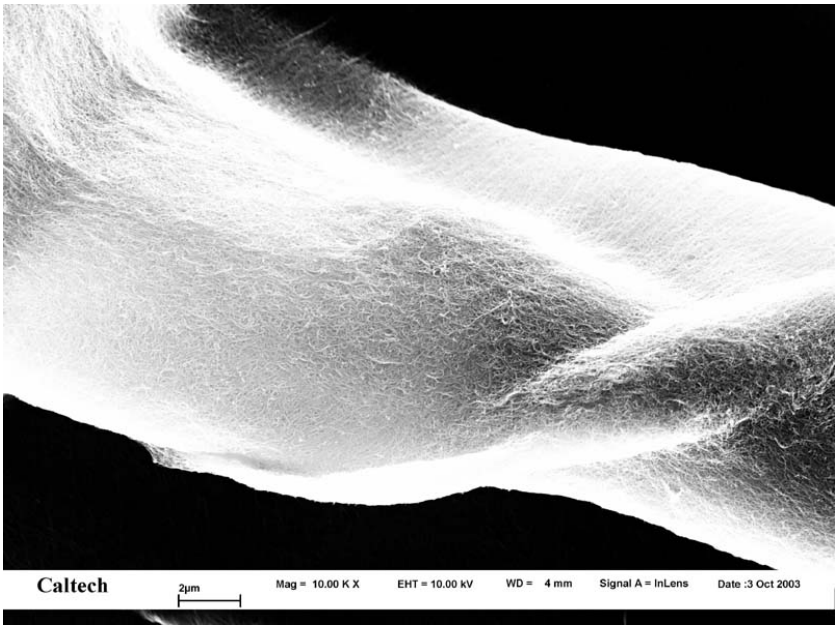

A: convection weaves nanotubes into a smooth ridge

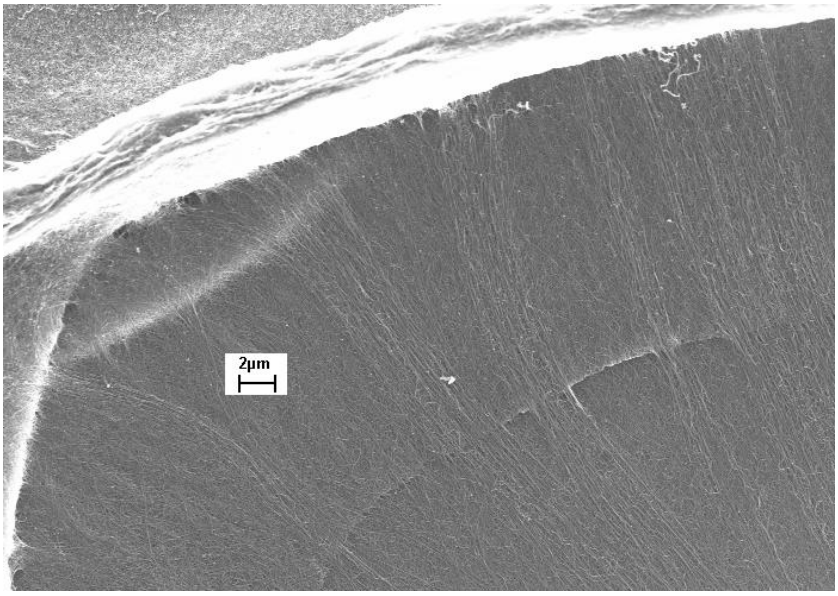

B: lateral capillary force pulls nanotubes together, but they are not woven as in A

Figure 5.2 The ridge at nanotube self-assembly patterns with and without convection

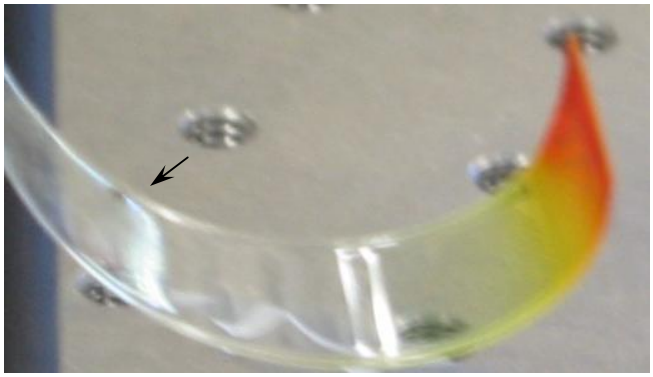

A: fluorescein solution imbibition in polyacrylamide

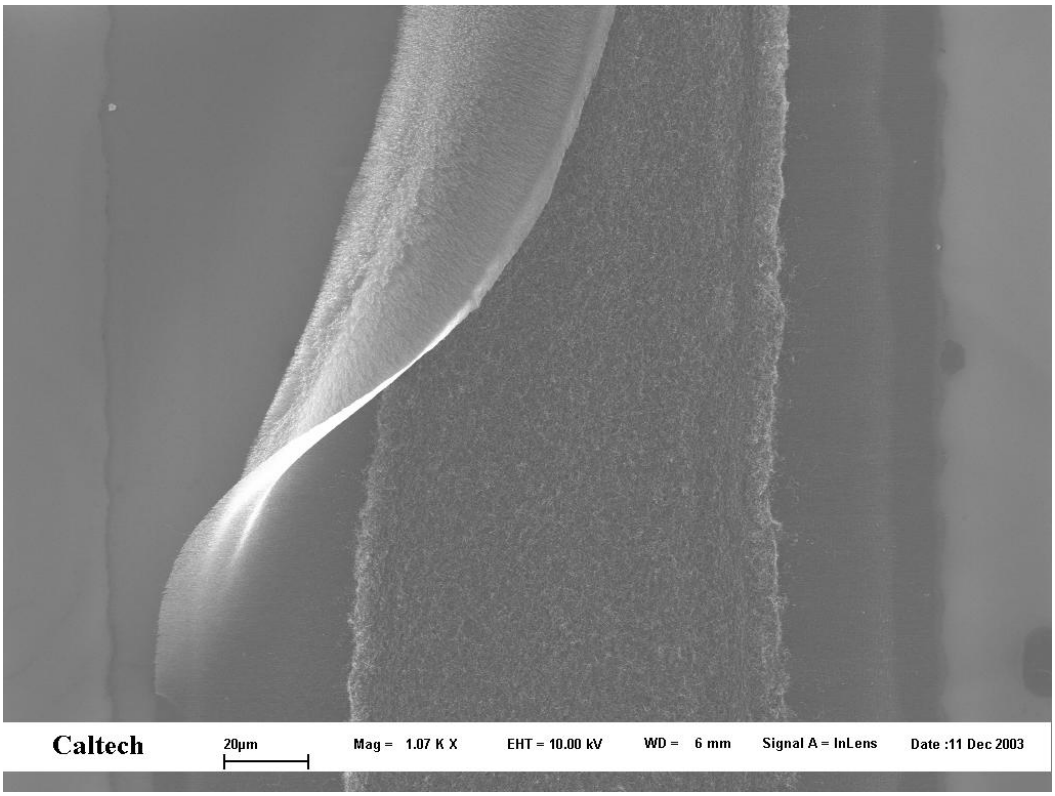

B: 200µm wide nanowick

Figure 5.3 Curling by surface tension

A.

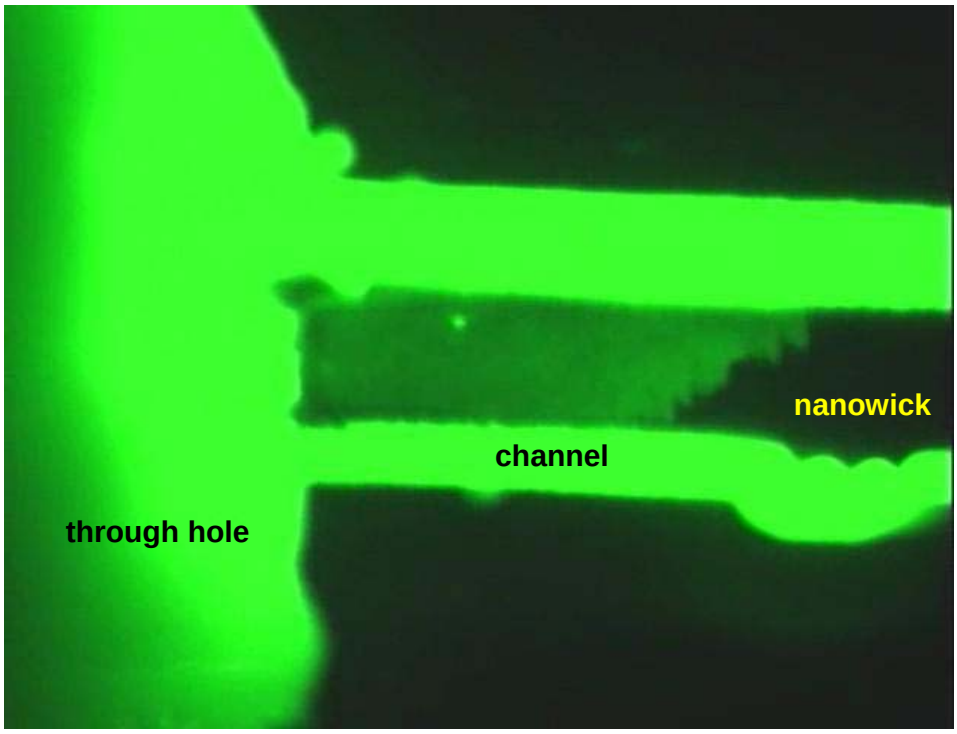

B.

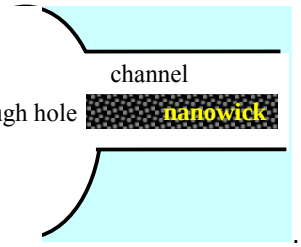

Figure 5.4 Interstitial flow of an encapsulated nanowick

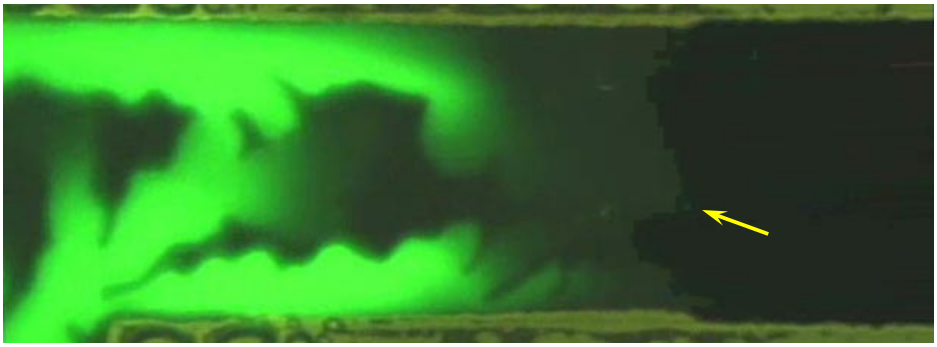

A: front conformation when it stops moving

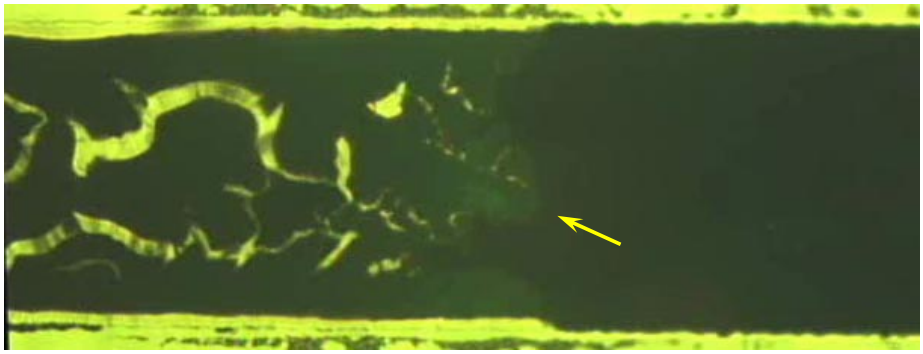

B: open fractures after solution dries up

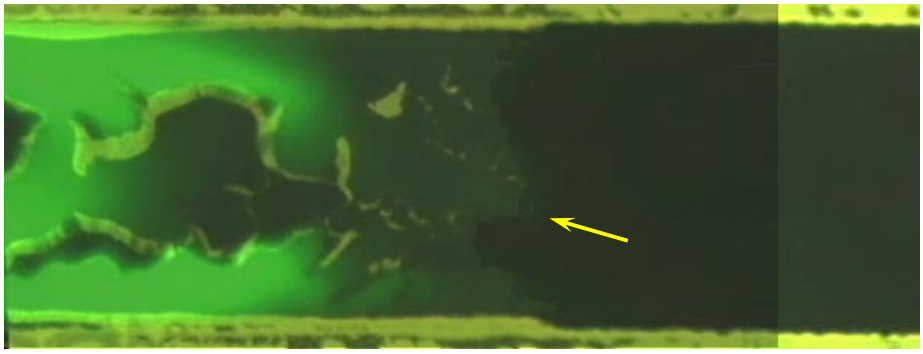

C: superposition of A and B

Figure 5.5 Action of surface tension on a fractal front

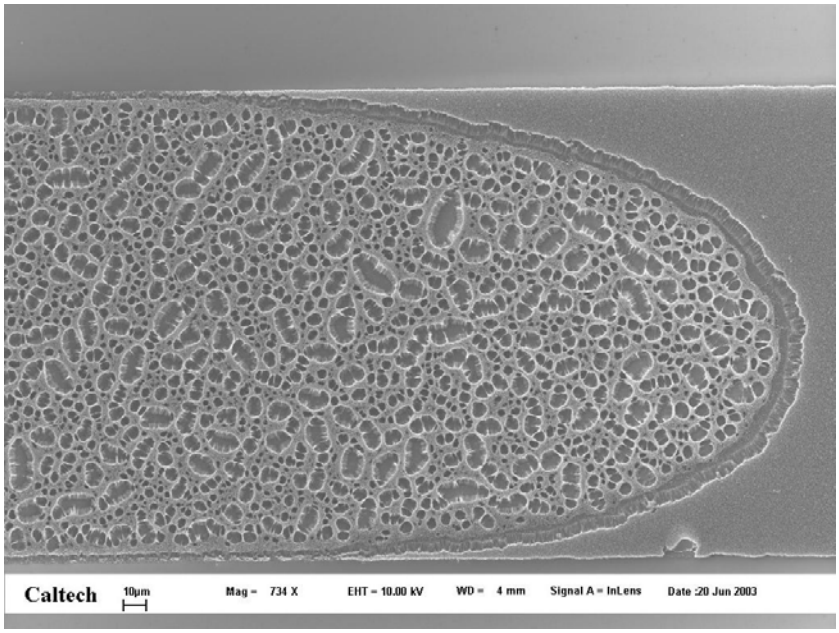

A: 200µm wide nanowick with 0.2%Trition solution

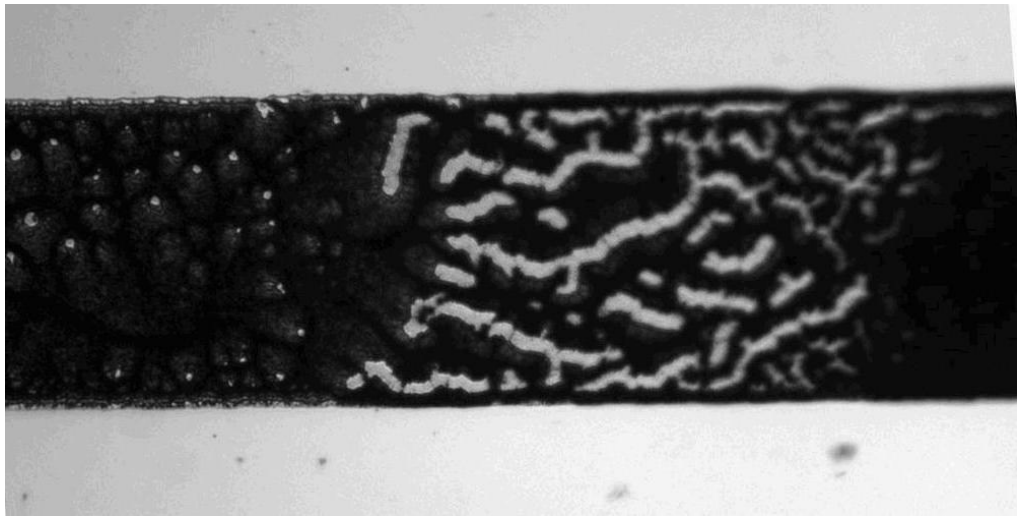

B: 100µm wide nanowick with 0.01% Triton solution

Figure 5.6 Liquid front imprints on 3µm high nanowicks

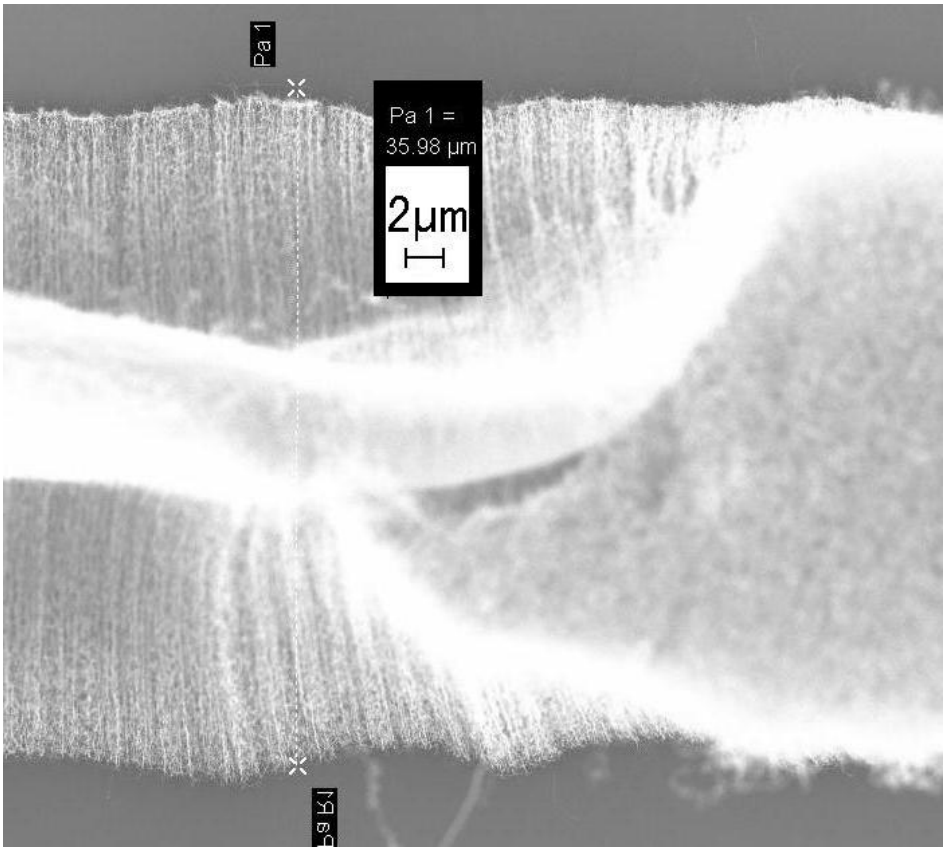

A: 35µm wide nanowick with 0.1% Triton solution

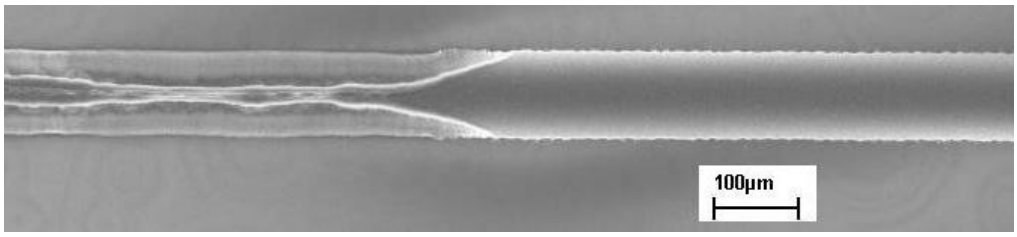

B: 100µm wide nanowick with 0.1% Triton solution

Figure 5.7 Liquid front imprints on 60µm high narrow nanowicks

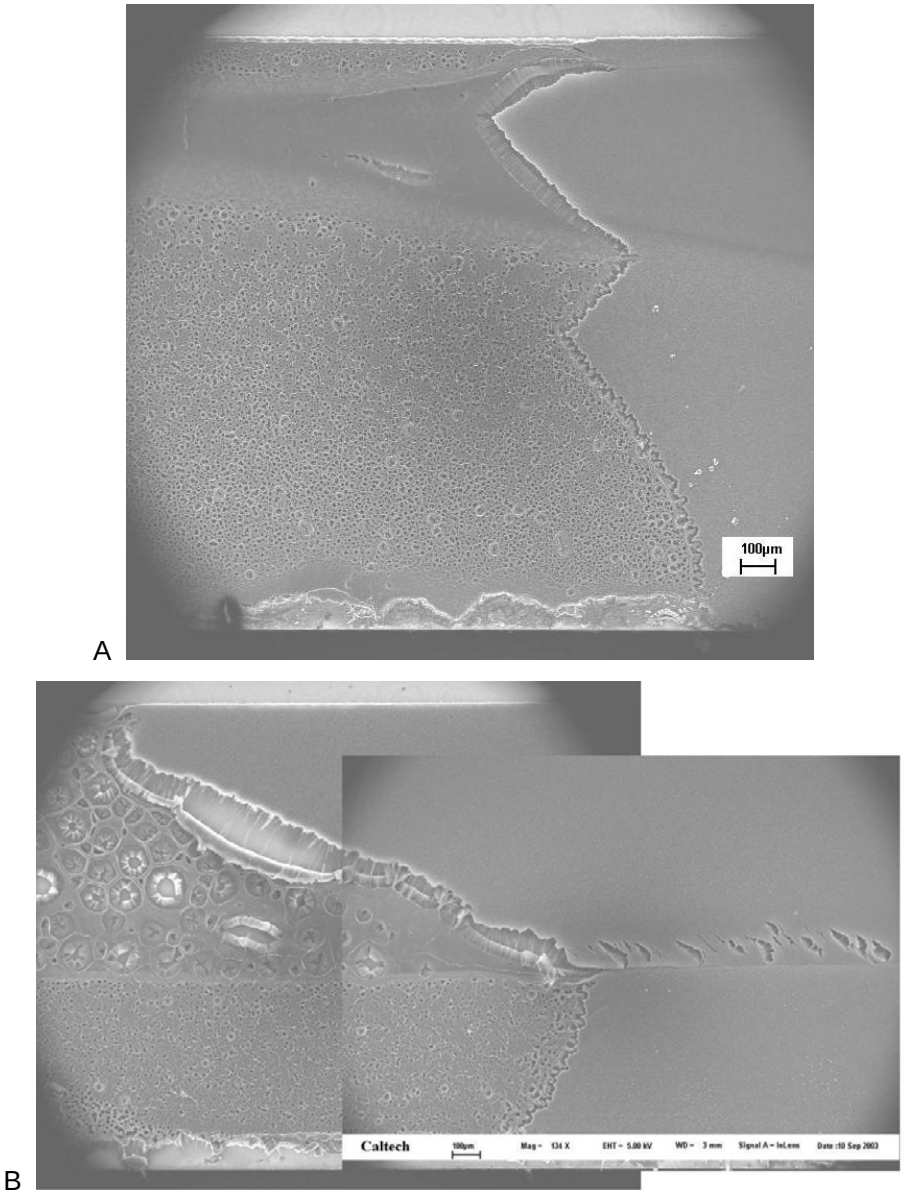

Figure 5.8 Flow response to conformation changes in nanotube arrays on 60µm-high 1.5mm-wide nanowicks with 0.1% Triton solution

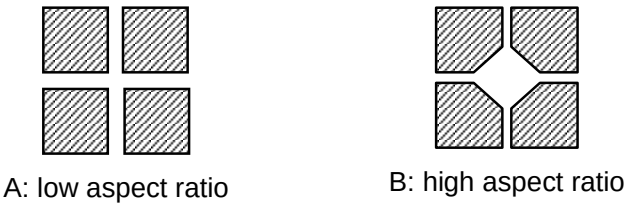

Figure 5.9 <pore body>-to-<pore throat> aspect ratio

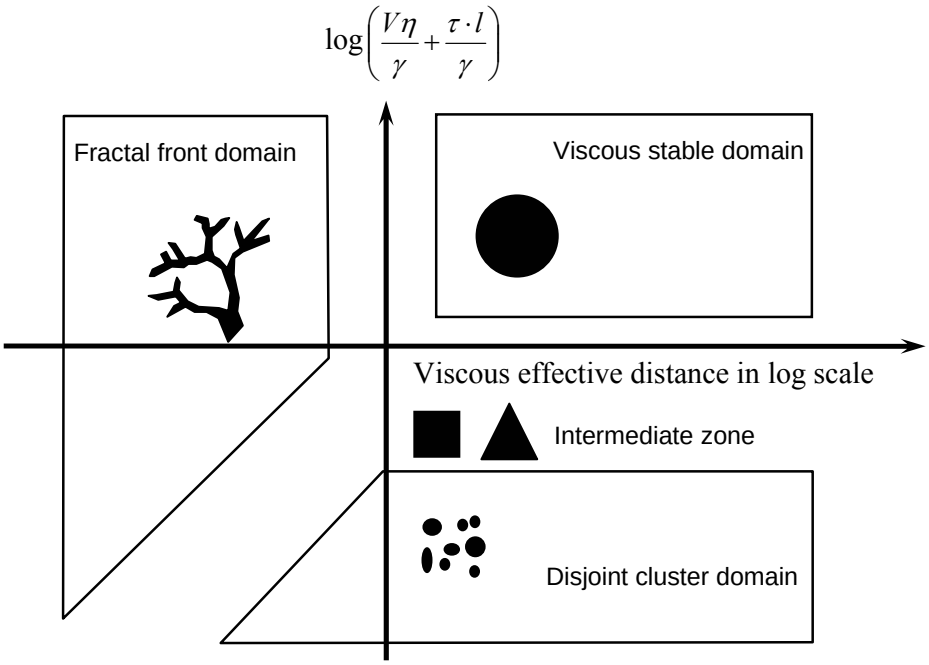

Figure 5.10 Distribution of qualitative competitive domains for viscous, surface tension and wetting effects

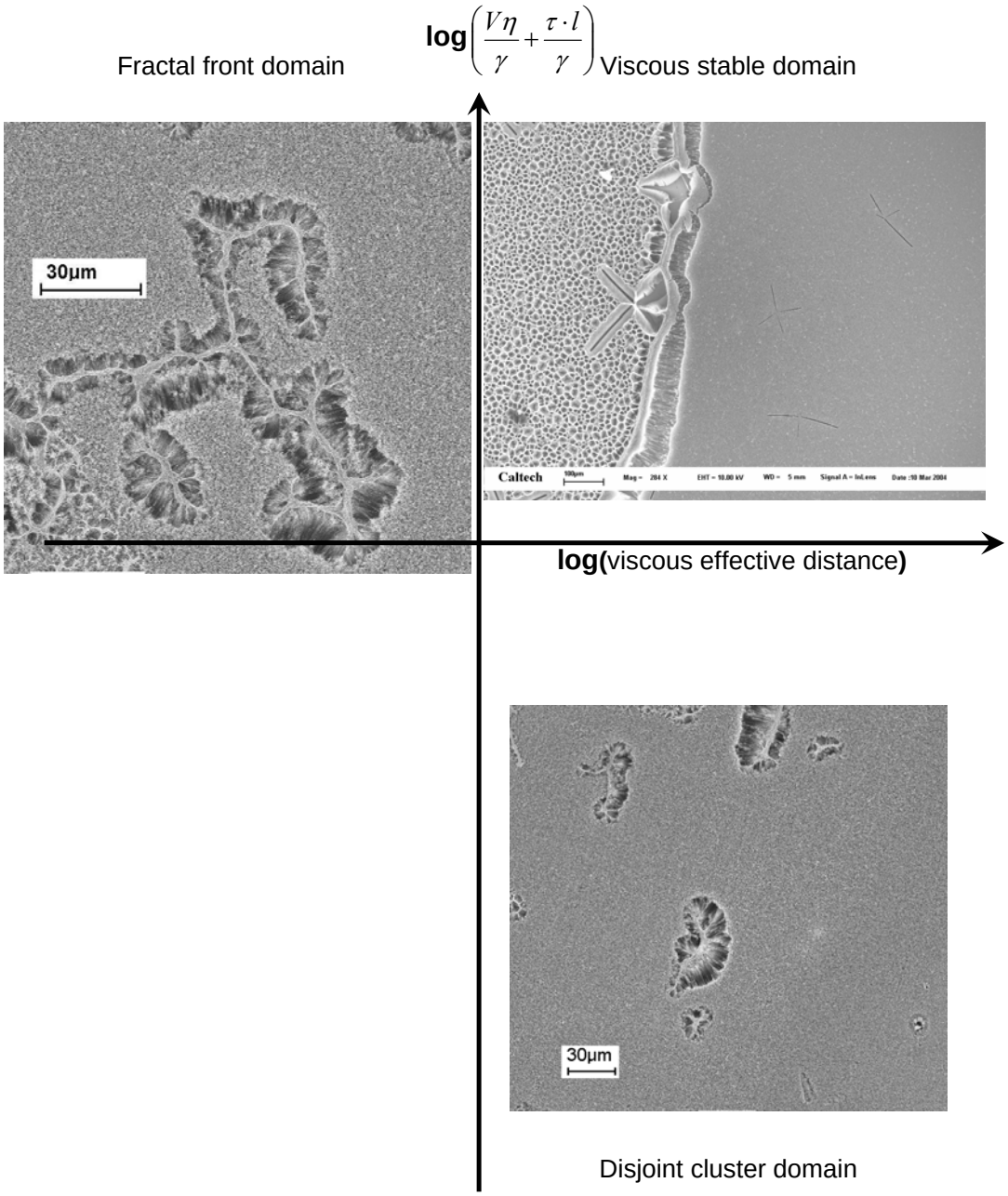

Figure 5.11 Front imprint representation of some domains